MODELING AND SIMULATION OF AN ACTIVE ROBOTIC DEVICE FOR FLEXIBLE NEEDLE INSERTION

Nader Hamzavi Zarghani

NATIONAL UNIVERSITY OF SINGAPORE

2009

MODELING AND SIMULATION OF AN ACTIVE ROBOTIC DEVICE FOR FLEXIBLE NEEDLE INSERTION

Nader Hamzavi Zarghani

A THESIS SUBMITTED

FOR THE DEGREE OF MASTER OF ENGINEERING

MECHANICAL ENGINEERING DEPARTMENT

NATIONAL UNIVERSITY OF SINGAPORE

2009

This thesis is dedicated to

my parents

Acknowledgments

I wish to thank a number of people who advocate and help me with supportive suggestions and encouraging assertions throughout my Master's program. My foremost thank goes to my supervisor Dr. Chui Chee-Kong. I thank him for his complete understanding and support that carried me through all the difficult times in my research period, and for his suggestions which helped me to shape my independent research. I should also express my thanks to Dr. Chui Chee-Cheon with his valuable opinions and suggestions in clarifying difficulties in this research.

I am honored to say my special thanks to all the students and staff in Mechatronics & Control Lab, particularly Dr.Chui's students whose presence and fun-loving spirit made the otherwise grueling experience tolerable.

Last but not least, I would like to thank my parents, my brothers, Navid and Nima, for always being with me when I needed them, and for supporting me through all these years, and my wonderful girlfriend, Ladan, for tolerating my difficult times and soothing me by her uncountable valuable supports.

Contents

Summary

Minimally Invasive Surgery (MIS) is more efficient than open surgery because the recovery and hospitalization time of MIS is considerably less than conventional surgical techniques. An active robotic needle is proposed for flexible needle insertion in MIS. The active needle is designed to improve flexibility and reachability of needle insertion.

With the active needle, we hope to achieve the flexibility to reach otherwise inaccessible clinical targets. We have investigated the kinematics and dynamics of the active needle. Based on a flexible swim-wave travelling path, we developed a new path planning algorithm for the active needle. The needle insertion path could be modified in accordance with the needle-tissue interaction force. We determine the optimal needle insertion path using energy minimization method. This is based on the hypothesis that an optimal path will transfer the minimum energy to the surrounding tissue and hence, cause less tissue injury.

Simulation based design methodology is used in this study. A computer aided design model of the active needle is developed using Solidworks. The sophistical active needle model is then exported to SimMechanics and Matlab for computer simulation of its interaction with the biological tissue during needle insertion. The simulation result agrees with the proposed needle insertion path derived from the path planning algorithm.

The active needle prototype has been fabricated for experimental investigation. The feasibility of the active needle prototype is demonstrated. The active needle is motorized with two actuators for forward and swim-wave motions. The active needle comprises the main body and the closed-loop mechanism. The closed-loop mechanism is a driving system which produces swim-wave motion of the active needle. This mechanism enables the active needle to be sufficiently small for MIS. We have found that the active needle can be steered towards the predefined targets accurately.

Although we have demonstrated theoretically and experimentally the feasibility of the active needle for flexible needle insertion, further study will be required to determine the clinical viability of the proposed active needle device.

List of Figures

List of Tables

List of symbols

M	Bending moment
c_1, c_2	Constant coefficients
C	Coriolis and centrifugal forces
C, S	Cos, sin
V	Cutting force of needle tip
γ	Euler angle about x-axis
β	Euler angle about y-axis
α	Euler angle about z-axis
G	Gravity forces
D	Inertia matrix
J	Jacobian
q	Joint variables
k	Kinetic energy
L	Length of active needle link
E	Modulus of elasticity
I	Moment of inertia
ω	Motion frequency
b_n, b_p	Negative and positive damping coefficients
C_n, C_p	Negative and positive value of dynamic friction
D_n, D_p	Negative and positive value of static friction
u	Potential energy

M	Resolution of motion
$\theta_2, \theta_3, \theta_4$	Rotational displacement of joints
E_1, E_2	Stiffness of tissue
F_a	Sum of nonfrictional forces applied to the system
tp	Time of puncture
$\Delta\frac{v}{2}$	Threshold velocity
${}^0_iT$	Transformation matrix
λ	Wave length
k	Wave number

Chapter 1

Introduction

1.1 Motivation and Background

The application of engineering in medicine is promising and demanding. Although surgery has advanced significantly, surgical outcome is still very much dependent on the skill of the surgeon. Engineers can develop new devices that could assist physicians to perform surgeries accurately and less invasively. Medical robotics is an engineering solution that has improved the capabilities of physicians in healthcare delivery. Robotics in surgery has been expanding over the past decade despite concerns of their effectiveness, safety and high cost. [1].

A medical robot can perform a surgical operation continuously, precisely, and tirelessly for long period with programming. It can place cutting tool at a predefined clinical target precisely. The precision can be improved further when the medical robot is used with surgical navigation system. A robot can also be programmed to restrict the motion of the surgeon in order to perform operation with high level of safety [2]. The effectiveness of a surgery is measured by its safety, invasiveness, accuracy, duration and cost. Engineering in medicine, and specifically robotics in surgery could help the goal of achieving effective surgery.

Robotics in surgery includes the usage of robotic and vision systems to interactively assist a medical team both in planning and executing a surgery [3]. These new techniques can minimize the side effects of surgery by providing smaller incisions, shorter operation time, higher precision, and lower costs than that of conventional methods. Surgical robots are being utilized in remote surgery, minimally invasive surgery and unmanned surgery. The focus of our research is on minimally invasive surgery. Less pain and faster recovery can be achieved by minimally invasive surgery. Unlike a minor surgery, minimally invasive surgery requires general anesthesia before operation.

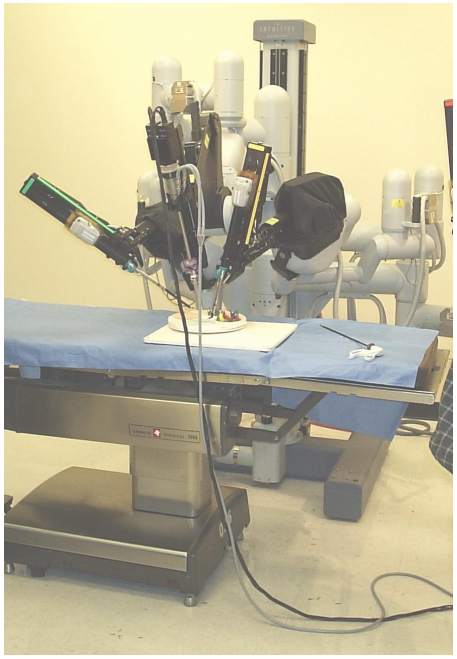

Figure 1.1: Da Vinci Surgical System
[3]

Well known example of a commercially successful surgical robot is da Vinci surgical system. Ninety five percent of patients, underwent prostate operations with this device, came back home after hospitalizing for only one day [4]. In addition to the da Vinci system, there are other robotic systems developed commercially and academically for specialized medical procedures from biopsy to retinal surgery. Early usage of industrial robots was to hold heavy devices at rest during surgical

operations. At that time, robots cannot be used for surgery due to safety reasons. Robodoc is the first robotic system that performed an operation on human to remove the tissue from the patient in late 1991. After that, a robotic system was designed in Imperial Collage of London [5], which enhances precision of surgical operations. In this system, heavy basement with a large workspace is designed to be situated at rest and a smaller device is connected to the heavy base for the minimal operation.

Surgical robots can be dichotomized as either passive or active [2]. The passive type has been used to hold fixtures at an appropriate situation while the active robot can produce more flexible movements when interacting with the patient. Active robots are specifically designed for the task. In our research, a novel type of active robot is introduced for minimally invasive surgery, using active robotic elements.

Our research concerns modeling needle insertion into a soft tissue and simulating path planning. Three major challenges in needle insertion are deformations, uncertainty and optimality [6].

Deformation: When the needle is inserted into a soft tissue, soft tissue will deform due to its interaction with the needle. Therefore, in order to precisely and successfully steer the needle into the target, soft tissue deformation should be considered for percutaneous insertion surgery.

Uncertainty: The needle might not perform action commands accurately with complete certainty in a clinical operation. Clinicians have to make provision for available uncertainties, such as the flexure of the needle due to its interaction with the tissue, to insert the needle into the target with highest possible accuracy.

Optimality: There could be more than one possible path for the needle to reach the clinical target. Among these possible paths, the optimal path should be selected in accordance with an optimization criteria. Energy optimization is the optimization criterion used in our research.

Our research addresses new flexible robotic system which can follow complex paths. The reachability of the robotic system is improved with the mechanical structure of the flexible needle. A closed-loop mechanism is designed to transfer motion from the base joint to revolute joints. This mechanism is small in size since the actuating system of the mechanism is set on the first link of the needle. However, kinematic analysis of the system becomes complex. This research also investigates path planning and simulation of needle-tissue interaction in order to find an optimal path for needle insertion. Experiment of the active needle prototype investigates the accuracy of needle insertion towards predefined targets.

1.2 Objectives and Scopes

A new surgical robotic needle known as the active needle, is proposed to improve the accuracy of needle insertion during surgery. This study focuses on the modeling and simulation of the active needle. By modeling the needle using fish-like robotic elements, path planning algorithm for the active needle is derived and validated with simulation result of needle-tissue interaction. Experiment is conducted to investigate the feasibility of developing an active needle prototype.

The scope of this research covers the following issues:

- Kinematic and dynamic analysis of the active needle,
- Needle insertion; path planning and dynamics,

- Optimization of required energy for needle steering,
- Simulation of active needle,
- Experiment of active needle prototype.

1.3 Thesis Organization

This thesis describes kinematic analysis, dynamic analysis, path planning, simulation, implementation and experiment of the active needle model. A complete research review on the needle insertion is presented in Chapter 2. Chapter 3 presents kinematic, dynamic analysis and implementation of the active needle. In Chapter 4, path planning, identification of path parameters and optimization of the bending energy are investigated. Chapter 5 covers simulation analysis of the active needle's trajectory with SimMechanics. In Chapter 6, accuracy of needle insertion is investigated by conducting experiment with the active needle prototype. Finally, discussion on results and future works for this research are summarized in Chapter 7.

Chapter 2

Literature Review

Many surgical robots have been used to perform or assist needle insertion during surgery. Problems of needle insertion including reachability due to uncertainty of needle steering have been extensively investigated [7–11]. However, an engineering solution that can effectively address the complex problems of needle insertion during surgery has yet to be found. We have proposed to overcome these problems using computer modeling and simulation after an extensive review of the existing literature.

2.1 Robotics in Surgery and Computer Aided Surgery

Computer Aided Surgery(CAS) is defined as a set of methods for preplanning, performing surgical intervention and post-operative procedures [12]. Extracting 3D model from medical images in late 1980s is the early application of CAS for surgical simulation [13]. CAS has three different phases for planning and operation.

These three phases are: pre-operative planning, intra-operative intervention, post-operative assessment. Robotics in surgery can be integrated with these phases of CAS.

In computer assisted robotic surgery, computer technology is utilized for planning, executing and following up of surgical procedures. In this study, surgical robots are not considered to replace the surgeon, but to provide the surgeon with a new set of versatile tools that can extend his or her ability to treat patients. In our terminology, medical robotic systems serve as surgical assistants that work cooperatively with surgeons. Computer integrated robot assisted surgery includes the concept that the robot itself is just one element of CAS, which is designed to assist a surgeon in carrying out a surgical procedure [14].

The robot is used directly in the intervention aspects of the intraoperative phase. However, when a robot is to be used, the planning aspect can also include a computer simulation sequence of robot motions. When the surgeon is satisfied that the sequence is correct and the robot will not impinge on the patient or adjacent equipment, then the motion sequence can be downloaded directly to the robot controller.

In the intraoperative phase, it is necessary to fix the robot with reference to the patient and then register the robot to specific markers or fiducials on the patient, usually by touching the robot tip to the markers [2]. These same fiducials will have been observable in the pre-operative imaging and three-dimensional models, and so this process can register the current patient fiducial location to that on the pre-operative images and models, as well as to the intraoperative robot location. The fiducials are usually small screws inserted into the bone in the orthopaedic surgery or are small discs stuck to the skin, e.g. over boney prominences in neurosurgery.

To ensure that the robot is being correctly employed, an intraoperative display of robot motions is required to guide the surgeon. The robotic display provides

a three-dimensional schematic of the correct position of the tool superimposed over simplified views of the tissue. These simplified schematic views are necessary for real-time viewing of often complex motions. Simple schematic are required for robotic display with only basic robot parameters on the screen, because the surgeon can perform properly in an emergency [15]. In an emergency, it may be necessary to abort the robotic procedure and it must be ensured that at all times it is possible to finish the surgery using a safe manual procedure. However, full diagnostics should be available on the screen when the full status of procedure is required to judge for next motion of robotic device.

An immediate assessment phase is usually required post-operatively. This requires that the robot can be readily removed and the patient unclamped so that the patient can be moved around. Rapid robot removal is also essential for safety reasons, so that if the robot malfunctions, it can be quickly removed and the procedure completed manually. In order to perform further action based on the assessment, it will be necessary to re-clamp the patient and reposition and re-register the robot.

Clinicians have been referring to CAS as medical robotics [16]. Medical robotics have vision from medical imaging as well as intelligence through computing. The market of medical robotics is expanding worldwide and is employing different technologies including surgical robots, control, imaging, surgical simulators, safety devices for computer-assisted surgery. CAS is using novel technologies to improve accuracy and precision and also to reduce invasiveness and cost of surgery [17].

2.1.1 Classification of Medical Robots

Surgical robots can be classified with respect to their technology basis [2]. The powered robot can be used in either passive mode or active mode to perform an operation. Using powered robots passively was the earliest applications of surgical

robots as a means of holding fixtures at an appropriate location, so that the surgeon could insert tools into the fixture [18]. These systems have the potential to provide a more stable platform to be more accurate for deep-seated tumors than equivalent camera-based localizers or localizers based on unpowered manipulator arms. A powered robot can be used to interact with the patient actively and create more complex motions potentially than that of a powered robot used passively. Most active robots have been developed specifically for the task and safety level has been set high.

2.1.2 Application of Medical Robots

Probably the largest sales of a commercial system for robotic surgery have been in the area of the manipulation of laparoscopes, mostly for abdominal, minimally invasive surgery [19,20]. There are also many clinical operations which require percutaneous diagnosis and therapies. In these operations, a thin device(needles, catheters, and ablation probes) will be inserted into a non-homogenous tissue. Application for percutaneous insertion are blood sampling [21], biopsy [22], brachytherapy [23] and neurosurgery [24].

The accuracy of an operation may vary for different applications. In eye, brain and ear procedures micro-millimeter is the required accuracy while placement accuracy for biopsy, brachytherapy and anesthetic in millimeter scale is satisfactory. It has been revealed that imaging misalignments, imaging deficiency, target displacement due to tissue deformation, needle deflection and target uncertainty are the main reasons for missing the target [25–30].

2.2 Percutaneous Insertion Therapy Constraints

Computer integrated surgery with medical robotics can provide solutions for existing constraints in percutaneous therapy. The major constraints are target visibility, target access and maneuverability of tool. Surgeons perform operations conventionally with their mental 3D visualization feedback from the tool [7].

In order to improve target visibility, visualization techniques have been evolved with real-time imaging. Although real-time imaging can improve the surgeon's vision for surgical operations, human error, image limitations, tissue deformation, needle deflection, and target uncertainty are still reducing accuracy. Moreover, there is difficulty in determining the position of the target due to the patient's movement, geometry or physiological changes of tissue [26]. Other sources of defects should also be considered; for instance, the robot which is performing around MRI device should be made of special material with nonmagnetic actuators due to the presence of the strong magnetic field around MRI device [31].

The target can be missed by the surgeon, if the needle excessively deflects. Needle deflection is a serious problem in dental anesthesia [32]. Kataoka et al. [33] have investigated the relationship between diameter of the needle, the needle tip shape and needle deflection by introducing a force-deflection model. Their model can successfully predict the deflection of the needle. However, only transverse loading is assumed in their experiment; this transverse loading is applying on the needle as a constant force per length.

Altrovitz et al. [34] have computed tissue deformation due to the needle tip's shape and frictional forces which are exerted on the needle. Their objective was to steer the needle and to avoid obstacles with minimum insertion depth. Minimizing the transferred energy to the tissue in every insertion depth is suggested in our study which seems more accurate and more effective. Bevel tip and needle diame-

ter are major causes of needle deflection. Moreover, the needle can deflect due to tissue deformation. Thus, the needle tip's contact force, properties of viscoelastic material and frictional force have influences on tissue deformation which leads to needle deflection [29]. In addition, Abolhassani et al. [8] have addressed physiological changes which may cause inaccuracy for percutaneous therapies. Prediction of needle deflection may require intensive computation using finite element (FE) methods.

2.3 Modeling of Needle Deflection

Needles have variable shapes and diameters with different flexibility and maneuverability. Needles can be categorized into two groups: rigid and flexible needles. Needle is rigid when remains stiff after insertion, or flexible when deflects with small transverse forces.

2.3.1 Rigid Needle

The stiffness of the rigid needle is high enough to maintain its straight posture after applying transverse loading on the needle. Needle deflection is negligible for the rigid needle insertion. The needle can be model as a rigid needle whether applied forces are not immense in magnitude or the needle is made up of inflexible material.

Many researchers have studied modeling and simulation of rigid needle insertion. Altrovitz et al. [9] have simulated effects of the needle tip and frictional forces with 2D dynamic FE model. They implemented a seed at the location of the needle tip. The output of simulation is compared to ultrasound video taken from a real medical procedure on a patient going under brachytherapy treatment for prostate cancer with a rigid needle.

DiMaio and Salcudean [7] have investigated needle forces during soft tissue penetration. Deflection of the tissue is measured by a 2D elastic model and the needle is modeled as a rigid needle due to its minimal bending. Dehghan and Salcudean [35] proposed a new method of path planning for rigid needle insertion into soft tissue. In their approach, needle insertion point, heading, and depth of needle insertion were optimized. They used a robotic system with 5 degrees of freedom to place the needle in proper orientation and one degree-of-freedom to move the needle forward.

2.3.2 Flexible Needle

Executing surgery with the flexible needle is one of the least invasive mechanisms. Three initial application areas of needle steering include the prostate, liver, and brain; these examples illustrate the ways in which needle steering might address difficulties observed by surgeons while using traditional rigid needles, thereby improving targeting, enabling novel treatment methods, or reducing complexity is required.

Needle biopsy for diagnosis of the prostate cancer is performed on about 1.5 million men per year and one in six men in the United States will be diagnosed with this condition [36]. A common treatment option is trans-perineal brachytherapy [37], involving implantation of thin needles to deposit radioactive seeds. In these procedures, it is challenging to achieve precise targeting in the event of organ dislocation and deformation. Significant seed-placement error can occur if the needle is tangential to the prostate capsule wall upon penetration. Hence, the ability to steer the needle and bevel to an optimal capsular penetration angle is of particular importance. After penetration, steering within the prostate may be useful for correcting the combined effects of deflection, dislocation, and deformation of the organ observed in contemporary practice.

The liver cancer is one of the most common cancers in the world, and also one of the deadliest. Without treatment, the five-year survival rate is less than 5 percent. The liver is also the most frequent location of secondary tumors metastasized from colorectal cancer, with about 130,000 new cases and 60,000 deaths annually in the United States alone [38]. Liver tumors smaller than 5cm in diameter are often treated with thermal ablation administered at the needle tip which is inserted into the skin and visualized with ultrasound imaging techniques.

Since liver tumors often have very different mechanical properties than the surrounding tissue, they can behave as if encapsulated with respect to needle penetration, presenting challenges similar to those of the prostate. Also, all but the smallest liver tumors [39] are large enough to require multiple overlapping thermal treatments for full coverage. Currently each treatment requires removing and reinserting the needle. If it were possible to partially retract, steer, and redeploy the needle into an adjacent treatment zone, some targeting uncertainty and additional puncture wounds might be avoided.

In the brain tissue, steerable needles might be used to stop the flow of blood from an intracranial hemorrhage (ICH), and remove resulting clots via targeted drug injection. The incidence of ICH ranges from 10 to 20 persons per 100,000, and untreated clot resolution takes two to three weeks, with an exceedingly high mortality rate of 50 to 75 percent. It is suggested that ultra-early intervention, given within three to four hours of onset, may arrest ongoing bleeding and minimize swelling of the brain after ICH [40].

Precisely steered delivery vehicles have the potential to increase drug-target interactions and may enable very rapid removal of clots. In a typical emergency setting, a burr hole to introduce a device for injecting such drugs, is drilled freehand and is seldom aligned with the optimal path to the target.

The location and orientation of the burr hole is fully dependent on the surgeons

hand-eye coordination, and the trajectory may be off-angle by as much 20-25 degrees. The burr hole is usually made significantly larger than the diameter of the interventional tool, and this can lead to subsequent technical and clinical complications. Steerable devices may allow this hole to be much smaller, since steering can compensate for initial alignment error.

Flexible needles can be divided into two subgroups: highly flexible needle and moderately flexible needle. Highly flexible needle has extreme flexibility and bends with inconsiderable amount of the lateral force. This type of needles is following the direction of bevel tip needle with a constant curvature. To steer a highly flexible needle towards 3D specified target through soft tissue, Webster et al. [10] have used nonholonomic bicycle and unicycle modeling. Nonholonomic kinematics, control, and path planning were used for a bevel tip needle to enhance potential for precise targeting and a robotic system was built to validate their theoretical model.

Altrovitz et al. [41] have steered a flexible needle with a new motion planning algorithm. The parameters for this algorithm can be extracted from images to calculate optimal needle entry point and next movement. They have considered uncertainty in motion and introduced a probability method to maximize success of reaching target. The needle which can follow their suggested path should be highly flexible. Therefore, a thin bevel needle tip is used for path planning. This new class of medical needles can reach targets which are inaccessible for rigid needle [42]. Park et al. [43] have also addressed the problem of steering a highly flexible needle through a firm tissue. They proposed a nonholonomic kinematic model with proven reachability and different possibilities for positioning the needle tip.

There is another type of needles in brachytherapy, neither rigid nor highly flexible. They are not rigid because the needle will deflect under external lateral forces. They are not also highly flexible since it is necessary that a considerable force is required to bend them. This type of needles is known as moderate flexible needle.

Many researchers have studied FE methods to model this type of needles. DiMaio and Salcudean simulated the needle as an elastic material using FE methods with geometric nonlinearity and 3-node triangular elements and validated this method in phantom studies [44]. Their method was evolved to 3D by using 4-node tetrahedral elements by Goskel et al. [11] using FE methods with geometric nonlinearity.

Linear beam theory is another approach adapted by many researchers. Glozman and Shoham [45], considered tissue forces as linear lateral force applied by virtual springs. They modeled the needle with 2D linear beam. They have noticed that the needle cannot be controlled in large depth of insertion and other techniques should be suggested. Yan et al. [46] developed needle steering model by using linear beam elements.

Kataoka et al. [33] represented force-deflection model for a linear beam element needle and validated the model with experimentally acquiring data from force sensors. They calculated deflection of the needle during insertion by measuring a physical quantity called infinitesimal force per unit length. Goskel et al. [11] explored modeling and simulation of moderate flexible needle and used three different models to simulate needle bending. They selected two FE methods: first with tetrahedral elements and second with nonlinear beam elements, as well as angular spring model. The forces cannot be determined before experiment or simulation of needle insertion. In this study, they predicted needle deflection for a wide range of load with single fixed parameter for each model. They have concluded that beam element is more efficient computationally, in comparison with tetrahedral or triangular element model.

2.4 Tissue Deformation Modeling

Soft tissue has visco-elastic behavior with anisotropic, nonlinear, and inhomogeneous characteristics. Therefore, tissue modeling and tissue deformation are very complicated problems which require accurate and fast calculations. Planning, simulation, and accurate calculation of complex behaviors of tissue in real-time can improve computer integrated assisted robotic surgery. There are a number of mathematical and experimental models for modeling soft tissue. Biomechanical properties of soft tissue can be determined with special measurements (*invitro* and *invivo*) and using constitutive laws. Real-time simulation of the tissue is modeled by spring-mass-damper or finite element (FE) models.

2.4.1 Soft Tissue Biomechanical Properties

Although mechanical properties of soft tissue and *in vitro* measurements have been focused in some studies [47, 48], quantitative modeling of *in vivo* soft tissue has recently been studied in depth to improve soft tissue modeling. Nightingale et al. [49] measured tissue stiffness with acoustic remote palpation (physical examination in which an object is felt to determine its size, shape, firmness, or location) imaging. Trahey et al. [50] have also measured arterial stiffness by means of force impulse imaging with developed acoustic radiation system. Han et al. [48] have evaluated assorted methods for measuring biomechanical properties of soft tissue with a novel ultrasound indentation system. Menciassi et al. [51] have quantified *in vivo* tissue properties using a microrobotic instrument. This instrument is able to sense vessels in scale of micro to qualitatively and quantitatively measure tissue properties. *In vivo, in vitro* excised lobe case, and *ex vivo* whole organ with/without perfusion are various biomechanical characteristics which are investigated and categorized [52].

Measurement devices should be small and accurate for collecting *in vivo* tissue

properties data. A device named TeMPeST (tissue measurement property sampling tools) is used for measuring the compliance of solid organ tissues *in vivo* by performing small-indentation test on suitable structures (such as the liver or the kidney) [53]. This device can vibrate the organ or the tissue with a punch to register relative displacement versus applied force at a moderately fast frequency. Thus, it can measure strain frequency response of the system with 1mm as motion range and 300 mN as maximum exerted force.

Ottensmeyer et al. [52] also conducted similar experiment with visco-elastic soft tissue property indentation instrument. This instrument has a flat punch that lays on the tissue surface and then, weights will be released on it to cause a large strain in order to measure normal tissue strain. Another apparatus is designed to maintain cellular integrity while performing *ex vivo* experiments. They have found similar results for large deformation time responses in the experiment with those of the perfusion apparatus of tissues tested *in vivo*. They also suggested testing whole organ rather than a cut of specimen for a more accurate reference.

The perfusion system has some advantages over *in vivo* experiments regarding the cost of testing, ethical and administrative issues. However, this system is analyzing the organ individually without considering neighboring tissues. Thus, other surrounding tissues are not enforcing boundary constraints.

In order to measure interaction forces between tissue and instrument, tissue strain, and tissue indentation, some devices have been developed. Brouwer et al. [54] used exponential equations to fit on data which is acquired from *ex vivo* and *in vivo* experiments performed on abdominal porcine tissue. In this case, boundary condition of surrounding tissue is not considered because the tissue was cut off from surrounding anatomical structure. Brown et al. [55] developed an endoscopic grasper to automatically perform experiments (*in vivo* and *in situ*) on abdominal porcine tissue. Compressive loading is applied cyclically and also statically with no

preconditioning tissue. Their observation revealed that exponential equation can express the relation between stress and strain for the collected data. Chui et al. [56] reported that a combined logarithmic and polynomial equation well represents the nonlinear stress-strain data of biological soft tissue.

Although a nonlinear model can represent relaxation behavior after the first squeeze, a linear model might express relaxation behavior for subsequent squeezes. In addition, the relaxation behavior was shown to be different from *in vivo* and *in situ* experiments. They have added value to their work by performing the experiment on the organ of the same pig for both *in vivo* and *in situ* experiment.

In order to standardized measurement of soft tissue, Kerdok et al. [57] introduced a reference cube as the truth cube made of soft polymer to investigate the deformation of soft tissue. Beads are placed in a grid pattern throughout the volume of the cube to measure tissue deformation. When the cube is under pressure, they can record displacement of the beads with CT-scan images. Deformation of the truth cube is compared to real-time tissue deformation modeling FE methods considering bead displacement, boundary conditions, and material properties.

Kerdok et al. [57] preferred the truth cube to FE methods because of difficulty and uncertainty accuracy in FE modeling techniques. The material of the truth cube has been evolved through different experiments; silicon rubber was a preliminary model. This model cannot represent the behavior of real soft tissue, because it has a simple configuration which is different from geometry of a real organ. Therefore, Kerdok et al. [57] and Howe [58] replaced the truth cube by a whole real organ which was the bovine liver. In order to provide a realistic condition, the liver organ was perfused with physiological solutions at pressure and temperature of real condition. To enhance the accuracy of FE calculations, creep modulus and the relaxation modulus were measured, as well as constitutive law parameters. Similar results were reported between the experiment setup and the

in vivo mechanical responses of the liver.

2.4.2 Tissue Modeling

Tissue modeling can be developed with soft tissue fundamental laws. The modeling is based on nonlinear stress-strain relationships, large deformations, visco-elasticity, nonhomogeneity, and anisotropy [59]. Due to the nonlinearity of stress-strain curve, the relationship between force and displacement will be nonlinear. Large deformation is a probable reason for nonlinearities.

Mass-spring models are useful for real-time simulation [46], although these models have limited accuracy [58]. In order to address the visco-elastic behavior of a soft tissue, *ex vivo* and *in vivo* experiment are widely studied [56, 60–62]. Soft tissue strain rate is related to the stress τ on a liver tissue sample and hence, liver could be considered as viscous. The viscous material deforms under instantaneous forces as well as applied forces. Linearity elasticity is introduced by two terms: geometrical and physical linearity. In geometrical linearity, higher terms are eliminated assuming small deformations, and in physical linearity, relationship between stress-strain tensor is assumed linear [63]. Tensor-mass model can represent viscoelasticity in case of viscous modeling with simple linear relations. The Maxwell, Voigt and Kelvin models are three most widely implemented mechanical models in modeling soft tissue [47], [63], [64]. Schematic diagrams are shown in Fig. 2.1.

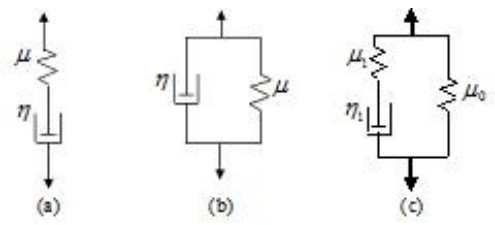

Figure 2.1: Mechanical model of viscoelastic material

In our study, Kelvin model also known as the standard linear model is used for tissue modeling. The tissue is assumed as a linear viscoelastic material. Therefore, Kelvin model can well approximate the mechanical behavior of the tissue. In linear viscoelastic model, linear elasticity is related to constant viscosity. The displacements are broken down into that of the dashpot and spring, whereas the total force is the sum of the force from the spring and the Maxwell element in the Maxwell model (Fig. 2.1).

Accuracy may be increased with FE methods for modeling small linear elastic deformation. However, FE calculations are computationally intensive and accuracy of calculations is based on number of input nodes [58, 59]. Mass-spring-damper model is also used to model dynamics interaction between lateral steering force acting on the needle and the needle tip lateral movement [46].

Many researchers have focused on FE techniques to model soft tissue properties. DiMaio and Salcudean [7, 44] have conducted comprehensive studies on modeling and simulation of tissue deformation during needle insertion into soft tissue. They used a realtime haptic simulation system which permits the user to execute needle insertion virtually with visual and kinesthetic feedback. They also calculated deflection of the working nodes attached to the needle with force boundary conditions. Displacement boundary conditions were adjusted regarding needle geometry and type. Physical experiment was conducted to set values for displacement boundary conditions of a flexible needle as well as force boundary conditions.

It is necessary to have a uniform mesh for condensation (technique for reducing the complexity of volumetric finite element models), but consequently, it requires a large memory for calculations. Nienhuys and van der Stappen [65] addressed the problem of modeling tissue using FE methods and developed iterative algorithms which require no pre-computed structures. Therefore, they could focus on a region

of interest to reduce the size of computations with an adaptive mesh. They have noticed that 3D simulation of haptic application would be highly computationally intensive.

Alterovitz et al. [9] simulated needle insertion for prostate brachytherapy, with 2D FE modeling. The property of the prostate, membrane and surrounding tissue is considered to be homogenous and linear elastic. Other mechanical properties are extracted from previous experiments (Young modulus and Poisson ratio). Force boundary conditions were employed for the elements to simulate needle insertion. A larger force for puncturing membrane tissue was an assumption of the simulation.

Required nodes were assigned to measure two types of applied forces: frictional force and the needle tip force. Nodes were maintained along the needle shaft and one node was at needle tip. In simulation, a static ultrasound image was deformed using the generated mesh deformations. Seed implantation was investigated in their simulation while considering tissue deformation which causes misplacement of the needle. They have observed changes in some parameters (depth and height of needle insertion, needle friction, needle sharpness and tissue property parameters of the patient) which determine the sensitivity of the seed placement error. In their conclusion, less seed placement error can be achieved with deeper insertion or sharper needle. In addition, seed placement error is minimal with the variances of the biological parameters of global tissue stiffness and compressibility. Increasing needle insertion velocity causes smaller deformation and seed placement error.

Different algorithms were also compared to increase the accuracy of real-time tissue modeling [66]. Heimenz et al. [67] and Holton [68] obtained data from a great number of insertions into different materials relevant to epidural insertion, using a force feedback model. This model was used for training anesthesiology residents, to perform needle insertion simulation with haptic devices [69].

2.5 Modeling Needle Insertion Forces

Accurate needle insertion requires a profound knowledge of interactive forces. Different tissue types can be identified and modeled with this knowledge and then, tissue deformation and needle deflection can be reduced by providing proper feedback to insertion robotic system.

An accurate model is able to differentiate between stiffness, damping and insertion forces. The magnitude of insertion forces can be measured in experiment and compared with suggested model. This model should identify some features such as the force peak and latency in the force changes. The magnitude of latency of the force should be very precise for applications with predictive force control; however, the exact value of these forces is not required in haptic simulation systems and human perception can compensate for the tolerance of the force magnitude.

The tissue is anisotropic and nonhomogeneous due to different tissue layers such as skin, muscle, fatty, and connective tissue. A certain amount of force is required to penetrate into each layer; therefore, the force changes accordingly layer by layer. On the other hand, the required amount of force is variable for the same tissue but for different patients with different ages, genders, body mass, etc. Fig. 2.2 shows the force profile with respect to time during needle insertion and retraction [70].

This data is obtained from *in vivo* insertion into the liver when other anatomical layers have been removed. Simone and Okamura [71], investigated modeling of needle insertion forces for the bovine liver and considered puncture of the capsule as an event which divides the insertion into pre-puncture and post-puncture phases. In pre-puncture, the force increases steadily and suddenly drops which indicates a successful puncture happened. The required force for post-puncture changes due to friction, cutting, and collision with interior structures. The total force acting on

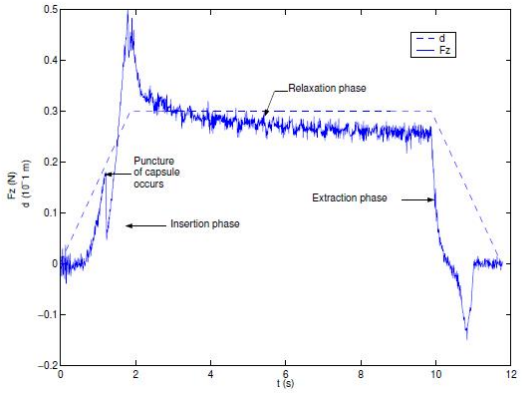

Figure 2.2: Force measurement during needle insertion and retraction for liver tissue
[70]

the needle is:

$$f_{needle}(z) = f_{cutting}(z) + f_{friction}(z) + f_{stiffness}(z) \tag{2.1}$$

where z is the position of the needle tip. In Eq. 2.1, the stiffness force belongs to pre-puncture and frictional and cutting forces belong to post-puncture.

Pre-puncture and post-puncture phases are shown in Fig. 2.3. The elastic properties of the organ and its capsule are causes of the stiffness force. Simone and Okamura [71], developed a nonlinear spring model for the stiffness force:

$$f_{stifness} = \begin{cases} 0 & z < z_1 \\ a_1 z + a_2 z^2 & z_1 \leq z \leq z_2 \\ 0 & z > z_3 \end{cases}, \tag{2.2}$$

where z is the needle tip's position and z_1, z_2, z_3 are shown in Fig. 2.3. The friction can be modeled by modified Karnopp model [72] (see Fig. 2.4):

$$f_{friction} = \begin{cases} C_n sgn(\dot{z}) + b_n \ddot{z} & \dot{z} \leq -\Delta\frac{v}{2} \\ max(D_n, F_a) & -\Delta v/2 < \dot{z} \leq 0 \\ min(D_p, F_a) & 0 < \ddot{z} < \Delta v/2 \\ C_p sgn(\dot{z}) + b_p \dot{z} & \dot{z} \geq \Delta\frac{v}{2} \end{cases}, \tag{2.3}$$

where C_n and C_p are negative and positive values of dynamic friction, b_n and b_p are negative and positive damping coefficients and D_n and D_p are negative and positive values of static friction, $\dot{z}$ is the relative velocity between the needle and the tissue, $\Delta\frac{v}{2}$ is the value below which the velocity is considered to be zero and F_a is the sum of nonfrictional forces applied to the system.

In Ref. [71], Simone and Okamura performed sinusoidal needle insertions with different frequencies and velocities to obtain force data and to find model parameters. They modeled remaining forces as the cutting forces which are necessary for slicing through the tissue. The cutting forces were modeled as constants for a given tissue:

$$f_{cutting} = \begin{cases} 0 & z_{tip} \leq z_2, t < t_p \\ a & z_{tip} > z_3, t \geq t_p \end{cases}, \tag{2.4}$$

where z, z_2, z_3 are the same as in Eq. 2.4, t is time and t_p is the time of puncture. The cutting force value was calculated by subtracting the estimated frictional force from the total force after puncture. CT fluoro imaging was used to identify different phases and calculate the relative velocities of the tissue and the needle. Model parameters have been determined for the average data obtained during needle insertion into the bovine liver. The model was compared and validated with the actual data.

Okamura et al. [73] investigated the effect of the needle diameter and type of the needle tip on insertion forces. It was noted that type of needle tip type has a

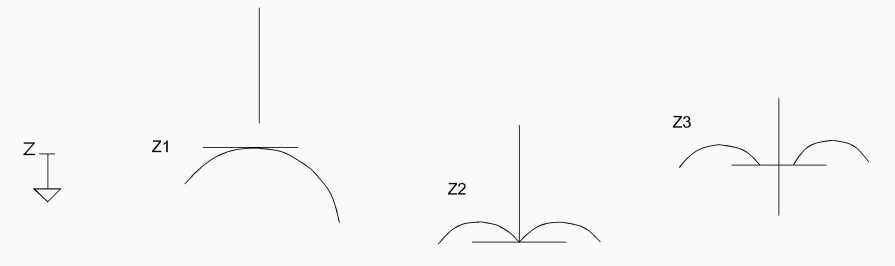

Figure 2.3: Needle insertion direction: before puncture, puncture and post puncture

significant effect on insertion forces. They revealed that for each type of the needle tip, the insertion force increased for needles with larger diameter. The insertion force was also increased as the type of the needle tip changing from triangular to bevel and from bevel to cone but the bevel angle did not affect the axial force significantly.

Maurin et al. [70] performed *in vivo* needle insertions into the liver and the kidney of anesthetized pigs to study insertion forces. They conducted manual and robotic insertions to compare to each other. In manual insertions, the radiologist inserted a needle by manually holding the force device attached to the needle. In the robotic insertions, the needle holder was attached to end-effector of the robot. In the manual insertion, estimation of depth was difficult because no imaging system was used. The needle was inserted for approximately 30 to 50mm. While in robotic insertion, they had a fixed insertion depth of 20 mm. Two methods were used for accessing the organ: "direct access" and "with skin access". All other anatomical layers were removed in "direct access" and different anatomical layers exist in "with skin access".

From their result, it can be seen that multiple layers in the method "with skin access" enhance the amount of forces. Furthermore, they concluded that generally less force is required for robotic insertion than manual insertion in the method "with skin access". However, this conclusion cannot be generalized for their result

of the "direct access" method. Comparison in magnitude of peak force was achieved with a controlled insertion depth of both cases, robotic and manual insertions.

They also used two models for their measurements. The first model was taken from Simone and Okamura [71]. They fitted a second-order polynomial to the data for modeling stiffness force and the Karnopp model for modeling the frictional force. The second model was taken from Maurel [74], based on the work of Fung [47]. They could achieve low errors for both models.

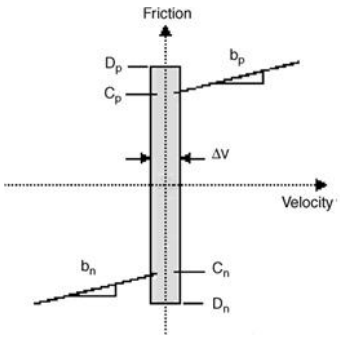

Figure 2.4: The modified Karnopp friction model [72]

Kataoka et al. [33] performed experiments on an exposed prostate of a defrosted beagle cadaver and used a specially designed load cell with seven axes for measuring and separating forces during needle insertion. They used a needle with a triangular pyramid tip and measured applied forces on the needle in three categories: the tip force, the frictional force and the clamping force.

The force acting on the needle tip in the axial direction was assumed to be primarily related to the cutting force. The amount of force was dependant on the shape of the needle tip. It was considered that summation of coulomb and viscous friction is the overall frictional force acting on the sidewall of the needle shaft in the axial direction. When the needle was pushed away from the needle path, a compression force was applied on the sidewall of the needle in the normal direction. This resisting force was called the clamping force. The clamping force increased as

the needle was inserted deeper into the tissue. Its magnitude was affected by the needle gauge and the incision shape.

There was a sudden drop in the amount of the needle tip force after puncture because the inner tissue is softer than prostate capsule. Nevertheless, all tissue types may not behave similarly to have a constant cutting force. The frictional force increased proportionally to the true insertion depth according to the needle diameter. Kataoka et al. [33] calculated the true insertion depth by subtracting the surface motion from the driving distance of the needle. Two main reasons for inaccurate calculation of the insertion depth were tissue deformation and surface deformation due to the compression and sliding back on the needle after puncture. They presented that the total axial force was the summation of the needle tip force and the frictional force. The clamping force affects the value of the frictional force.

Matsumiya et al. [75] presented an experimental study of robotic needle insertion into a formaldehyde-fixed (FAfixed) human vertebra and measured forces and torques during insertion. The needle type was triangular pyramid tip which was inserted by a robotic device. This robot could insert the needle with bidirectional axial rotation and it was specially designed for percutaneous vertebroplasty. Their results presented a strong correlation between the axial force variation during insertion and the distribution of the bone local CT-value along the needle path. CT-value is the value which is acquired from x-ray CT image of the bone.

In the study by Matsumiya et al. [75], the influence of FA-fixation on the axial force was investigated by measuring and comparing the axial force during needle insertion to human femoral heads that had been preserved under freezing or FA-fixation. The axial force for robotic insertion into human femoral head was found to be smaller than that for manual insertion (about 1/3 of the manual insertion). They mentioned two reasons for the smaller axial force in robotic insertion. First, the robot could hold the needle more stably during insertion than a human. This

stability was achieved by a constant insertion speed in their experiments. Second, the speed and the angle of rotation (in case of having axial rotation) can be varied easily in robotic insertion. Their result proved that robotics can provide a safer needle insertion operation in percutaneous vertebroplasty due to reduction in the amount of the axial force. Their conclusion was not analytically proven.

DiMaio and Salcudean [7, 76] developed a planar robot to be navigated in an artificial phantom under a CCD camera supervision to explore the relationship between needle forces and 2D tissue deformation. Fig. 2.5 illustrates the force distribution along the needle shaft for needle insertion into a nonhomogenous phantom [71]. Existence of two forces was indicated: an axial frictional force and a peak force. Frictional force between the needle and the tissue in a uniform form along the shaft produces the axial force, and the cutting force causes a force peak at the needle tip. The cutting force is approximately twice the frictional force [7].

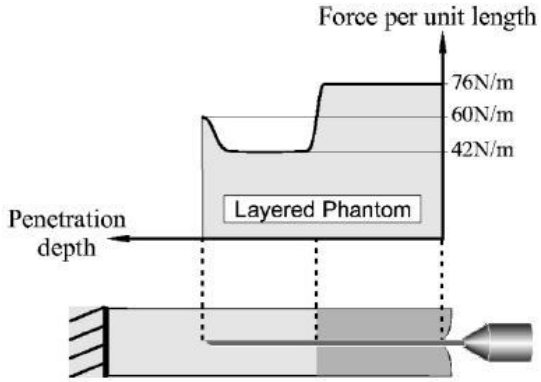

Figure 2.5: Shaft force distribution into inhomogeneous phantom [71]

They could demonstrate the relation between velocity and existing insertion forces. The shaft force is relatively proportional to the insertion velocity while the force peak at the distal end of the needle is noticed to be independent of velocity. Therefore, the shaft force is dominant at higher velocities. Their study is useful for preliminary simulations. However, needle insertion in such artificial

tissue phantoms cannot help to realistically model interactive forces during needle insertion in inhomogeneous and viscoelastic tissue.

The first *in vivo* force/torque measurement for manual needle insertion in human soft tissue is proposed by Podder et al. [77]. They equipped a hand-held adapter with 6-DOF force/torque sensor and a 6-DOF electromagnetic position sensor. They measured force, torque and position during manual needle insertion in a prostate brachytherapy procedure. They also performed *in vitro* needle insertions into beef steak wrapped with chicken skin using a 6-DOF robot. The most comprehensive model is the work presented by Simone and Okamura [71] which confirms results of all above studies.

2.6 Tracking of Needle Navigation

Robotics and medical imaging are employed to overcome the reachability problem of needle insertion. Development of minimally invasive surgery is mostly based on medical imaging. Percutaneous insertion therapy involves inserting the needle into the skin in order to reach local part of a tissue. CT scan and fluoroscope are two main devices used for ultrasound and x-ray imaging.

Magill et al. [78] have constructed a simulator to insert anesthesia needle for training clinicians. They have simulated visco-elastic material of tissue by applying forces on the needle. If trainees place the needle in wrong position, they will receive haptic sensations feedback. Maurin et al. [79] have developed a robotic system to help radiologists by a teleoperation system. This system has a needle driving tool with a haptic interface providing force feedback. The driving tool was actuated to translate and rotate the needle. Fluoroscope provides the clinical capability for realtime needle insertion.

Hagmann et al. [80] have used a haptic system to navigate the surgeon's hand to a clinical target based on CT data. The graphical interface was used to provide tool's trajectory for the surgeon. Hong et al. [81] fabricated a two-degree-of-freedom robot for ultrasound-guided percutaneous cholecystostomy. The robot could correct its path in real time regarding organ deformation or unintended patient movement. The robotic system could serve as an active guidance system.

A passive needle insertion robotic system could be manipulated by the surgeon while robotic kinematic held in a defined position to the patient body. Kronreif et al. [82] developed a robotic system which was manually navigated under supervision of a real-time imaging. The real-time imaging technique can help the surgeon plan the trajectory more conveniently.

High performance computers are required to handle intensive calculations for real time imaging. It should be noted that the accuracy of real time imaging is higher than offline imaging. In general, image-guided surgery is evaluated with three dominant factors: image resolution, image segmentation and augmented reality. In case of absence of real-time imaging, an accurate model for tissue deformation along with force feedback is a proper substitution.

Simulation and modeling of needle insertion have been studied in 2D and 3D environment. DiMaio and Salcudean [7] have presented an interactive simulation of needle insertions in a planar environment. They simulated needle insertion into a flat slab of material. During the simulation, the elastic response of the entire slab is computed using a linear finite element model. As a result, the effects of needle deflection and displacement can also be simulated. This is an improvement over traditional methods which only simulate frictional forces exerted parallel to the needle [83]. They validated their model by comparing the results to measurements of needle insertions made in a slab of soft plastic.

Nienhuys and van der Stappen [65] have proposed a computational technique

to adapt mesh in the region of interest. The geometry of the needle surface was accounted for in the magnitude of frictional forces. They performed simulation in 2D space. Wang et al. [84]developed a method to calculate tissue deformation and approximate needle-tissue interaction to relate model to physical representation. They performed an experiment to calculate seed delivery errors for different needle insertion velocity and depth. Altrovitz et al. [85] have simulated needle insertion for prostate brachytherapy with a 2D model of needle based on dynamic FE analysis by considering effects of the needle tip and frictional forces.

There are many robotic devices developed for percutaneous surgeries. fabricated a compatible manipulator with 3 DOF, and Susil et al. [86] operated the manipulator on anesthetized canines to prove the feasibility and also the accuracy of needle insertion, intra-prostatic injections and fiducial marker placements. For CT guided surgery of prostate biopsy and therapy, Fichtinger et al. [87] explored a needle insertion robotic system to assist the surgeon. Maurin et al. [79] developed a robotic system with parallel combination under CT guidance. Schneider et al. [88] demonstrated a robotic device with integrated ultrasound to insert needle into the prostate, and Ebrahimi et al. [89] presented a hand-held steerable device for needle insertion. Hong et al. [81] built a 7-DOF robotic system under ultrasound guidance. They used a 5-DOF passive arm to place the needle at correct position with respect to the skin and 2-DOF for needle insertion. Their system predicted tissue deformation and organ placement by an image servo system running real time.

Our study investigates methods to enhance the reachability of needle insertion. A robotic device is proposed with enough flexibility to access unreachable areas. Chapter 3 represents the theoretical model of our flexible robotic device for needle insertion.

Chapter 3

Theoretical Modeling of Active Needle

A theoretical model of the active needle is proposed to enhance reachability of needle insertion. The design considerations are discussed,and then, kinematic analysis, dynamic analysis and the active needle implementation are presented in this chapter.

3.1 Design Considerations of Active Needle

Surgical needle insertion is a very challenging issue due to tissue deformation and needle deflection. When the needle is inserted into the tissue, soft tissue deforms and needle deflects as well. It is challenging to steer the needle toward a predefined clinical target and it is more difficult to reach targets deep inside tissue or behind obstacles.

The focus of our research is on the enhancement of reachability of needle insertion with the aid of a flexible robotic device. This robotic device is useful for

reaching targets which are not easily accessible. The target can be called not easily accessible or inaccessible, if it is situated off the insertion path or obstacles exist along the insertion path toward the target.

This study concentrates on insertion of moderately flexible needle for percutaneous therapies. The moderately flexible needle is neither very rigid to remain straight after insertion nor highly flexible to deflect with any inconsiderable external force. This type of needle bends under considerable external forces. Some researchers modelled this type of needle with linear beam elements [45, 46].

3.2 Modeling of Active Needle

The flexible robotic device is called active needle and is designed to improve the reachability problem of needle insertion. The active needle consists of two major parts: main body and closed-loop mechanism. The main body consists of articulated links which are connected together with revolute joints. This structure is composed of n number of links; the first link has one degree-of-freedom (DOF) for forward motion and $n-1$ links are connected together with revolute joints.

The motion is analyzed in 2D workspace. Therefore, each link has three DOFs and the whole system has $3 \times n$ DOFs. Constraints on the motion allow revolution of $n-1$ joints and forward motion of the first link. Thus, 2 DOF of all joints are constrained and total number of DOFs of this system is $3 \times n - 2 \times n = n$. This active needle has adequate DOF to provide flexible movements.

The closed-loop mechanism is used to transfer rotary motion of motor to revolute joints. In the active needle model, actuators are not situated directly on each revolute joint. If actuators are positioned on each revolute joint, the needle will not be suitable for minimally invasive surgeries due to its size limitations. The solution

which has been devised is to place actuators at the first link of the active needle and use a mechanism to transfer this motion to all joints. Despite articulated robots having individual actuators on each joint, the closed-loop mechanism is designed to transfer the motion from a motor located at the base of the needle to all joints.

This mechanism performs at two levels. At the first level, rotary motion of the motor is transferred to reciprocating action of the mechanism. This reciprocating mechanism resembles pull-push cable mechanism. In our design, rigid bars are preferred to cable in a push-push cable mechanism because rigid bars are capable of transferring a larger amount of force compare to cable. At the second level, the reciprocating motion transforms to revolute motion of each revolute joint. Therefore, rotary motion of the motor is transferred to reciprocating motion and then, reciprocating motion is transferred to rotary motion of each joint. Then, the relationship between joints depends on each other. So, the motion of the active needle is restricted.

3.2.1 Kinematic Analysis of Active Needle

Kinematics analysis of the proposed active needle is investigated for a general case. In this case, number of links are considered to be limited. In kinematics modeling, the position and orientation of the end effector is calculated. If joint variables are taken as inputs, the output will be the position of the needle tip. Denavit-Hartenberg representation has been used to express forward kinematics. The presented kinematic modeling is based on works done by Craig [90].

3.2.1.1 Model Description

The active needle robot is modeled with n serial links connected together. Fig. 3.1 represents a special case of the active needle consisted of four links. Generally, nee-

dle tip should be situated in a specific position with one translational actuator and m rotary actuators for revolute joints. m determines number of rotary actuators.

The position of needle tip is expressed by p_x, p_y in the world coordinate system. This world coordinate system is an inertial system attached to the base. The local coordinate system is specified for each joint. First link is actuated along z_0 (local coordinate) by translational actuator. Revolute joints are actuated according to the rotation of previous links.

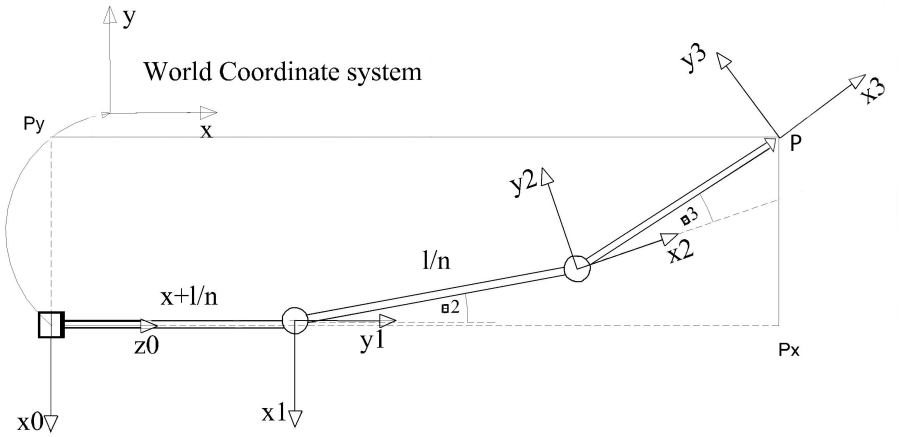

Figure 3.1: Configuration of the active needle model

The end-effector has three independent variables in $2D$ space. A robotic manipulator must have at least three degrees of freedom to locate its end effector at an arbitrary point and arbitrary orientation in space. If number of degree of freedom is greater than three, infinite number of solution may exist to the kinematic equation.

For this model, superposition approach is employed to find the workspace of the active needle. At first, workspace of serial revolute joints are determined. Then, workspace of translational joint is superimposed. Reachable workspace is the locus of needle positions for which the needle tip can reach regardless of its orientation [91]. The reachable workspace of the active needle is shown in Fig. 3.2.

The outer radius of reachable workspace is found by stretching out all the links and the inner radius of circle is found by folding back each link on the other one. A disk with radius of $2L$ is reachable of the active needle (shown with a grey disk in Fig. 3.2). The length of all links is considered to be the same, equivalent to L. Dextrous workspace is the locus of needle positions for which the needle tip can be oriented in all possible orientations. Center of the circle is a single point which represents dextrous workspace (shown with a black point in Fig. 3.2).

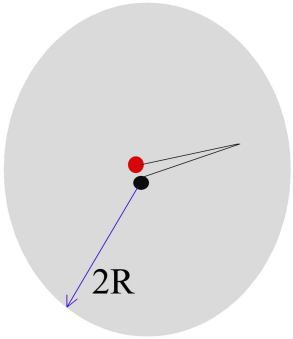

Figure 3.2: Workspace of articulated links of the active needle model

Finally, translational motion of the first link can superimpose to the workspace of rotating links. The workspace of rotating links are shown in Fig. 3.2. If the workspace of prismatic joints is superimposed to the workspace of rotating links, the result will be an oval shape which is elongated along with the diameter of the circle. Fig. 3.3 represents the workspace of the active needle for x translational step. This figure can be elongated by moving the active needle forward with different translational step. This elongation is appeared due to insertion step of the prismatic joint. This workspace is larger than that of serial manipulators with only articulated robotic arms due to its forward motion.

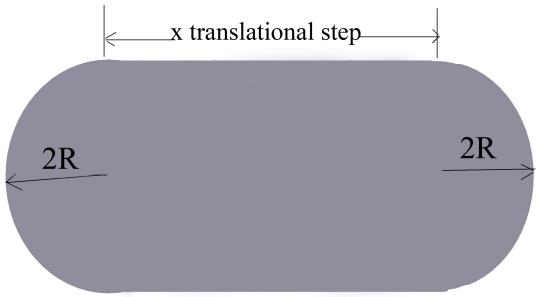

Figure 3.3: Workspace of the active needle; with x translational step

3.2.1.2 Forward Kinematic Analysis

The position of the needle tip in the workspace is calculated by forward kinematics analysis. Needle tip position is determined according to joints' variables. Fig. 3.1 shows the notations of all links, angles and local coordinates of each link used in forward kinematics. To find the transformation matrix of each link and finally the end effector, DH-representation has been assigned for each link:

$$ {}^{i-1}_{i}T = \begin{bmatrix} cos\theta_i & -sin\theta_i cos\alpha_i & sin\theta_i sin\alpha_i & a_i cos\theta_i \\ sin\theta_i & cos\theta_i cos\alpha_i & -cos\theta_i sin\alpha_i & a_i sin\theta_i \\ 0 & sin\alpha_i & cos\alpha_i & d_i \\ 0 & 0 & 0 & 1 \end{bmatrix}. \tag{3.1} $$

By multiplying transfer function of the first link to the next link continuing to the last link, transformation matrix expresses position of end effector in coordinate system of the first link:

$$ {}^{0}_{3}T = {}^{0}_{1}T . {}^{1}_{2}T . {}^{2}_{3}T, \tag{3.2} $$

$$ {}^{0}_{3}T = \begin{bmatrix} -S_{23} & -C_{23} & 0 & -\frac{l}{n}(S_{23}+S_2) \\ 0 & 0 & -1 & 0 \\ C_{23} & -S_{23} & 0 & x+\frac{l}{n}(C_{23}+C_2+1) \\ 0 & 0 & 0 & 1 \end{bmatrix}, \tag{3.3} $$

where $C_{ijk} = cos(\theta_i + \theta_j + \theta_k)$, $S_{ijk} = sin(\theta_i + \theta_j + \theta_k)$ and x is the forward displacement. C and S represent cos and sin functions.

Transformation matrix can be expressed as a combination of all joint's variables. When there are n revolute joints which are being pushed by a translational joint, the transformation matrix (Eq. 3.4) expresses the position of last link of robot in terms of joints' variables:

$$ {}^{0}_{n}T = \begin{bmatrix} -S_{23\ldots n} & -C_{23\ldots n} & 0 & -\frac{l}{n}(S_{23..n}+S_{23\ldots n-1}+\ldots+S2) \\ 0 & 0 & -1 & 0 \\ C_{23\ldots n} & -S_{23\ldots n} & 0 & x+\frac{l}{n}(C_{23\ldots n}+C_{23\ldots n-1}+\ldots+C_2+1) \\ 0 & 0 & 0 & 1 \end{bmatrix}, \tag{3.4} $$

where $C_{23\ldots n} = cos(\theta_2 + \theta_3 + \ldots + \theta_n)$ and similarly, $S_{23\ldots n} = sin(\theta_2 + \theta_3 + \ldots + \theta_n)$. Link 0 refers to the first link of the active needle.

3.2.1.3 Inverse Kinematics

In order to navigate the needle toward a predefined target, joint variables are determined. Needle tip position is inside the workspace of the robot for all orientations during insertion. The order of joint space is greater than that of end effecter's position space. Thus, an iterative algorithm is required to find joints variables.

A wave-traveling path is proposed for steering the active needle. The complete formula of this path will be shown in chapter 4. The simplified format of the path is:

$$y = (x + x^2).sin(kx + wt), \tag{3.5}$$

where $k = 2\pi/\lambda$ and $w = 2\pi/M$. This path should be followed by the active needle model. M as the resolution of motion is equal to 32; λ as the wave length is assumed to be $15cm$ according to the proposed model.

From Eq. 3.5, joint variables are calculated. The first time derivative of this path provides the velocity which rotates the path from the initial position to the next position. The velocity vector is normal to the path because the differentiation is taken with respect to time. This differentiation approximate angular velocity of each joint. The active needle is steered on a specific path which is fixed for every instant and links of the needle should follow that path. It is assumed that each joint has rotating motion with the velocity which can be found from differentiating the path motion. Therefore, $dy/dt(t_f, x = 5cm) = q_2(t_f)$, $dy/dt(t_f, x = 10cm) = q_3(t_f)$ and $dy/dt(t_f, x = 15cm) = q_4(t_f)$. Finally joint variables can be stated as (refer to Appendix A) $q_i(t_f) = \begin{bmatrix} 0.05 \\ 0.01 \\ 0.02 \\ 0.03 \end{bmatrix}$.

After determining final values of all joint variable, a time-variant function is defined for each joint between the initial position, $q(t_0)$, and final position, $q(t_f)$. $q(t)$ represents joint variables over the time (rotating angles and one translational displacement). $q(t)$ is initially situated in zero condition, similarly every angle and displacement equals to zero at $t_0 = 0$. Each joint is considered to be actuated with zero velocity and rests at the end of motion, equivalently $\dot{q}(t_0) = \dot{q}(t_f) = 0$. The value of $q(t_f)$ will be found later for each joint. Thus, four boundary conditions

can be satisfied by a third order polynomial with four unknown parameters:

$$q(t) = q_0 + q_1 t + q_2 t^2 + q_3 t^3. \tag{3.6}$$

After applying boundary conditions (refer to Appendix A):

$$q_i(t) = \frac{3}{t_f^2} q_{if} t^2 - \frac{2}{t_f^3} q_{if} t^3. \tag{3.7}$$

The objective is to find the values of q_{if}. For sliding motion, translational displacement (x) is assumed to be $5cm$ at $t = t_f$ and total duration of the insertion procedure (t_f) is assumed to be $5sec$.

The cubic path planning equation for each joint variable, is determined by substituting these values of $q_i(t_f)$ into Eq. 7.3. Therefore, joint variables are obtained as:

$$\begin{aligned} x(t) &= \frac{3}{5^2}(0.05)t^2 - \frac{2}{5^3}(0.05)t^3, \\ \theta_2(t) &= \frac{3}{5^2}(0.01)t^2 + \frac{2}{5^3}(0.01)t^3, \\ \theta_3(t) &= \frac{3}{5^2}(0.02)t^2 - \frac{2}{5^3}(0.02)t^3, \\ \theta_4(t) &= \frac{3}{5^2}(0.03)t^2 - \frac{2}{5^3}(0.03)t^3. \end{aligned} \tag{3.8}$$

By calculating four variables in every $5sec$ interval, the end effector position can be found with transformation matrix (Eq. 3.1). Inverse kinematics problem can be solved with neural network. Traditional methods for solving IKS problem are geometric, algebraic and iterative methods. Traditional methods are inapplicable to be used for generalized m degrees of freedom manipulators due to its complexity in mathematical formulation.

It should be noted that the driving closed-loop mechanism requires a complete kinematics analysis. This mechanism is the closed-loop with parallel actuators.

The kinematic analysis of the closed-loop mechanism is not discussed in this research. The relation between kinematics of the closed-loop mechanism and that of the main body requires to be found. Kinematic analysis of the closed-loop mechanism constrains the motion of joints and then, joint variable will be dependant. The dependency of joints on each other can be found by solving the closed-loop mechanism. In this section, forward kinematic analysis is focused on articulated links of the main body.

3.2.1.4 Velocity Analysis

Velocity analysis determines velocity of needle tip with respect to the velocity of joints. The instantaneous kinematic relationship between the velocity of the joint and that of the end-effector is generally expressed by:

$$\dot{q} = J\dot{p}, \tag{3.9}$$

where $\dot{q}$ is the vector of rate of change in joint variables, J is the Jacobian matrix expressed in the world coordinate system, and $\dot{p}$ is the vector of rate of change in end effector variables. $\dot{p} = [v, w]^T = [\dot{x}, \dot{y}, \dot{z}, w_x, w_y, w_z]^T$, where v is the vector of translational velocity and w is the vector of rotational velocity about the body axis of the end effector.

The manipulator Jacobian also describes the relationship between wrenches employed at the end-effecter and joints' torques. The relationship between a spatial wrench F applied at the end-effecter and the corresponding torques is $\tau = J^T F$. A planar space is assumed to determine the Jacobian Matrix for the end-effector. End effector's position is expressed in the world coordinate system. Needle tip position (x_p, y_p) is specified in terms of joint variables. Mathematical relations are

derived according to geometry which is shown in Fig. 3.1.

$$x_p(x,\theta_2,\theta_3,\theta_4) = x+L(C_{234}+C_{23}+C_2+1) y_p(\theta_2,\theta_3,\theta_4) = L(S_{234}+S_{23}+S_2), \quad (3.10)$$

where x is translational displacement and $\theta_2, \theta_3, \theta_4$ are rotational displacement of joints. To obtain velocity vector, differentiation of position vector is calculated:

$$dx_p = \frac{\partial x_p}{\partial x}.dx + \frac{\partial x_p}{\partial \theta_2}.\theta_2 + \frac{\partial x_p}{\partial \theta_3}.\theta_3 + \frac{\partial x_p}{\partial \theta_4}.\theta_4, \quad (3.11)$$

$$d\mathbf{x} = \mathbf{J}\mathbf{dq}, \quad (3.12)$$

where $d\mathbf{x} = \begin{bmatrix} dx_p \\ dy_p \end{bmatrix}$, $d\mathbf{q} = \begin{bmatrix} dx \\ d\theta 2 \\ d\theta 3 \\ d\theta 4 \end{bmatrix}$ and $J = \begin{bmatrix} \frac{\partial x_p}{\partial x} & \frac{\partial x_p}{\partial \theta_2} & \frac{\partial x_p}{\partial \theta_3} & \frac{\partial x_p}{\partial \theta_4} \\ \frac{\partial y_p}{\partial x} & \frac{\partial y_p}{\partial \theta_2} & \frac{\partial y_p}{\partial \theta_3} & \frac{\partial y_p}{\partial \theta_4} \end{bmatrix}$.

Jacobian$J$ relates the needle tip displacement $d\mathbf{x}$ to joints' displacements $d\mathbf{q}$ which is defined as:

$$J = \begin{bmatrix} 1 & -L(S_{234}+S_{23}+S_2) & -L(S_{234}+S_{23}) & -LS_{234} \\ 0 & L(C_{234}+C_{23}+C_2) & L(C_{234}+C_{23}+C_2) & L(C_{234}+C_{23}) \quad LC_{234} \end{bmatrix}. \quad (3.13)$$

In order to perform a given task, a robot must have enough DOFs to reach the predefined destinations. A kinematically redundant manipulator has more than minimal number of DOFs required to complete a set of tasks. A redundant manipulator has an infinite number of joints' configurations which result in the same end-effecter configuration. The extra DOFs in redundant manipulators can be used to avoid obstacles, to solve kinematic singularities or to optimize the motion of a manipulator relative to a cost function.

The manipulator Jacobian can also be used to relate joints' torques to end-

effecter's wrenches for redundant manipulator. Redundant manipulator is free to move even if the end effecter is fixed. In particular, the possible existence of internal motions, with the inertial coupling between the links, causes forces to be applied to end-effecter even if no torque is applied on joints. While a redundant manipulator is in static equilibrium, the previous relationship, $\tau = J^T F$ still holds.

Redundancy of a system can be calculated by finding the difference $n-m$, where n represents DOF of system and m expresses number of independent variables of end effecter. In the active needle model, DOF is equal to number of links, and the value of m in $2D$ motion plane of needle is equal to three. For instance, if the active needle has four links, the redundancy of whole system is one degrees. Therefore, the active needle model has more degrees of freedom required to perform a task or a set of tasks. Furthermore, the model provides more flexibility to avoid obstacles and possible singularities in the system. The redundancy problem is not studied for our case study; because the three-link active needle is studied in this thesis. For the proposed active needle has no redundancy. The velocity analysis has also been addressed in section 3.2.1. The required force applying on the end effector can be determined from "Modeling Insertion Forces" section of chapter 2.

3.2.2 Dynamic Analysis of Active Needle

Dynamics of motion analyzes forces and acceleration of links. In order to determine required forces to accelerate and decelerate links, lagrangian dynamic formulation is used. Lagrangian dynamic formulation is an energy based method.

The Lagrangian dynamic formulation provides a means of deriving the equations of motion from a scalar function called Lagrangian. Lagrangian is defined as the difference between kinetic and potential energy of the active needle. The

Lagrangian of an articulated robotic system is defined by:

$$L(q, \dot{q}) = k(q, \dot{q}) - u(q). \tag{3.14}$$

The equation of motion of the active needle is given by:

$$\frac{d}{dt}\frac{\partial L}{\partial \dot{q}} - \frac{\partial L}{\partial q} = \tau, \tag{3.15}$$

where τ is $n \times 1$ vector of actuator torque. In the case of the active needle, this equation can be expressed as:

$$\frac{d}{dt}\frac{\partial k}{\partial \dot{q}} - \frac{\partial k}{\partial q} = \tau. \tag{3.16}$$

The dynamic equation can be expressed in joint space dynamics [90]:

$$D(q)\ddot{q} + C(q, \dot{q})\dot{q} + G(q) = \tau, \tag{3.17}$$

where $C(q, \dot{q})\dot{q}$ is a vector of coriolis and centrifugal forces and $G(q)$ is a vector of gravitational forces.

The kinetic energy of linear and angular motion of each link is determined. Total kinetic energy of system is obtained by the summation of kinetic energy of individual links:

$$k = \sum_{i=1}^{n} k_i, \tag{3.18}$$

where k represents the kinetic energy.

The kinetic energy of the active needle can be described by a scalar formula as a function of joint position θ and velocity $\dot{\theta}$, $k(\theta, \dot{\theta})$. In fact, kinetic energy is given by:

$$k(\theta, \dot{\theta}) = \frac{1}{2}\dot{\theta}^T D(\theta)\dot{\theta}, \tag{3.19}$$

where $D(\theta)$ is an $n \times n$ inertia matrix. This quadratic expression can be expressed in generalized coordinates. In generalized coordinate system, generalized displacement (q) is angular displacement for rotary joint or linear displacement for prismatic joint. Similarly, generalized velocity ($\dot{q}$) is either the angular velocity for rotary joint or linear velocity for prismatic joint. Then, kinematic energy can be expressed in generalized coordinate system by:

$$k(q, \dot{q}) = \frac{1}{2}\dot{q}^T D(q)\dot{q}. \tag{3.20}$$

The total potential energy stored in the individual links is:

$$u = \sum_{i=1}^{n} u_i. \tag{3.21}$$

If the active needle moves in a horizontal plane, potential energy is zero. On the other hand, if the active needle moves in vertical plane, change in elevation of motion is very small. Thus, potential energy of the active needle is not considered in our analysis.

In order to solve dynamic analysis, position and velocity of center of mass of each link is found with respect to the base coordinate system. Then, kinetic energy is calculated for the center of mass of each link, to find the expression of inertia matrix $D(\theta)$. Finally, the Lagrangian equation is determined.

Center of mass of each link of the active needle is assumed to be on the middle of each link. The reference coordinate system is the world coordinate system on the base (Fig. 3.1). The forces act on needle tip F could be applied by the actuators at joints by using the relationship:

$$\tau = J^T(q)F, \tag{3.22}$$

where Jacobian is already determined in "Velocity Analysis" section.

3.2.2.1 Identification of center of mass Position and Velocity for Each Link

The center of mass is determined for each link of the active needle with respect to the coordinate system on the fist link. All links have the same length L. Center of mass position of each link is expressed by x and y:

$$
\begin{aligned}
&Link1: \\
&\quad x_1 = L + \frac{L}{2}cos(\theta_1) \\
&\quad y_1 = \frac{L}{2}sin(\theta_1), \\
&Link2: \\
&\quad x_2 = L + Lcos(\theta_1) + \frac{L}{2}cos(\theta_1 + \theta_2) \\
&\quad y_2 = Lsin(\theta_1) + \frac{L}{2}sin(\theta_1 + \theta_2), \\
&Link3: \\
&\quad x_3 = L + Lcos(\theta_1) + Lcos(\theta_1 + \theta_2) + \frac{L}{2}cos(\theta_1 + \theta_2 + \theta_3) \\
&\quad y_3 = Lsin(\theta_1) + Lsin(\theta_1 + \theta_2) + \frac{L}{2}sin(\theta_1 + \theta_2 + \theta_3).
\end{aligned}
\tag{3.23}
$$

Derivatives of position vectors provides velocity for mass center of each link:

$Link1:$

$$\dot{x}_1 = -\frac{L}{2}sin(\theta_1)\dot{\theta}_1$$
$$\dot{y}_1 = \frac{L}{2}cos(\theta_1)\dot{\theta}_1,$$

$Link2:$

$$\dot{x}_2 = -Lsin(\theta_1)\dot{\theta}_1 - \frac{L}{2}sin(\theta_1+\theta_2)(\dot{\theta}_1+\dot{\theta}_2)$$
$$\dot{y}_2 = Lcos(\theta_1)\dot{\theta}_1 + \frac{L}{2}cos(\theta_1+\theta_2)(\dot{\theta}_1+\dot{\theta}_2),$$

$Link3:$

$$\begin{aligned}\dot{x}_3 &= -Lsin(\theta_1)\dot{\theta}_1 - Lsin(\theta_1+\theta_2)(\dot{\theta}1+\dot{\theta}_2) - \frac{L}{2}sin(\theta1+\theta2+\theta3)(\dot{\theta}_1+\dot{\theta}_2+\dot{\theta}_3)\\ \dot{y}_3 &= Lcos(\theta_1)\dot{\theta}_1 + Lcos(\theta_1+\theta_2)(\dot{\theta}_1+\dot{\theta}_2) + \frac{L}{2}cos(\theta_1+\theta_2+\theta_3)(\dot{\theta}_1+\dot{\theta}_2+\dot{\theta}_3).\end{aligned} \tag{3.24}$$

Velocity of mass center of each link is obtained by $v_i^2 = \dot{x}_i^2 + \dot{y}_i^2$. Therefore,

$$\begin{aligned}v_1^2 =& \frac{L^2}{4}\dot{\theta}_1^2\\ v_2^2 =& L^2\dot{\theta}_1^2 + \frac{L^2}{4}(\dot{\theta}_1^2+\dot{\theta}_2^2)^2 + L^2cos(\theta_1)\dot{\theta}_1(\dot{\theta}_1+\dot{\theta}_2)\\ v_3^2 =& L^2\dot{\theta}_1^2 + L^2(\dot{\theta}_1+\dot{\theta}_2)^2 + \frac{L^2}{4}(\dot{\theta}_1+\dot{\theta}_2+\dot{\theta}_3)^2 + 2L^2cos(\theta_1)\dot{\theta}_1(\dot{\theta}_1+\dot{\theta}_2)\\ &+ L^2cos(\theta_3)(\dot{\theta}_1+\dot{\theta}_2)(\dot{\theta}_1+\dot{\theta}_2+\dot{\theta}_3)\\ &+ L^2cos(\theta_2+\theta_3)(\dot{\theta}_1)(\dot{\theta}_1+\dot{\theta}_2+\dot{\theta}_3).\end{aligned} \tag{3.25}$$

3.2.3 Lagrangian Equation of Active Needle

The kinetic energy of each link is determined by $k_i = \frac{1}{2}m_i v_i^2$ and total energy can be found by Eq. 3.18. The first link of the active needle moves with constant insertion velocity $\dot{x}$. Total kinetic energy is summation of kinetic energy of first link with kinetic energy of second, third and forth links. Thus, total kinetic energy

is expressed by:

$$k = \frac{1}{2}m_0\dot{x}^2 + \frac{1}{2}m_1v_1^2 + \frac{1}{2}m_2v_2^2 + \frac{1}{2}m_3v_3^2, \tag{3.26}$$

where m_0 is the mass of first link, and m_1, m_2, m_3 are masses of the second, third and forth links, respectively. It is common to express total kinetic energy in quadratic matrix format, $k = \frac{1}{2}\dot{q}^T D(q)\dot{q}$. Inertia matrix $D(q)$ can be extracted from quadratic form of total kinetic energy.

$$k_{total} = \frac{1}{2}\dot{q}^T \begin{pmatrix} m_0 & 0 & 0 & 0 \\ 0 & k_{22} & k_{23} & 2m_3L^2(\frac{1}{2} + cos(\theta_3) + cos(\theta_2 + \theta_3)) \\ 0 & k_{32} & k_{33} & 2m_3L^2(\frac{1}{2} + cos(\theta_3)) \\ 0 & k_{42} & k_{43} & m_3\frac{L^2}{4} \end{pmatrix} \dot{q}. \tag{3.27}$$

where $k_{22} = m_1\frac{L^2}{4} + m_2L^2(\frac{5}{4} + cos(\theta_2)) + m_3L^2(\frac{9}{4} + cos(\theta_2) + cos(\theta_3) + cos(\theta_2 + \theta_3))$,

$k_{23} = 2m_2L^2cos(\theta_2) + 2m_3L^2(\frac{5}{4} + cos(\theta_2) + cos(\theta_3) + cos(\theta_2 + \theta_3))$,

$k_{32} = 2m_2L^2cos(\theta_2) + 2m_3L^2(\frac{5}{4} + cos(\theta_2) + cos(\theta_3) + cos(\theta_2 + \theta_3))$,

$k_{33} = m_2\frac{L^2}{4} + m_3L^2(\frac{5}{4} + cos(\theta_3))$,

$k_{42} = 2m_3L^2(\frac{1}{2} + cos(\theta_3) + cos(\theta_2 + \theta_3))$,

$k_{43} = 2m_3L^2(\frac{1}{2} + cos(\theta_3))$.

The expression for inertia matrix $D(q)$ is determined by Eq. 3.20. The general lagrangian formulation can be expressed by Eq. 3.17. Coriolis and centrifugal forces are obtained by:

$$C_{kj} = \sum_{i=1}^{n} C_{ijk}\dot{q}_i, C_{ijk} = \frac{1}{2}(\frac{\partial d_{kj}}{\partial q_i} + \frac{\partial d_{ki}}{\partial q_j} - \frac{\partial d_{ij}}{\partial q_k}). \tag{3.28}$$

Therefore, matrix C is determined by differentiation of inertia matrix $D(q)$:

$$\begin{bmatrix} 0 & 0 & 0 & 0 \\ 0 & c_{22} & c_{23} & c_{24} \\ 0 & c_{32} & c_{33} & c_{34} \\ 0 & c_{42} & c_{43} & c_{44}, \end{bmatrix}, \tag{3.29}$$

where $c_{22} = (-m_2L^2sin(\theta_2) - m_3L^2(sin(\theta_2) + sin(\theta_2 + \theta_3)))\dot{\theta}_3 - (m_3L^2(sin(\theta_3) + sin(\theta_2 + \theta_3)))\dot{\theta}_4$,

$c_{23} = (-m_2L^2sin(\theta_2) - m_3L^2(sin(\theta_2) + sin(\theta_2 + \theta_3)))\dot{\theta}_2 + (-4m_2L^2sin(\theta_2) - 4m_3L^2(sin(\theta_2) + sin(\theta_2 + \theta_3)))\dot{\theta}_3 + (-2m_3L^2(sin(\theta_3) + 2sin(\theta_2 + \theta_3)))\dot{\theta}_4$,

$c_{24} = (-m_3L^2(sin(\theta_2) + sin(\theta_2 + \theta_3)))\dot{\theta}2 - 2m_3L^2(sin(\theta_3) + 2sin(\theta_2 + \theta_3))\dot{\theta}_3 - 4m_3L^2(sin(\theta_3) + sin(\theta_2 + \theta_3)\dot{\theta}_4)$,

$c_{32} = (m_2L^2sin(\theta_2) + m_3L^2(sin(\theta_2) + sin(\theta_2 + \theta_3)))\dot{\theta}_2$,

$c_{33} = (-m_3L^2sin(\theta_3))\dot{\theta}_3 + (-m_3L^2sin(\theta_3))\dot{\theta}_4$,

$c_{34} = -2m_3L^2sin(\theta_3)\dot{\theta}_2 - m_3L^2sin(\theta_3)\dot{(\theta_3)} - 4m_3L^2sin(\theta_3)\dot{\theta}_4$,

$c_{42} = (m_3L^2(sin(\theta_3) + sin(\theta_2 + \theta_3)))\dot{\theta}_2 + (2m_3L^2sin(\theta_3))\dot{\theta}_3$,

$c_{43} = (2m_3L^2sin(\theta_3))\dot{\theta}_2 + (m_3L^2sin(\theta_3))\dot{\theta}_3$.

The Lagrangian dynamic equation is obtained by substitution of $D(q)$ and $C(q, \dot{q})$ into Eq. 3.17. In this equation $q = [\dot{x}, \dot{\theta}_1, \dot{\theta}_2, \dot{\theta}_3]^T$ and $\dot{q}$ is the derivative of q matrix. This formulation describes dynamic analysis of the main body of the active needle. The closed-loop mechanism constraints the motion of revolute joints. The relation between revolute angles and their angular displacement can be investigated in further research.

3.3 Implementation of Active Needle

Implementation of the active needle deals with two subjects: size and flexibility. The active needle should be small enough to be suitable for minimally invasive surgery. In addition, the active needle should be very flexible to improve reachability of needle insertion. The flexibility of the active needle influences the size of the needle and requires a larger actuating system with a larger needle. The active needle is a proposed robotic device which enhances flexibility of needle insertion with a small actuation system. There is a compromise between the size of the robotic device and its flexibility.

The idea of the active catheter inspired a great motivation to develop the active needle model (Fig. 3.4). Mineta et al. [92] developed a new batch fabrication process of a shape memory alloy (SMA) sheet based on electrochemical pulse etching. A bending mechanism of an active catheter of about $0.8mm$ in outer diameter could be fabricated using three at meandering SMA actuators. Glozman and Shoham [45] commented that the size of active catheter actuators is not suitable for needle navigation; however, this is not proven.

Figure 3.4: Small diameter active catheter using shape memory alloy coils [93]

The proposed active needle should be as flexible as an active catheter with a special driving system. This driving system reduces the size of the needle. A moderately flexible needle is studied in this research; this type of needle has enough

flexibility as well as sufficient stiffness. Although the needle should be reasonably flexibile, it should be stiff enough to puncture the soft tissue. The idea of active

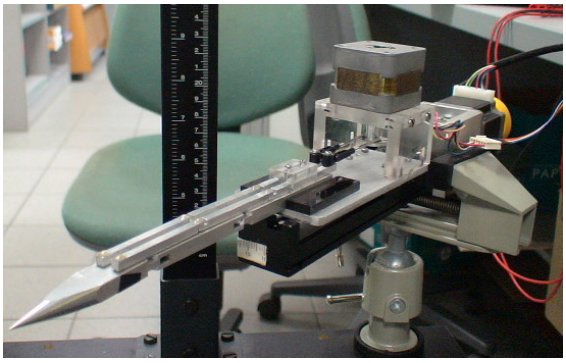

Figure 3.5: Prototype active needle device

needle improves flexibility of needle by adding joints to a long needle and using a symmetric tip instead of a bevel tip. Conical or triangular tip are types of needles with symmetric tip which can cause the needle to bend less comparing to bevel tip needle [73]. Active needle is made of two mechanical subsystems connected together: main body and closed-loop mechanism. Active needle device is shown in Fig. 3.5.

For our prototype (Fig. 3.6), the main body is a open-loop system with three links connected together with revolute joints (see Fig. 3.1). Total length of three links is 20 cm. The needle is fabricated with a rectangular cross-section ($7cm \times 15cm$). Density of Aluminium is $2.7kg/mm^3$ and Young's modulus(E) is equal to 70000 Mpa. The first link of the main body is connected to stepper motor which provides insertion motion for the needle. Stepper motor with the resolution of 1.8 degree is controlled by a driver. The driver is connected to DAQ hardware which is an interface between the driver and Labview program.

Labview's programming environment consists of two main windows, the Front Panel (FP) and the Block Diagram (BD). The FP provides users interfaces to the program where the inputs and outputs to the program are indicated by various

animation items like knobs, push buttons or LEDS. The BD is where the graphical code is written with all the wires representing the flow of data among function blocks.

Another actuator is required for swim-wave motion of the needle. The rotary motion of this motor is transferred to reciprocating motion of the closed-loop mechanism. The closed-loop mechanism is a driving system to produce swim-wave motion of the active needle. The reciprocating motion is pushing bars of the mechanism on one side of the motor and at the same time, pulling bars of the mechanism on the other side of the motor. Thus, the motor should be powerful enough to produce required torque. A stepper motor is selected with specifications of 4V and 0.6A.

Labview programming controls the motion of these two stepper motors: one motor for the forward motion and another for the swim-wave motion. In order to calculate number of steps, current position of the needle is saved into variables; next position for the motor is read from input values and subtracted from current position. By knowing the sign of subtraction, direction of rotation of motor can be determined. Then, the motor will rotate to next position, clockwise or counter clockwise regarding the sign of subtraction.

For the closed-loop mechanism (see Fig. 3.6), a pulley is mounted on the stepper motor for swim-wave motion to transfer rotary motion of the motor to translational motion. This translational motion is connected to rectangular bars. These bars have pins on both ends which slides in slots grooved inside the main body of the active needle. Each bar has a pair which has the opposite motion of its pair; i.e. the bar on right side of the motor is pushed forward while its pair on the left side is pulled backward.

With the driving closed-loop mechanism, the motion is transferred form the rotary motor at the base of the first link, to revolute joints. The main advantage of

this mechanism is that actuators are placed at the end of the first link. Therefore, the active needle's size is not constrained by the size or position of the actuators. Micro fabrication may have great contributions to reduce the size of the active needle. In Appendix B, all drawings for the active needle prototype are presented.

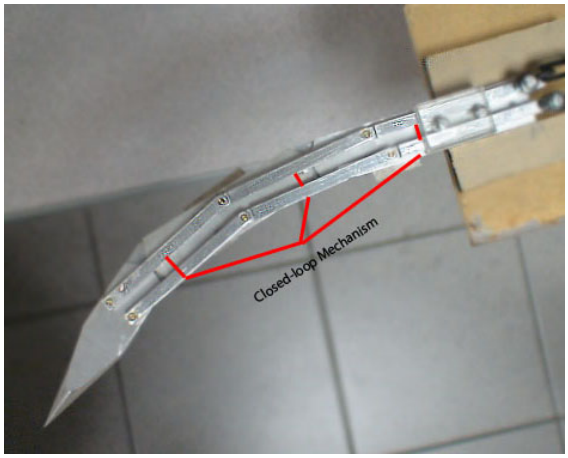

(a) Closed-loop mechanism consists of three parallel bars

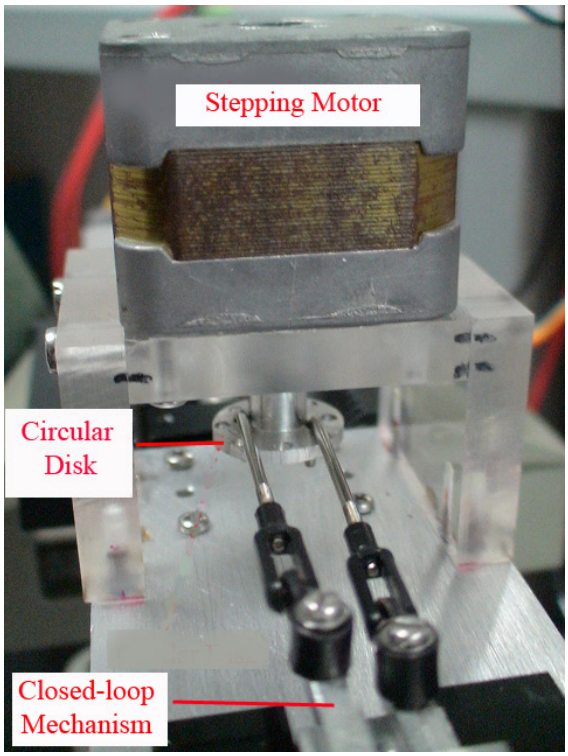

(b) Pulley mounted on stepper motor to transfer motion to the closed-loop mechanism

Figure 3.6: Closed-loop mechanism

Chapter 4

Motion Path Planning and Simulation

A path is proposed to be flexible enough to avoid obstacles in the way of needle insertion toward the target. The path parameters are related to the dynamics of the active needle. The active needle follows the proposed path and path parameters are optimized with respect to energy minimization method.

4.1 Motion Planning

A patient treatment can be improved with the aid of motion planning and medical robotics. The patient's data can be acquired from medical images and clinical criteria. Medical imaging techniques indicate the position of the target. Then, motion planning provides proper information to find a path which navigates the needle to the predefined clinical target based on acquired data. Path planning problem is addressed in this research by proposing a flexible path for the active needle model.

The proposed path is flexible enough to avoid obstacles exist around the insertion path. The active needle is properly designed to follow this proposed path. The active needle is modeled by linear beam elements by which the path can be followed. Needle-tissue interaction forces constrain the needle's motion. Therefore, the interaction forces are modeled by spring-damper elements, in order to find the optimal path.

A path is called optimal if it requires minimum energy for needle navigation. In order to follow an optimal path, linear beam elements of the active needle bend under application of external forces. The required energy for bending the needle should be minimized. The bending energy will be transferred to the surrounding tissue of the needle and will consequently cause injury to the patient. By minimizing the bending energy, tissue injury and recovery time will be reduced. At final stage of patient treatment, the medical robot can be steered with the acquired information from motion planning.

4.1.1 Identification of the Path

For path planning, the active needle is modeled by linear beam elements. These elements are considered as fish elements with great flexibility and manoeuvrability. An analogy is performed between fish motion in a viscous environment and the active needle model in a visco-elastic tissue. The visco-elastic environment inside the tissue is similar to the viscous environment of the robotic fish. Fish motion is naturally efficient and flexible. Beneficial and efficient characteristics of fish locomotion brought out the idea of utilizing fish elements in modeling the active needle. The governing equation of the swimming mode of a fish is applied to linear beam elements of the active needle.

In order to propose a path for needle insertion, a sinusoidal function is suggested

with two variables: time t and the needle tip's position x. Eq. 4.1 is a traveling-mode wave motion of the body of a fish (suggested by Lighthill in 1960):

$$y(x,t) = (c_1 x + c_2 x^2) sin(kx + wt). \tag{4.1}$$

Eq. 4.1 is an appropriate choice for path planning of the active needle. However, it should be modified according to our desirable strategy for path planning. Modification of path parameters are based on two main concerns: soft tissue force constraint and energy minimization of motion.

The needle-tissue interaction forces constrain the maneuverability of the proposed path. During post-puncture, friction, cutting and collision with interior structures are the main reasons which alter the magnitude of needle insertion force [73]. Chui et al. [94] addressed the assumption of one known force at the point of contact between the needle tip and the tissue. Although complex forces on the needle are not known, the force at the needle tip can be measured by force sensors. It should be noted that the needle tip's force varies with depth of insertion. Experiments are required to determine the value of forces acting on the needle for each insertion depth.

Generally, friction and cutting forces are major force components which oppose steering the needle inside the tissue. However, frictional forces applied by a constraint surface or a constraint environment is unable to impose any constraint because it is always tangent to the surface [95]. In addition, frictional forces can be compensated with a larger forward motion from the base of the robot. Therefore, only cutting forces constrain the needle's motion. The cutting forces can bend the needle and then, the needle applies force on the surrounding tissue. Minimization of the bending energy is a major concern of this path planning.

4.1.2 Modification of the Proposed Path

The path of our active needle is the track of the needle tip's position and this position is time-variant; therefore, the deflection curve in Eq. 4.2 implicitly vary with time. Eq. 4.2 expresses the path of motion, unlike Eq. 4.1 which describes the motion of the robot. Therefore, the path of the motion is separated from general wave Eq. 4.1:

$$y(x) = (c_1 x + c_2 x^2) sin(kx), \tag{4.2}$$

where x is the position of the needle tip which is a function of time. k represents the wave number, and c_1, c_2 are constant coefficients.

The proposed path of the needle is a sine function which can overpass obstacles existing in the way of needle insertion to the target. In other words, the trend of a sine function is compatible with our objective to proceed to the predefined target and move around possible obstacles. At early stages of needle insertion, a straight line is required to penetrate into tissue and move forward. Then, a curve path is required to overpass the first encountering obstacle and come back to the same alignment with the insertion line.

In a primitive case, it is assumed that no obstacle exists around the target (as shown in Fig. 4.1). However, the clinical target is not aligned with the insertion line. Therefore, a curve path is required to reach the clinical target. A sine function has the ability to cause the active needle to pass over an obstacle and then come back to the same alignment with the insertion line.

The amplitude of the proposed path is a quadratic polynomial because it can provide a proper motion in early stages of the insertion procedure. This quadratic polynomial has the ability to damp the amplitude of the needle's path in shallow insertion depth by assigning appropriate values for coefficients c_1 and c_2. By inserting the needle deeper inside the tissue, the second order term ($c_2 x^2$) becomes more

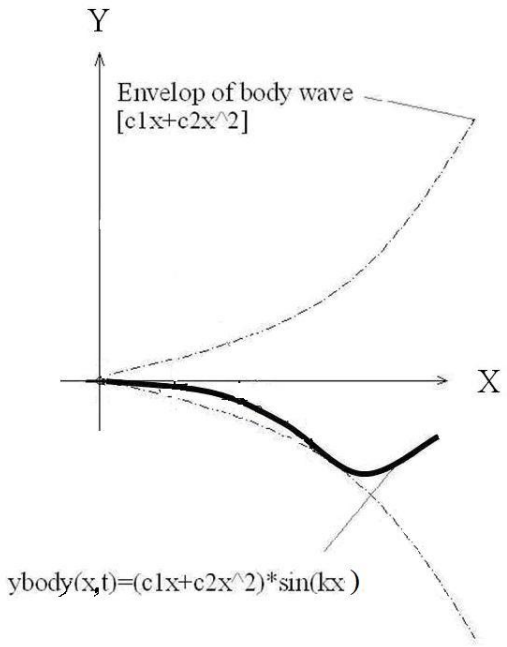

Figure 4.1: Implementation of the proposed motion path

dominant than the first order term ($c_1 x$). Then, the path increases its curvature to reach targets situated off the needle insertion line for larger insertion depth.

The suggested theoretical model of the active needle is consisted of individual rigid links connected together with revolute joints which enable the needle to be flexible enough to take the shape of a sine function in Eq. 4.2. The wave number k is equal to $\frac{2\pi}{\lambda}$, where λ is the body wave length. The wave frequency of the physical needle model should be the same as that of the path. The active needle should have enough rotating links to produce same body wave length. So, parameter k of the path has a physical meaning of the mechanical model of the active needle.

4.1.3 Identification of Optimal Path

The proposed path is optimized based on energy minimization method. This optimization is constrained by needle-tissue interaction forces. Interaction forces are

modeled to set constraint for the optimal path. Cutting forces acting on the needle are elastic forces which are constraints of optimization problem. These forces are modeled by mass-spring model [47], [63], [64]. A well established mass-spring model is Kelvin Model (Fig. 4.2), which is a standard linear model with the ability of decent approximation of the tissue visco-elasticity behavior.

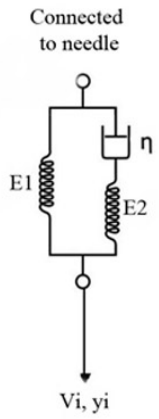

Figure 4.2: Modeling visco-elastic material of soft tissue with Kelvin Model

The elastic forces of soft tissue which are calculated according to displacement of the needle, expressed by:

$$V_i = y_i(E_1 + E_2 + \frac{E_2^2}{\eta}.exp(-\frac{E_2}{\eta}.\tau)), \tag{4.3}$$

where V_i is the cutting force of the needle tip for every instant of time, y_i is the displacement of the needle tip for every instant of time, $E_1 and E_2$ are the stiffness of tissue, η is the damping ratio of tissue, and τ is the relaxation time.

The active needle is modeled by linear beam elements and the cutting force V_i represents shear forces exerted by the tissue on the needle [45]. The relationship between shear forces and displacement is represented by:

$$V_i = EI\frac{d^3y_i}{dx^3}, \tag{4.4}$$

where E is the modulus of elasticity, I is the moment of inertia and EI is the flexural rigidity of the needle which is constant along the length of the needle. V_i is substituted form Eq. 4.4 to Eq. 4.3 to obtain:

$$EI((\frac{6c_2k}{c_1x+c_2x^2}-k^3)cot(kx)-3k^2.\frac{c_1+2c_2x}{c_1x+c_2x^2})-(E_1+E_2+\frac{E_2^2}{\eta}exp(\frac{-E_2^2}{\eta}\tau))=0. \tag{4.5}$$

After determining constraint equation (Eq. 4.5), the proposed path is optimized based on bending energy minimization. The bending energy is required to deflect the beam elements of needle inside the tissue. The energy of this bending moment is calculated by $U_{energy}=\int\frac{M^2}{2EI}dx$, where M is the bending moment caused by the transverse load. Knowing that $M=EI.frac\partial^2y\partial x^2$, energy can be expressed by:

$$U_{energy}=\frac{EI}{2}\int_0^x((2c_2-k^2(c_1x+c_2x^2))sin(kx)+(2k(c_1+2c_2x))cos(kx))^2dx. \tag{4.6}$$

An optimization tool is selected to minimize the bending energy (Eq. 4.6) by considering forces acting on needle tip. The objective is to determine the three parameters (c_1, c_2, k) in order to determine the optimal path of the needle.

The needle insertion depth is assumed to between 25cm to 30cm. The forward motion of needle insertion is broken into small increments. For each increment, forces acting on the needle tip is calculated and the energy is minimized for each path according to the forces. It should be noted that the value of elastic forces in Eq. 4.3 is changing with variable x for each increment of insertion.

Optimization toolbox of MATLAB solves function minimization problem according to constraints. The optimization results should be reasonable for the proposed active needle. Reasonable value of wave body length λ is determined by the mechanical structure of the active needle. As the active needle should follow the

proposed path, wave length λ can be determined by the length of rotating links of the model. Total length of rotating links is between 5cm and 15cm. Thus, acceptable range for body wave number k is determined to be between 20 and 120.

4.2 Simulation

The optimization algorithm is set and the path is simulated considering elastic forces constraint for each sequence. Kelvin model's properties are assumed to be unity (properties are shown in Fig.4.2) for faster convergence. Three parameters c_1, c_2 and k are initialized to start the optimization method. Then, optimization method is processed for every $1cm$ of needle insertion and theses parameters are updated for each insertion step. The updated values of each insertion step provide the minimum energy path for the next motion.

Constraint equation of forces is considered in each iteration. The optimization method is acceptable when the parameter k is between 20 and 120 and parameters c_1 and c_2 to be less than unity to provide a straight path in early stages of insertion. The optimization runs 100000 iterations for each insertion sequence by considering elastic forces constraint.

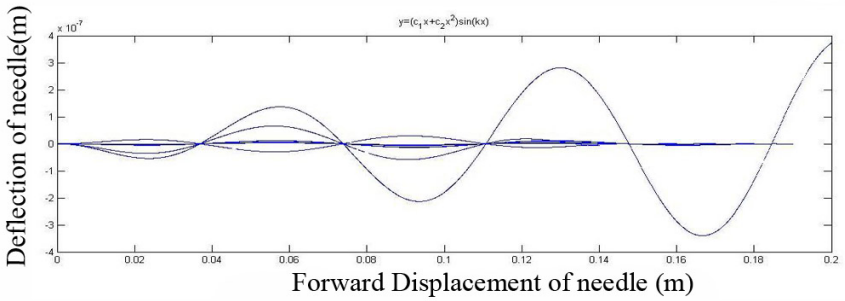

Figure 4.3: Simulation result for needle insertion, 1cm increment, until 20cm depth

Optimization converges from the beginning of insertion until x reaches 24cm with 1cm increment. The parameters are optimized for this insertion depth($c_1 = 0.01, c_2 = -0.04, k = 71$). After minimizing equation of energy (4.6) by considering constraint equation (4.5) with the proposed methodology for optimization, the proposed path of the active needle is obtained by:

$$y = (0.01x - 0.04x^2)sin(71x). \tag{4.7}$$

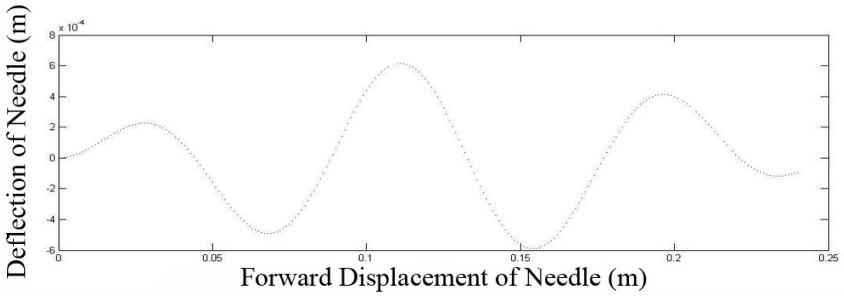

Figure 4.4: Simulation results for insertion depth of 24cm

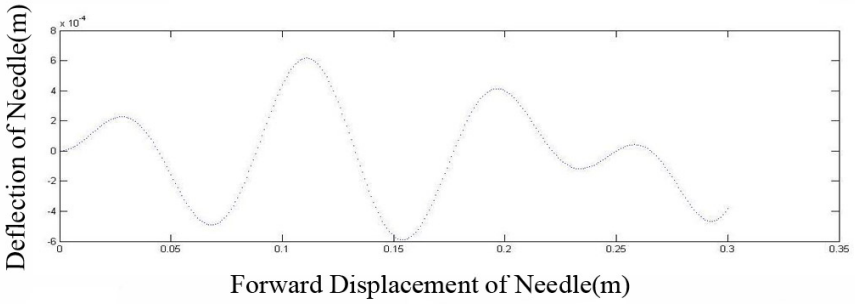

Figure 4.5: Simulation results for insertion depth of 30cm

The path is updated after calculating constraint forces for each insertion step because constraint forces are unknown ahead of time. The simulation result shows small deflection of the needle(in order of $0.1mm$). The final result is the optimum

path with small deflection. The path planning proposes a path as a criteria for needle insertion. In chapter 7, results and limitations are completely discussed.

Chapter 5

Active Needle Simulation using SimMechanics

In this chapter, simulation of the active needle is investigated with SimmMechanics. The model of the active needle is designed in Solidworks and then, imported into SimMechanics. SimMechanics is selected as simulation platform for investigating the relationship between actuating signals, applied tissue-needle interaction forces and the needle tip's position and velocity.

5.1 Computer Aided Design of Active Needle

The active needle consists of the main body and the closed-loop mechanism. Articulated links comprise the main body of the active needle. The first link of the main body is manipulated by a stepper motor to insert the needle forward. The closed-loop mechanism (Fig. 6.3) is mounted on the main body of the active needle. This mechanism is a driving system to produce swim-wave motion by transferring motion from rotary motor to revolute joints. Therefore, angles of revolute joints are dependent on each other.

The active needle is modeled in Solidworks (see Fig. 5.1). In this model, the main body of the active needle has three links. The first link has one DOF for translational motion and each of two other links has one DOF for rotational motion. The closed-loop mechanism is also modeled with 6 parallel rectangular bars(see Fig. 3.6). The bars have sliding motion in slots of the main body of the needle.

The closed-loop mechanism is designed to transfer rotary motion to revolute joints. The sliding motion of this mechanism is modeled in Solidworks by setting a constraint for tangential movement of rectangular bars. Then, pins of rectangular bars move parallel to the edge of slots. The active needle is very well modeled in Solidworks. The active needle bends to left/right by moving the rectangular bars back/forward. The conceptual design of the active needle is shown in Fig. 5.1.

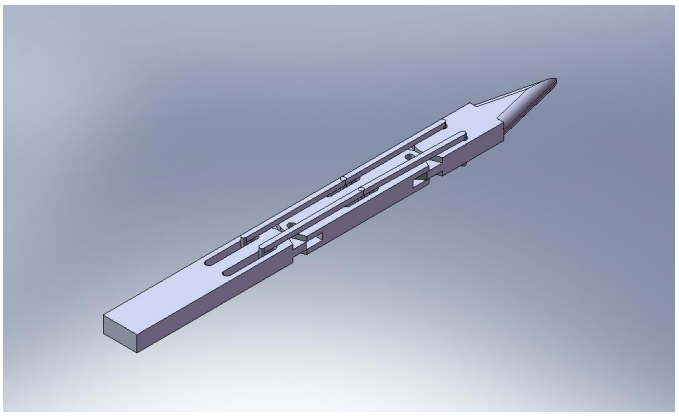

Figure 5.1: CAD design of active needle prototype

5.2 Interfacing Solidworks with SimMechanics

The SimMechanics link utility is the necessary intermediary that enables user to convert CAD assemblies into SimMechanics models. The intermediate step between CAD assembly and SimMechanics model is exporting of an XML file from

the assembly. The exporting process automatically creates STL files containing body geometry information that is required for visualizing bodies of the system. Then, SimMechanics importer converts these files into XML files which is reference to STL files in order to visualize the bodies. The models in SimMechanics with the physical structure can systematically be produced from XML files. The XML file includes mechanical structure, DOF and geometry of body. Simulink and SimMechanics block diagrams are used to model the mechanical system and to provide the platform for simulation.

There is a procedure to transfer Solidworks design into SimMechanics (as described in Fig. 5.2). First, SimMechanics link should be registered in MATLAB. Then, SimMechanics link is added to add-ons of Solidworks. At the end, the completed CAD file should be saved as XML file. This converted file can be opened in SimMechanics platform.

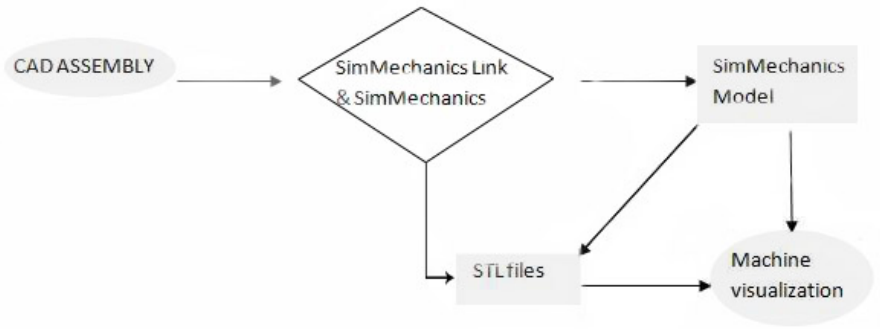

Figure 5.2: Diagram of converting of CAD assembly to SimMechanics model

After exporting the massive CAD model to MATLAB in order to generate the physical model in SimMechanics, some of the constraints between the main body and the closed-loop mechanism in the physical model of SimMechanics are removed. Thus, SimMechanics cannot transfer all constraints from the CAD model. It is required to modify the model and make it compatible with existing dynamic modeling in SimMechanics.

After importing the physical model into SimMechanics and visualizing the model of active needle, actuating signals for the needle joints are determined. The rotation of revolute joints are related to each other due to the kinematics of the closed-loop mechanism. In order to consider constraint motion of revolute joints, actuating signal revolute joints are selected relatively. Three distinct actuating signals are required to run the model, move it forward while producing swim-wave motion.

5.3 Simulation Design Considerations in SimMechanics

SimMechanics is based on the Simscape software which encompasses the modeling and design of systems according to basic physical principles. Simscape software runs within the Simulink environment and interfaces seamlessly with the rest of Simulink and MATLAB. Unlike other Simulink blocks which represent mathematical operations, Simscape blocks represent physical components or relationships directly. Simulink signals can be connected to SimMechanics blocks through actuators and sensors. SimMechanics software is capable of modeling and simulating of mechanical systems with a set of tools to specify bodies, mass properties, possible motions, kinematic constraints, and coordinate systems. Then, motion of the bodies can be initiated and investigated.

After modeling, simulation and visualization of the active needle in SimMechanics, needle-tissue interaction forces are considered. Okamura et al. [73] conducted e research on modeling forces during needle insertion in an *ex vivo* tissue. A translational stage with one DOF was used to manipulate the needle ($1.27mm$ OD, $15.24cm$ long). Their setup performed under computed tomography (CT) fluoroscopy. They measured force component in order to categorize needle insertion

forces. Forces acting on the needle are classified in three groups: stiffness, friction, and cutting. Needle-tissue interaction forces are extracted from current study.

The focus of this study is on Post-puncture needle insertion. Thus, stiffness force which corresponds to pre puncture insertion is not studied. The main sources of frictional force are coloumb friction, tissue adhesion and damping. Frictional force can be measured independently. Cutting force is the combination of needle tip cutting force and tissue stiffness at needle tip due to tissue compression. Cutting force cannot be measured explicitly. Therefore, it is measured by subtracting estimated frictional force from total force. The average cutting force for five-time insertions into a liver is reported to be 0.94 N with insertion velocity of $3mm/sec$ [73]. It should be noted that cutting force consists a major portion of post puncture forces. In our simulation, forces are extracted from experiments done by Okamura et al. [73].

5.4 Simulation Methods

The physical model for simulation comprised three links connected together with three joints. For SimMechanics model, a machine environment block is set to control dynamics of simulation, dimension of machine, gravity, tolerances, mode of analysis, and visualization. The machine environment block should be connected to the ground block. The ground block is the reference block for the body coordinate system of all three links which are directly/indirectly connected to this block. The first link is connected to the ground by a prismatic joint. Revolute joints are used to connect the first link to the second link and the second link to the third link.

Each joint is actuated by an individual actuating signal. The prismatic joint is actuated by a forward motion with the insertion velocity of 3 $\frac{mm}{sec}$. The actuating signal for revolute joints is a sine wave function. Previous works have manipulated

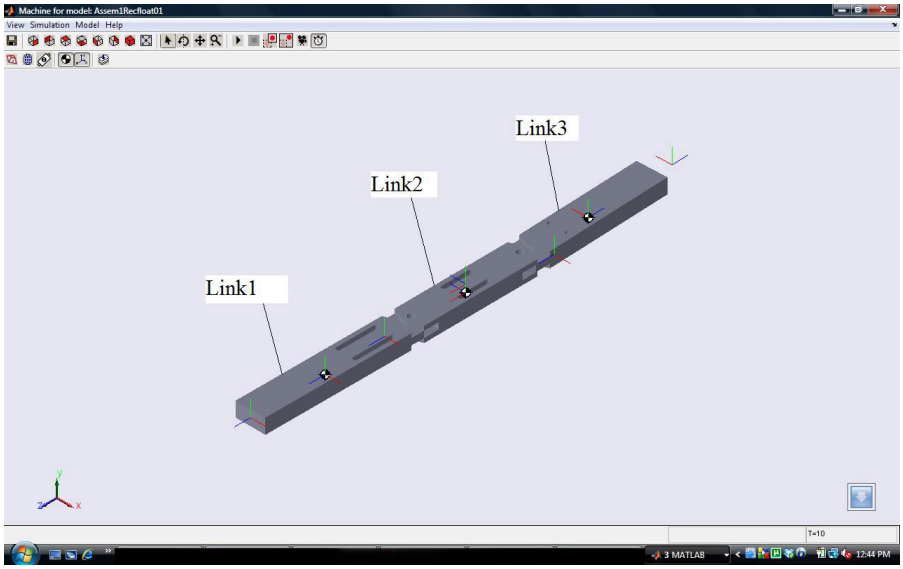

Figure 5.3: Active needle model in SimMechanics software for simulation

the needle with two degrees of freedom (prismatic and revolute) from the first link [85, 96, 97]. In this study, the active needle model is actuated from the base joint with two actuators; One actuator is for forward insertion and another actuator is for swim-wave motion. For swim-wave motion, the rotary motion of the motor is transferred to each revolute joint by the closed-loop mechanism, which is different from existing needle insertion systems.

In simulation, each revolute joint is actuated by a sinusoidal function. for the first joint, the acceleration function is selected to be $-2(\frac{4\pi}{32})^2.sin(\frac{4\pi}{32}t + \frac{\pi}{2})$ and acceleration of the actuating signal for the second revolute joint is $2(\frac{4\pi}{16})^2.sin(\frac{4\pi}{16}t + \frac{\pi}{2})$. Sign of actuating signals addresses the gradient of the path. The actuating signal of each joint is observed by connected sensors (as shown in Fig. 5.7). Fig. 5.4, 5.5 and 5.6 demonstrate position trajectory and velocity of translational and revolute joints after applying actuating signals.

The motion of the needle is constrained by encapsulating tissue around the needle. The surrounding tissue around the needle applies force during needle insertion. Concept of variable mass is used to represent the tissue surrounding the needle.

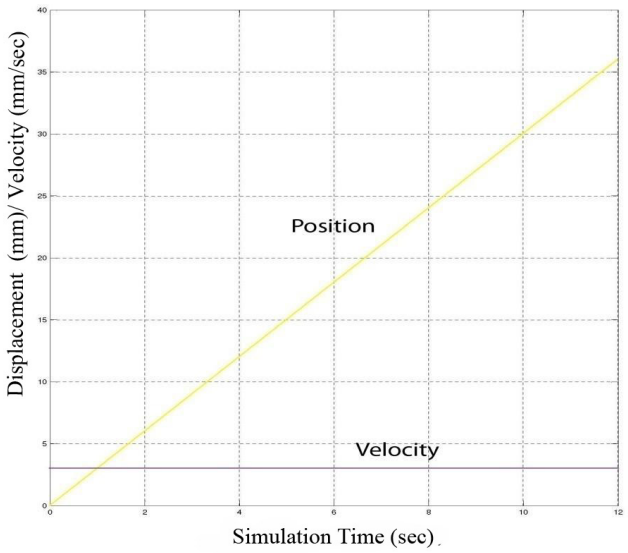

Figure 5.4: Scope of first joint sensor, forward motion displacement and velocity

The variable mass can attach to a body, but cannot actuate the body attached to it. Therefore, thrust forces are applied with respect to the reference body. These trust forces resemble needle-tissue interaction forces. Thrust forces are assigned for each link and their magnitude are extracted from experiments. Fig. 5.7 shows block diagram of the active needle model with needle-tissue interactive forces.

5.5 Simulation Results

Frictional and cutting forces are acquired from research conducted by Okamura et.al [73] on rigid needle insertion into the liver tissue. The active needle consists of rigid articulated parts. Each link of the active needle model is considered as a rigid needle. Thus, frictional and cutting forces are applied for each link of our active needle.

Cutting force is the dominant force applying on the needle. The average value

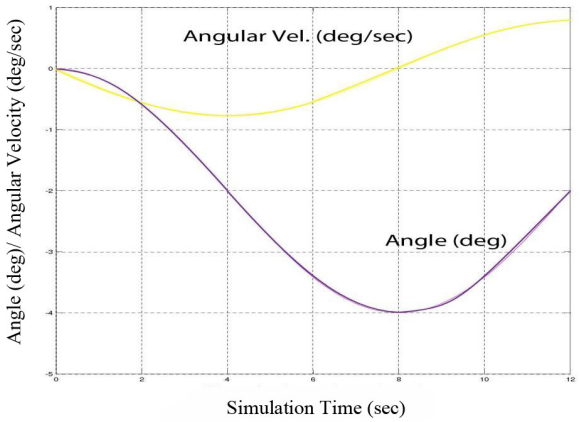

Figure 5.5: Scope of second joint sensor, angle of rotation and angular velocity

of cutting force is 0.94 N. Frictional force repeats itself for sinusoidal insertion motion used in this experiment. In order to apply frictional force on links of our simulated model, the actuating signal is extracted from the experiment. Thus, the actuation signal is a discrete time function. The extracted vector of frictional forces is $[0.5, 0, -1, -1.5, -1, 0.4]$ for a duration of 6 sec. This vector is a step function with $1sec$ duration for each step.

The following four assumptions are considered to simulate needle-tissue interaction:

1) Cutting force on the needle tip: Cutting force is the only force which is considered in this category, because cutting force is the major portion of the total force required for the insertion.

2) Frictional force on the first link, cutting force on the second and the third links: Cutting force on the last two links is 0.94 N for each link. Frictional force is applied by the step function described above.

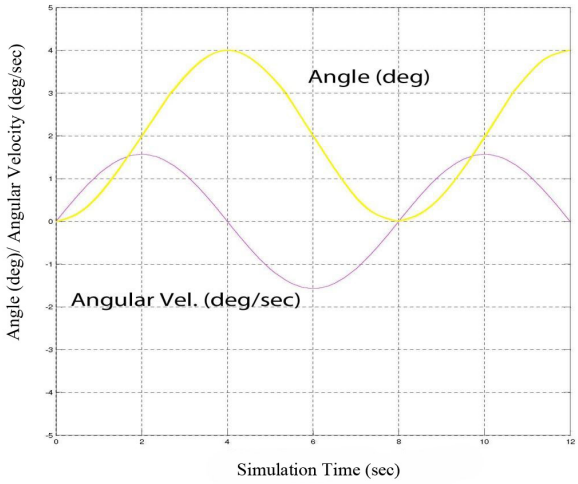

Figure 5.6: Scope of third joint sensor, angle of rotation and angular velocity

3) Cutting force and frictional force on all three links: frictional force is applied on moving forward link as well as rotating links. In this case, all three links can cut the tissue and the cutting force is applied on each link.

4) Frictional force on all three links and cutting force on the needle tip: It is assumed that the last link with a sharp end has the most effective cutting force and other links follow the path of the needle tip. Therefore, cutting force is only applied on the last link. In addition, frictional force is applied to all three links.

The last link is connected to a sensor to record the motion of the needle tip after exerting forces on the needle. For every one of the four assumptions illustrated above, position trajectory of last link is demonstrated (Fig. 5.8 and 5.9). The first joint of this simulation is a prismatic joint with only one DOF. The prismatic joint constrains the motion and cannot demonstrate the effect of external forces. Another type of joint with more than one DOF is required to observe the effect of forces.

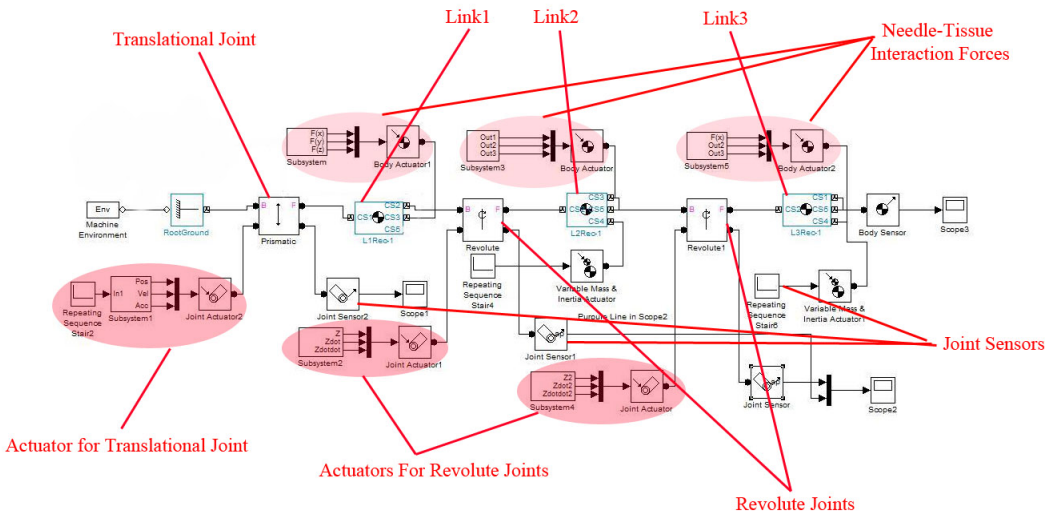

Figure 5.7: SimMechanics block diagram of active needle with modeling needle-tissue interaction forces

A cylindrical joint replaced the prismatic joint. The cylindrical joint permits needle shaft to rotate and move forward as well. Based on the four described assumptions, simulations are repeated by using the cylindrical joint. In Fig. 5.10, displacement of the needle tip is presented. It seems that there should be no displacement in the normal to the plane of motion. Misalignment between origin of the ground block and origin of the local coordinate system causes error displacement which is shown by purple line (Fig. 5.10, 5.12, 5.14 and 5.16); this error is appeared due to the usage of a cylindrical joint. The needle's forward insertion motion is demonstrated for all four assumptions in Fig. 5.13, 5.13, 5.15 and 5.17.

Simulation results of needle insertion while using a prismatic joint, is considered to be reference for the validation of needle insertion using cylindrical joint. If there is no noise in needle steering, the needle tip displacement vs. the normal direction to the forward insertion motion should have the same trend as Fig. 5.8. This figure demonstrates the trend of needle deflection in the plane of motion. Simulation results of other cases which follow this trend are considered acceptable, although

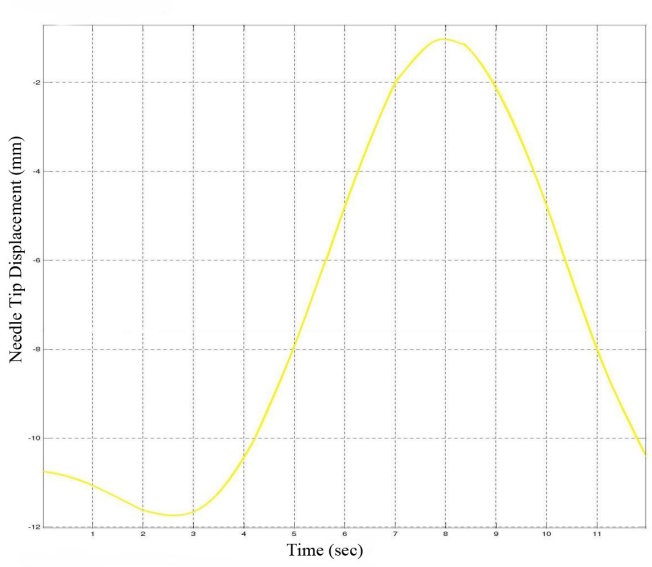

Figure 5.8: Displacement of needle tip vs. normal direction to forward motion of needle, dimensions in mm

all cases are very noisy. In Fig. 5.14, case III demonstrates an opposite trend of deflection comparing to the other three cases. Furthermore, deflection of needle in direction normal to the plain of motion should be as small as possible. The purple line in case II is very noisy (as shown in Fig. 5.12). Therefore, case II and case III have unreasonable results by comparing them to the case of prismatic joint. Case I and case IV have acceptable simulation results. Fig. 5.10 and 5.16 reach their maximum value at $t = 8sec$ and minimum value at $t = 2sec$. It is noticeable that the curvature of these two figures changes after $t = 5sec$. It should be considered that case IV is more comprehensive than case I by considering frictional forces applying on the active needle. The frictional forces have no effect on forward motion displacement of needle for all cases (Fig. 5.11, 5.13, 5.15 and 5.17).

In this chapter, a computer simulation method is proposed using Solidworks to model an active needle and SimMechanics to simulate its interaction with the soft tissue. The simulation results could be experimentally validated. The proposed simulation-based design methodology could be used in the development of other

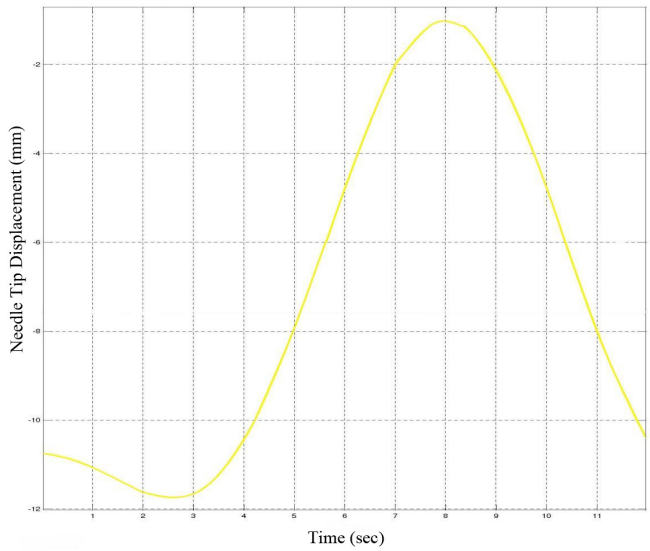

Figure 5.9: Displacement of needle tip vs. direction of needle forward motion, dimensions in mm

medical devices.

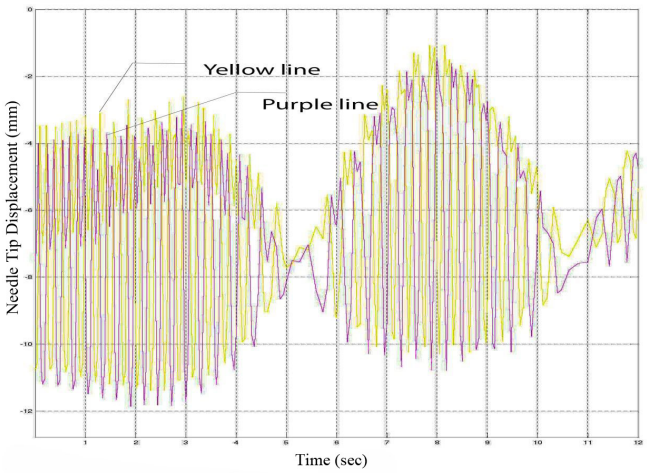

Figure 5.10: Case I, needle tip displacement vs. time

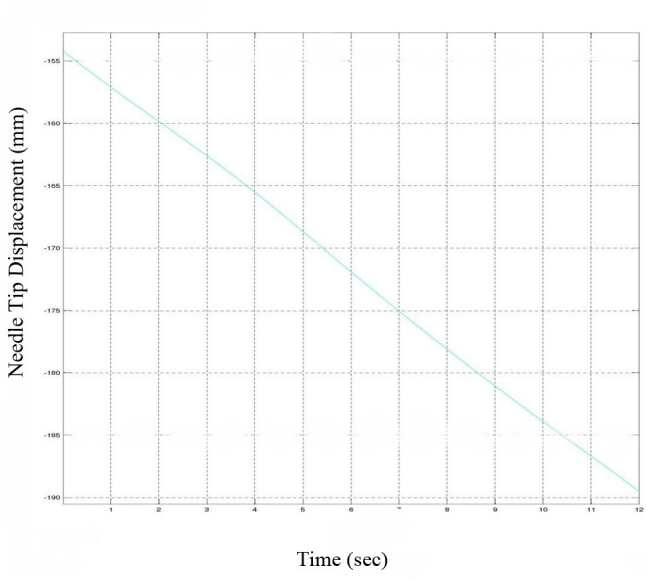

Figure 5.11: Case I, needle tip displacement vs. time, displacement along forward motion direction, dimensions inmm

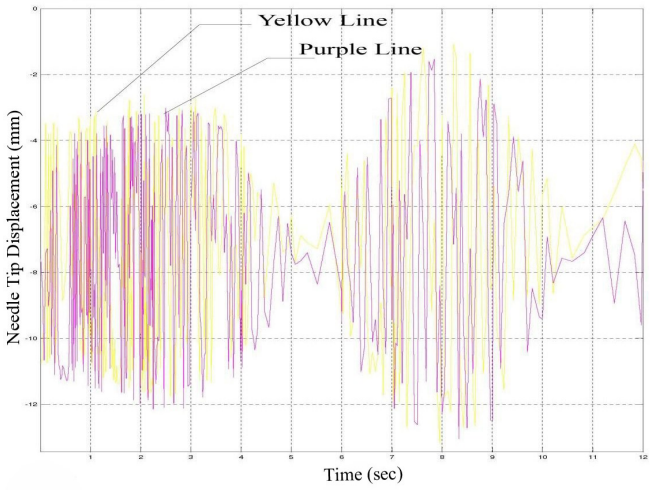

Figure 5.12: Case II, needle tip displacement vs. time

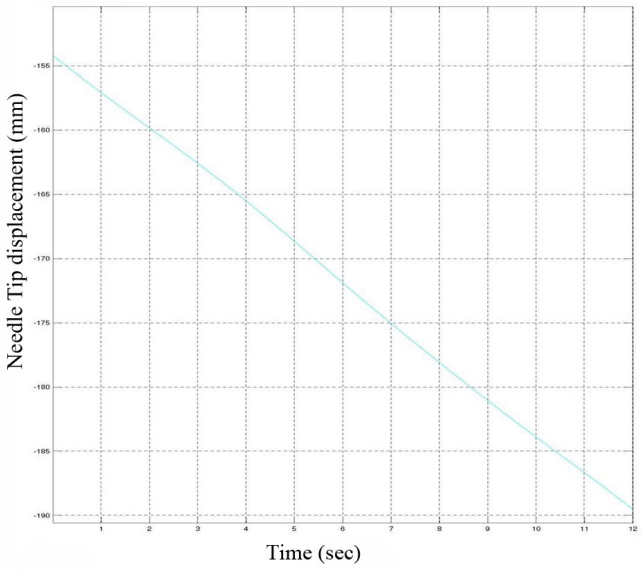

Figure 5.13: Case II, needle tip displacement vs. time, displacement along forward motion

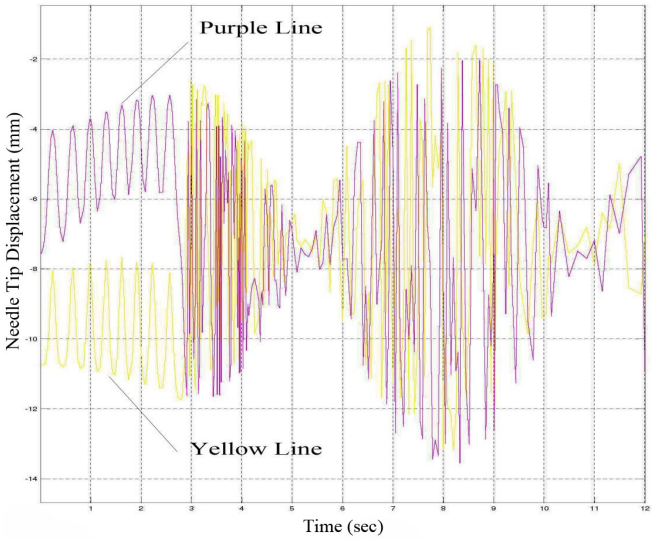

Figure 5.14: Case III, needle tip displacement vs. time

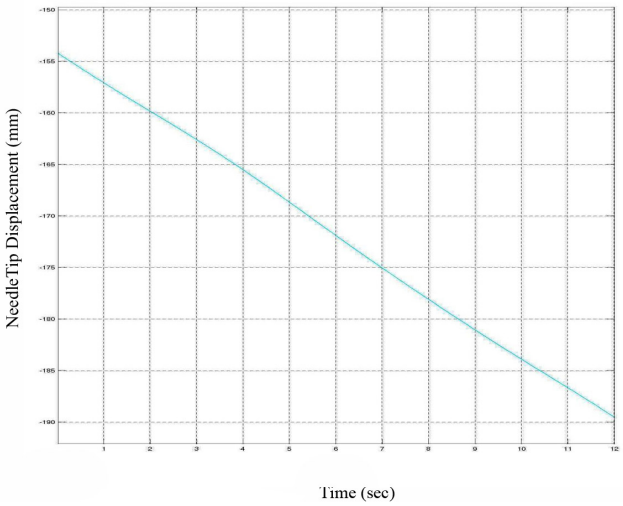

Figure 5.15: Case III, needle tip displacement vs. time, direction along forward motion

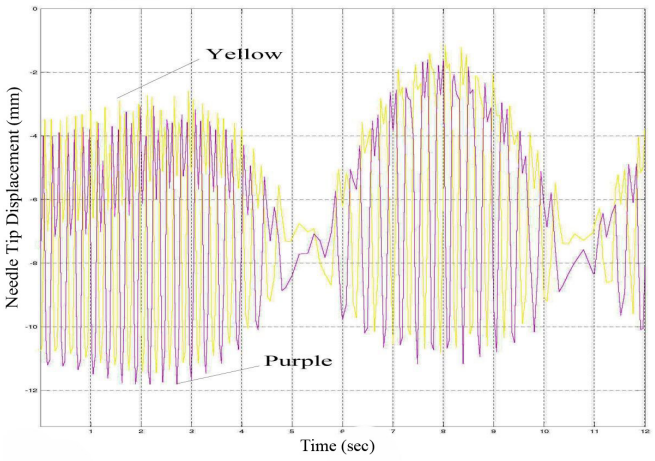

Figure 5.16: Case IV, needle tip displacement vs. time

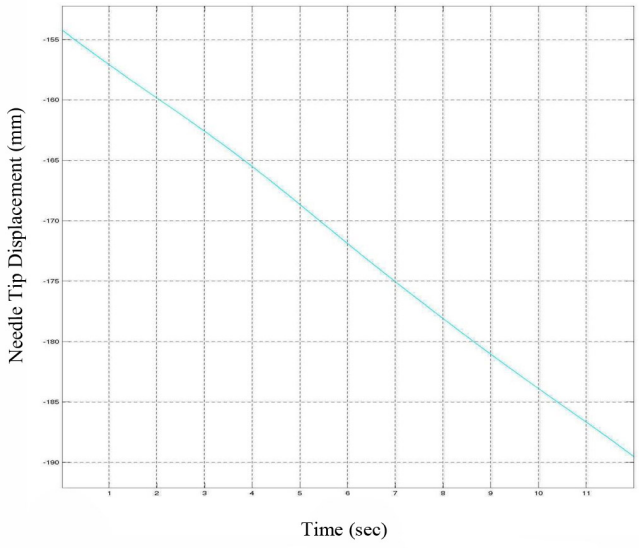

Figure 5.17: Case IV, needle tip displacement vs. time, displacement along forward motion

Chapter 6

Experiment of an Active Needle Prototype

This chapter explains implementation and fabrication of the active needle prototype. The prototype represents a surgical needle which is larger than a real surgical needle. The experiment is conducted to investigate the accuracy of needle insertion and to determine the flexibility of the active needle model.

6.1 Active Needle Prototype Development

The active needle prototype consists of two main parts: the main body and the closed-loop mechanism. In our active needle prototype, the main body has three links connected together with revolute joints. The concept of the active needle is presented through this prototype. The size of the active needle is about five times larger than real surgical needle. However, micro fabrication is a technique that can be used in future studies to reduce the size of the needle. The prototype consists of the main needle mechanism, the closed-loop mechanism, the actuating mechanism, and the computer interface (see Fig. 6.1).

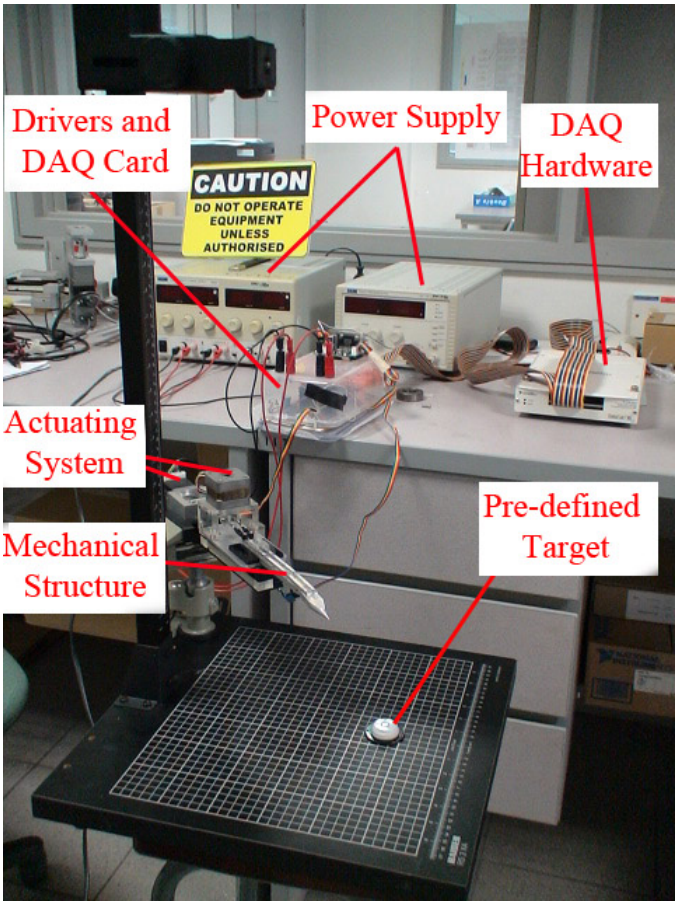

Figure 6.1: Active needle insertion system

6.1.1 Mechanical Structure

The active needle prototype composed of two mechanical structure: the main needle structure, the closed-loop mechanism. Appendix A includes drawing of the main body and the closed-loop mechanism.

Main Needle Structure:

The main body has three links connected together with revolute joints. Total length of three links is 20 cm. The needle has a rectangular cross-section ($7cm \times 15cm$). The needle is made of aluminium with a density of $2.7\frac{kg}{mm^3}$ and Young's modulus(E) of 70000 Mpa. Link 1 of the main body is connected to a translational stage which inserts the needle forward Fig. 6.2. All three links are

connected together with revolute joints and positioned at the same level at connecting junction. Thus, the thickness of link 2 is designed to be smaller at both ends in order to fit inside the rectangular saw tooth shapes of the mating end of link 1 and link 2 , and also link 2 and link 3.

The slots are grooved inside link 2 and link 3 with a reasonable distance far apart. This distance is the moment arm to transfer reciprocating motion of the bars into rotational motion of the joints. The reciprocating motion permits the last joint to have a larger angular displacement than the other revolute joint. The moment arm, which is the horizontal distance between center of revolute joint and center line of slot, is designed to be $4mm$. The width of the main body is constrained by this length because smaller moment arm is not able to produce required angular displacement. If geometrical configuration does not constrain the motion, a more powerful motor can produce a larger angular displacement with a smaller moment arm. There is a trade-off between a more powerful motor and smaller width for the main body. The suggested value is selected for our design regarding the power of the actuator.

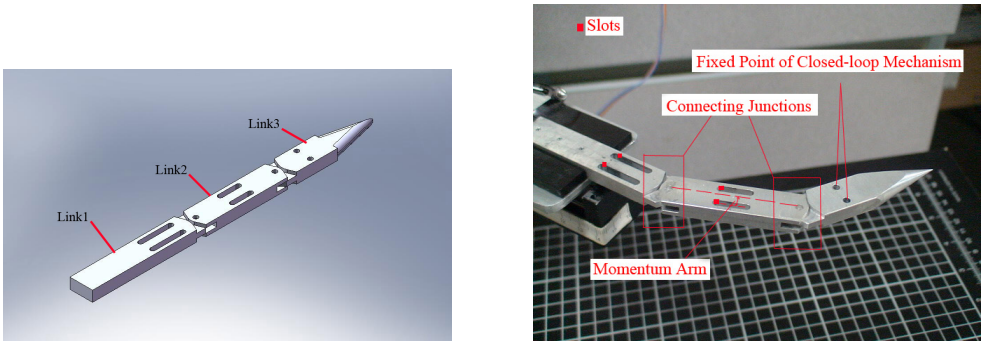

(a) CAD diagram of main body (b) Physical model of main body

Figure 6.2: Main body: physical and CAD model

Closed-loop Mechanism:

The closed-loop mechanism is consisted of three pairs of parallel bars which transfer the rotational motion of the motor to the main body. These bars are

positioned parallel to each other to produce push and pull motion. Push and pull motion is transferred to swim-wave motion of the needle. The advantage of this mechanism is that actuator is placed at the base joint of the needle. Therefore, the actuator for swim-wave motion is positioned out of the workspace of the needle and the size of the needle is not constrained by the required actuators.

This mechanism is connected to the main body with pins to slide inside slots of the main body. The slots in link 1 and link 2 permit the mechanism to slide in with respect to fixed points (shown in Fig.6.2). The fixed points of this mechanism are at connecting points between the last pair of links of the closed-loop mechanism and link 3 of the main body (shown in Fig.6.2).

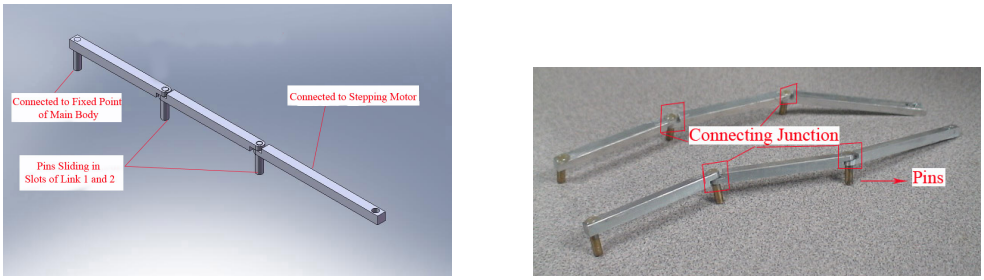

(a) CAD diagram of closed-loop mechanism

(b) Physical model of closed-loop mechanism

Figure 6.3: Closed-loop mechanism: physical and CAD model

Connecting junction of bars of this mechanism is designed to be at the same level when mating surfaces of links come together (Fig. 6.3). The end of bars at mating junction with the next bar has step configurations.

6.1.2 Actuating System

Actuators used for the active needle are stepper motor units. Stepper motors are enough stable to drive a wide range of loads. This type of motor requires no feedback which suits our desire for the active needle insertion open-loop system. They can drive load without a gear system. Therefore, the system is compact by

having minimum components. One stepper motor for forward motion, and another stepper motor for swim-wave motion. The latter motor is mounted on translation stage connected to the stepper motor for the forward motion as shown in Fig. 6.4.

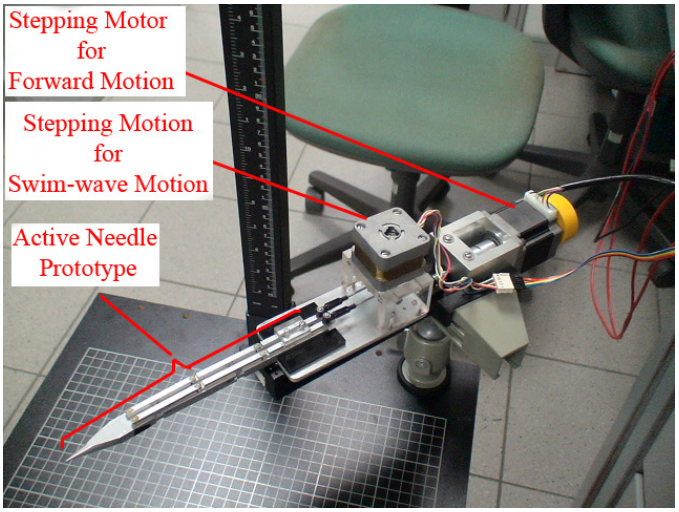

Figure 6.4: Actuating system for active needle prototype

Stepper motor for forward motion:

For the active needle insertion, steeping motor PK265 has been used with driver CMD2120P. The 1.8° stepper motor specification is shown in Table 6.1.

Table 6.1: Stepper motor unit PK256

Motor Type	Possible Thrust	Driver Model	Power supply input voltage	Power supply current capacity
standard type(PK256)	0.53N	CMD2120P	24 VDC	2.9 A or more

This 2-phase stepper motor and its driver are shown in Fig. 6.6. The driver sends signals to move the motor with definite steps.

Stepper motor for swim-wave motion:

Stepper motor 103-540-26 STEP-SYN with a resolution of 1.8° is selected (Table 6.3). A circular disk is mounted on the shaft of the motor. On this disk, two holes are drilled which are $8mm$ far apart. Two rods are placed inside these holes

(a) 2 phase-stepper motor PK256

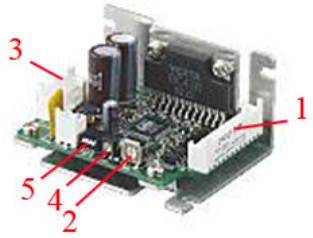

(b) Driver, 1.I/O signals connector 2.motor operating current setting switch 3.motor connector 4.motor stand still current potentiometer 5.Pulse input mode setting switch

Figure 6.5: Stepper motor and driver for forward motion

from one end. They are connected to the first link of the closed-loop mechanism from the other end (shown in Fig. 6.8).

Table 6.2: Stepper motor unit 103-540-26 STEP-SYN

	Type	Power Supply input voltage	Power supply current capacity
stepper motor	103-540-26 STEP-SYN	4 VDC	0.6 A
Control circuit	L297 and L298N	5 VDC	0.7 A

The driver control circuit is required to provide driving signals to the power stage. L297 controller is used to control stepper motor. Used with a dual bridge driver such as the L298N forms a complete microprocessor-to-bipolar stepper motor interface. The L297 with the driver combination has many advantages: very few components are required (so assembly costs are low, reliability high and little space required), software development is simplified and the burden on the micro is reduced. Furthermore, the choice of a two-chip approach gives a high degree of flexibility. The L298N can be used on its own for DC motors and the L297 can be used with any power stage, including discrete power devices.

This stepper motor is a bipolar motor and is driven by an L297, an L298N bridge driver and very few external components. Together these two chips form a complete microprocessor-to-stepper motor interface.

(a) Stepper motor 103-540-26 STEP-SYN

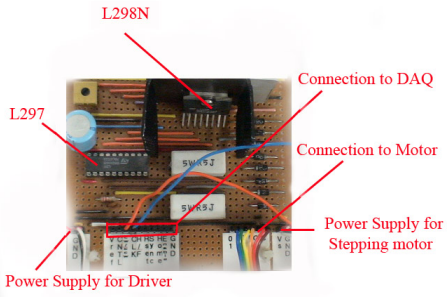

(b) Stepper motor control circuit

Figure 6.6: Stepper motor and driver for swim wave motion

6.1.3 DAQ Programming for Driving Motors

LabView is a graphical programming language (G-language) and it uses the concept of Virtual Instruments (VIs), which is distinct from other text-based programming languages and the intuitive graphical development environment combines the ease of using configuration-based tools with the flexibility of a powerful programming language.

LabView's programming environment consists of two main windows: the Front Panel (FP) and the Block Diagram (BD). The FP provides users interfaces to the program where the inputs and outputs to the program are indicated by various animation items like knobs, push buttons or LEDS. The BD is where the graphical code is written with all the wires representing the flow of data among function blocks. All of the control programs are developed in LabView 7.1 from National Instruments.

In programming with LabView, DAQmx functions should be used sequentially for a task. The DAQmx-Create Channel.vi is the first function which needs to be called for configuration/selection of the ports to be used in the task. Next, either the DAQmx-Timing.vi or the DAQmx-Trigger.vi can be called to configure the properties of the task. After that, the DAQmx-Start Task.vi is called to explicitly start the task. At this point, the DAQmx-Write.vi or DAQmx-Read.vi is called

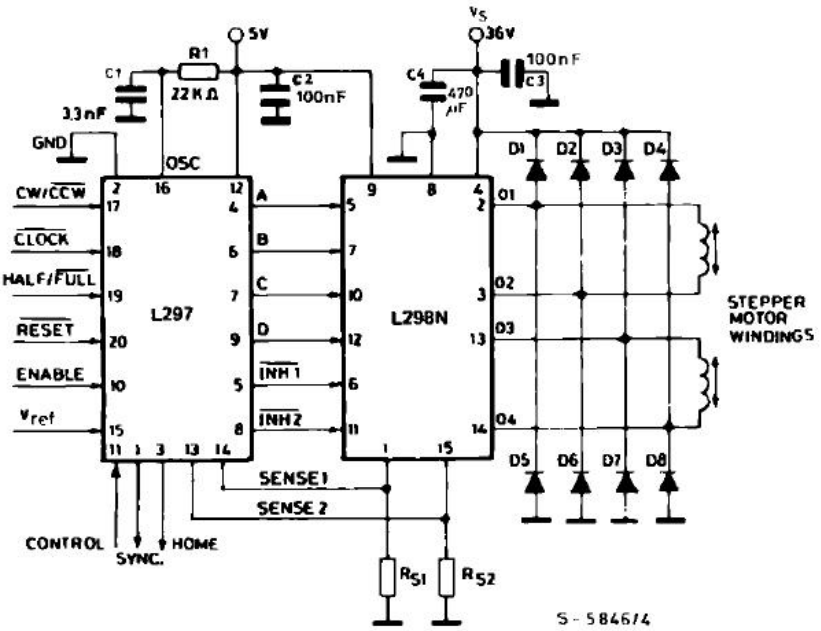

Figure 6.7: L297 and L298N driving a bipolar stepper motor

to write or read the lines. Lastly, the DAQmx-Clear Task.vi is used to clear the reserved ports for other functions to be used at the end of the task.

LabView program controls the motion of these two stepper motors. In order to calculate the number of steps, first, current position of the needle is assumed to be saved into variables. Then, next position for the motor is read from input values and subtracted from current position. By knowing the sign of subtraction, direction of rotation can be determined and array for values of position difference are built to be written out in order to produce output signals. Then, the motor will rotate to reach next position, clockwise or counter clockwise following the sign of subtraction.

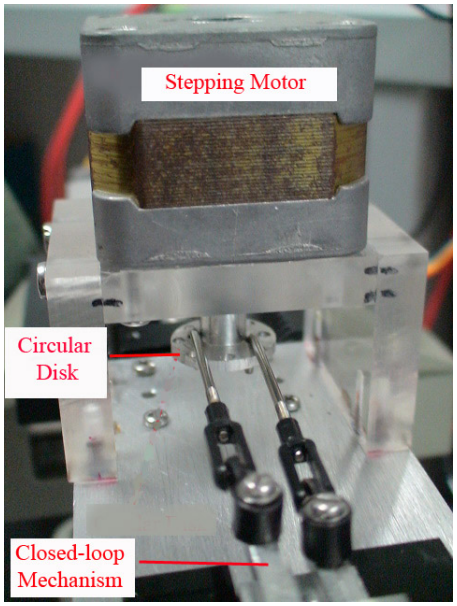

Figure 6.8: Circular disk connected to closed-loop mechanism

6.2 Experiment Methodology and Results

The experiment is set up to observe the performance of flexibility and accuracy of the active needle. In LabView programming, the actuating signal is used in definite number of units. Based on the resolution of stepper motors, number of units are calculated.

The empirical measurements show that each unit in LabView program equals to 2.1° angular displacement of stepper motor. The experiment is conducted to investigate the flexibility of the active needle to reach the pre-defined target. The predefined target is marked in the xy plane of motion. The main idea is to break insertion procedure into two stages. First, a line parallel to the centerline of the main body (initial position of stretched out links) is drown. Next, number of units required for swim-wave motion to touch this line are calculated. After that, a forward motion with known resolution of translational stage can navigate the needle to the target.

This is the pre-planning strategy for the active needle experiment. In experiment, needle forward motion and swim-wave motion are performed at the same time. It is calculated that swim-wave motion and needle insertion are to complete during the same period of time.

6.2.1 Swim-Wave Motion Experiment

First, swim-wave motion is investigated by monitoring the position of needle tip for a number of iterations to determine the accuracy of this motion. The position of the needle is recorded to determine the required number of units to bend the needle to the right or left side. The initial position is measured as shown in Fig. 6.9 and then, fifty number of steps are selected as the input for the stepper motor. The final position of the needle is also recorded. The displacement vector is defined by the mean value for twelve iterations.

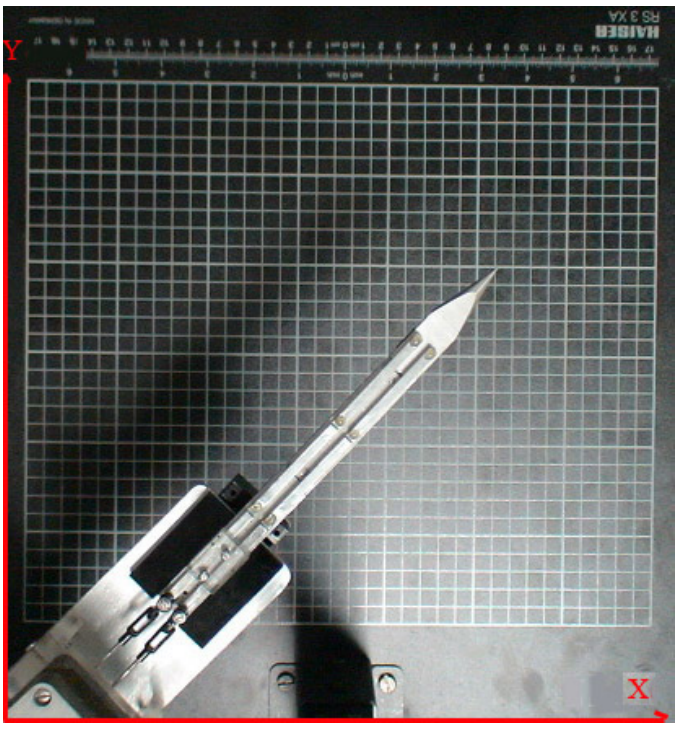

Figure 6.9: Initial position of needle tip before swim-wave motion

Fifty number of steps are required to make the needle to bend to left or right side (Fig. 6.10 and Fig. 6.11). For twelve iterations, data are recorded to determine displacement vector for counter-clockwise or clockwise rotation of the stepper motor.

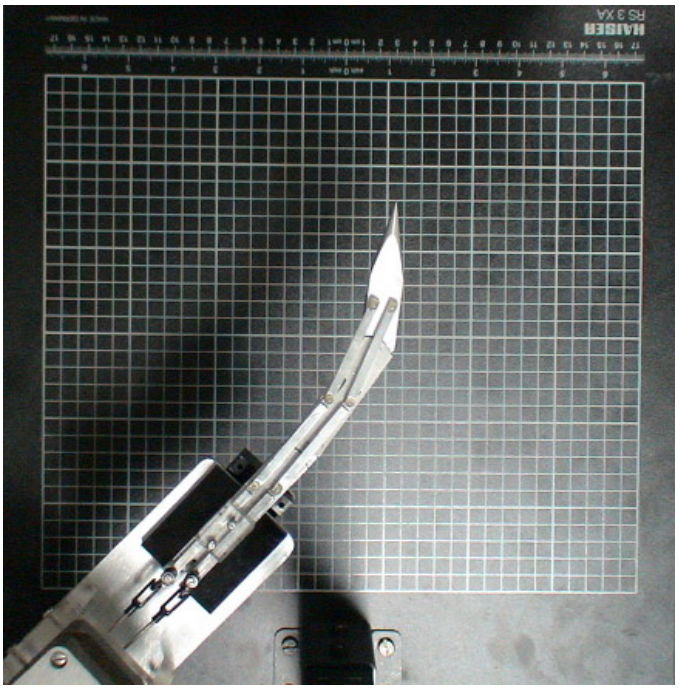

Figure 6.10: swim-wave motion under positive rotation of stepper motor

6.2.2 Active Needle Prototype Experiment

Two pre-defined targets are determined in the workspace area of the active needle. The experimental methodology determines the required steps for swim-wave motion and forward motion. For theses defined targets, the active needle is pre-planned to reach the target and then retract to insert another time. For each target, the needle is inserted twelve times to find out the accuracy of needle insertion.

The first predefined target is positioned at distance $2mm$ at angle 143° with respect to the x axis of the world coordinate system (shown in Fig. 6.9). In order

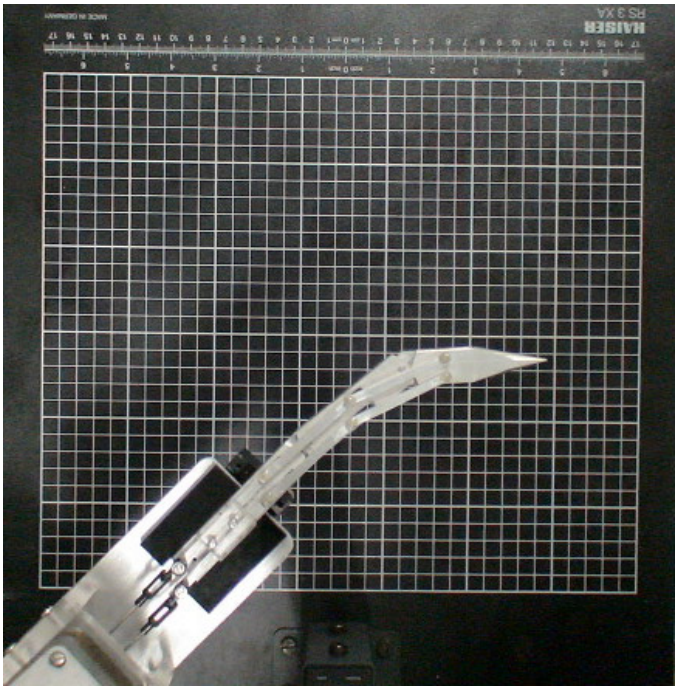

Figure 6.11: Swim-wave motion under clockwise rotation of stepper motor

to reach this target, counter-clockwise rotation of the stepper motor is required for the active needle. Number of steps are calculated to be 40 steps (counter-clockwise rotation) for swim-wave motion and 5000 steps for forward motion (presented in Fig. 6.12). Then, the active needle is navigated to the target and deviation is calculated for each insertion. For twelve times insertions, the needle tip's position is recorded and the distance from the target is calculated. Fig. 6.13 shows the predefined target and the active needle's posture to achieve the target for one insertion trial.

The second predefined target is positioned at distance $1.7mm$ and at angle $49°$ with respect to the x axis of the world coordinate system (demonstrated in Fig. 6.9). In order to reach this target, number of steps for forward motion are 5000 steps for forward motion and 40 steps (clockwise rotation) for swim-wave motion. In this case, the accuracy of needle insertion is calculated for twelve insertion trials. The needle's posture is presented after one insertion trial to reach predefined target

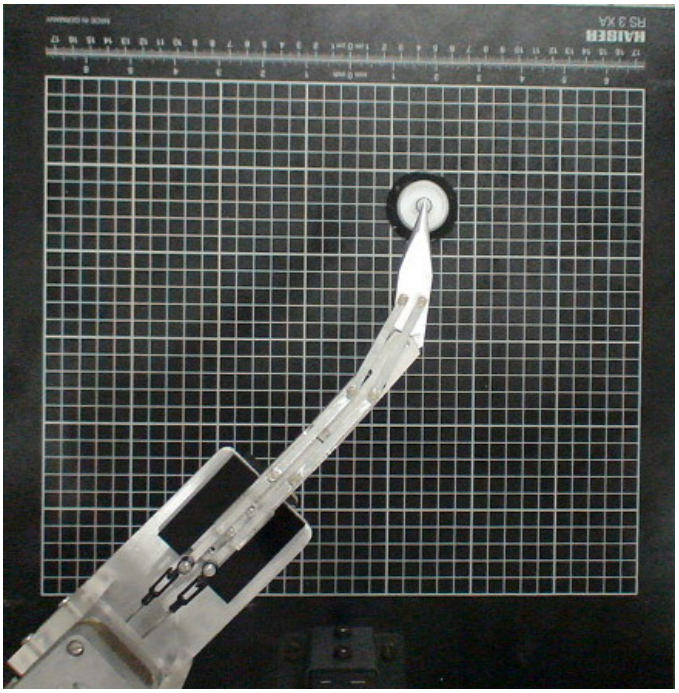

Figure 6.12: Experiment of simultaneous movement to reach pre-defined target, CCW rotation for swim-wave motion

as shown in Fig. 6.14.

6.2.3 Experiment Results

In these two experiments, the needle tip's position is recorded before and after insertion. The main objective of experiments is to determine the accuracy of needle insertion for each experiment. In the first experiment, the required number of steps for stepper motor is calculated to reach a predefined target. Preplanning needle insertion for the second experiment is based on the first experiment. In the second experiment, main objective is to find out the accuracy of needle insertion for two predefined targets.

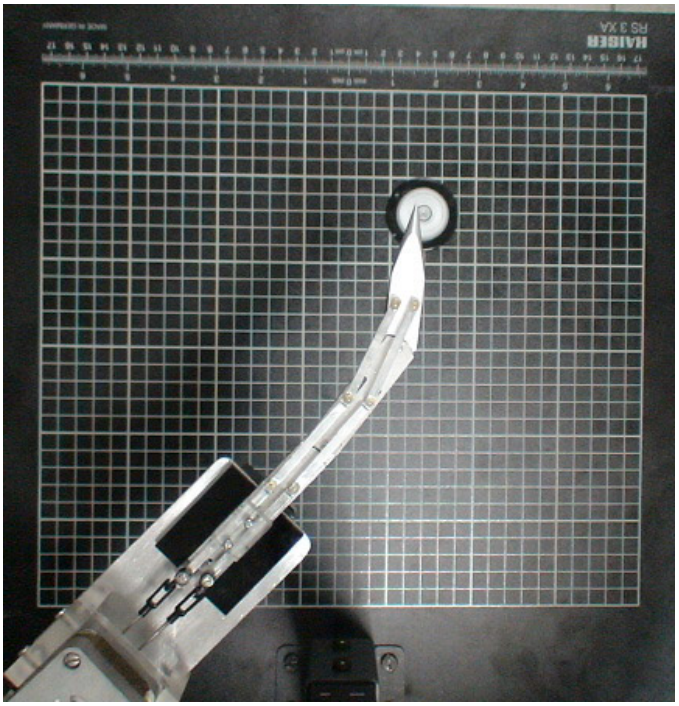

Figure 6.13: Needle tip position, deviation from predefined target on left-side of the needle

6.2.3.1 Results of Swim-Wave Motion Experiment

The result shows that the displacement vector, for counter-clockwise rotation of the stepper motor for fifty steps, is the vector with magnitude of $2.9mm$ at angle of $63°$ with the x axis of the world coordinate system (shown in Fig. 6.9). For counter-clockwise rotation of the stepper motor, the vector has the magnitude of $2.4mm$ at angle of $171°$.

6.2.3.2 Results of Active Needle Prototype Experiment

The first predefined target is positioned at angle $143°$ with respect to the x axis of the world coordinate system (shown in Fig. 6.9) with $2mm$ distance. Based on results of the first experiment of swim-wave motion, the required number of steps for both stepper motors are calculated. For twelve insertions, the needle tip's

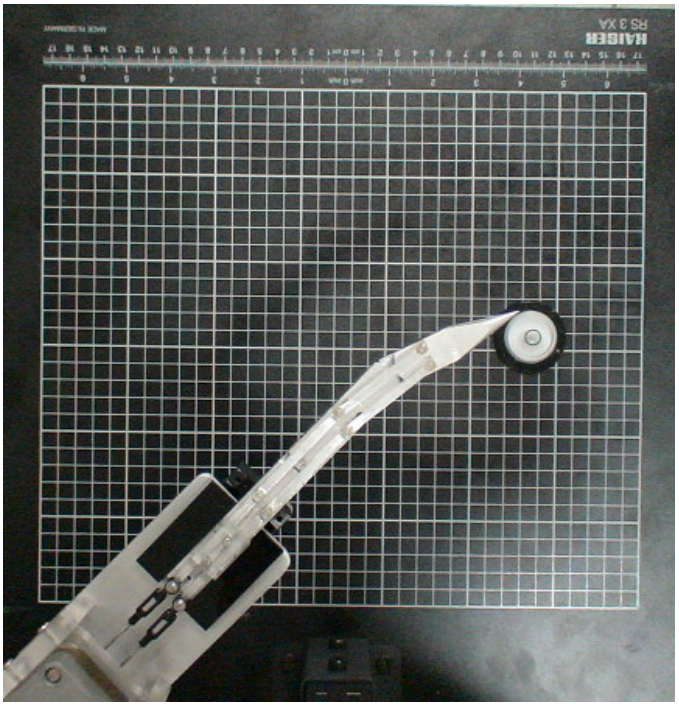

Figure 6.14: Needle tip position, deviation from predefined target on right-side of the needle

position is recorded and its distance to the target is determined. The average error for placing the needle tip is found to be $4.9mm$ for the first predefined target. The needle tip's position is shown for all insertions in Fig 6.15.

In the second experiment, the target is positioned at angle 143° with respect to the x axis of world coordinate system (shown in Fig. 6.9) with $2mm$ distance. The average error for needle tip placement at predefined target position for twelve insertions is calculated to be $1.8mm$. Fig. 6.16 presents the needle tip position for all twelve insertions.

Table 6.3: XY displacement of needle tip under actuation of stepper motor, dimensions in cm

(a) Counter-clockwise rotation

X	Y
14.6	7.1
12.4	5.9
14.5	7.1
12.4	5.9
14.5	7.1
12.3	5.9
14.4	7.1
12.5	5.9
14.6	7.2
12.5	6
14.7	7.1
12.4	5.9
14.6	7.2
12.5	6
14.7	7.1
12.5	5.9
14.5	7.1
12.4	6
14.5	7.1
12.4	5.8
14.5	7.2
12.5	6
14.6	7.1
12.4	6

(b) Clockwise rotation

X	Y
14.6	15.9
7.1	9.5
14.9	15.9
7.1	9.7
14.7	15.9
7.2	9.6
14.6	15.9
7.1	9.8
14.6	16
7.2	9.8
14.6	15.9
7.1	9.7
14.7	16
7.2	9.8
14.8	15.9
7.3	9.8
14.7	15.9
7.2	9.8
14.5	15.9
7.0	9.6
14.6	15.9
7.1	9.8
14.6	15.9
7.2	9.5

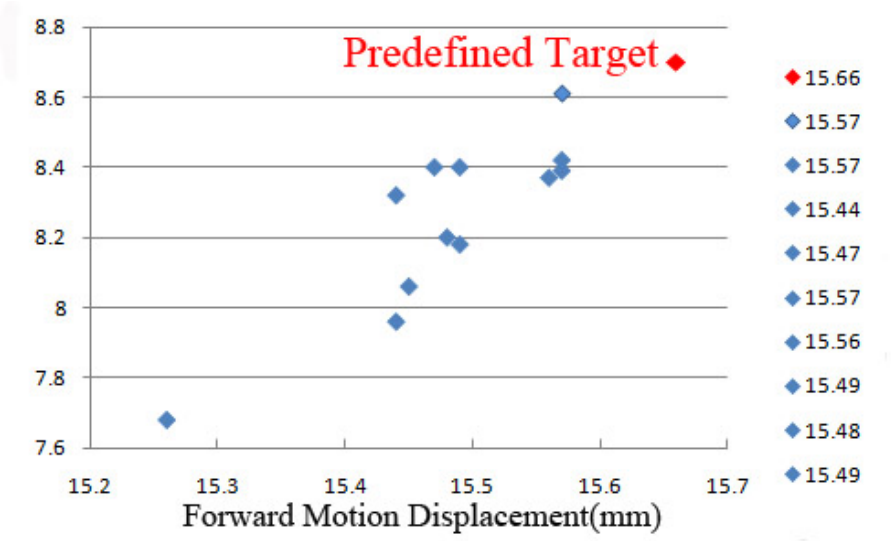

Figure 6.15: Needle tip position in xy plane for counter-clockwise swim wave motion

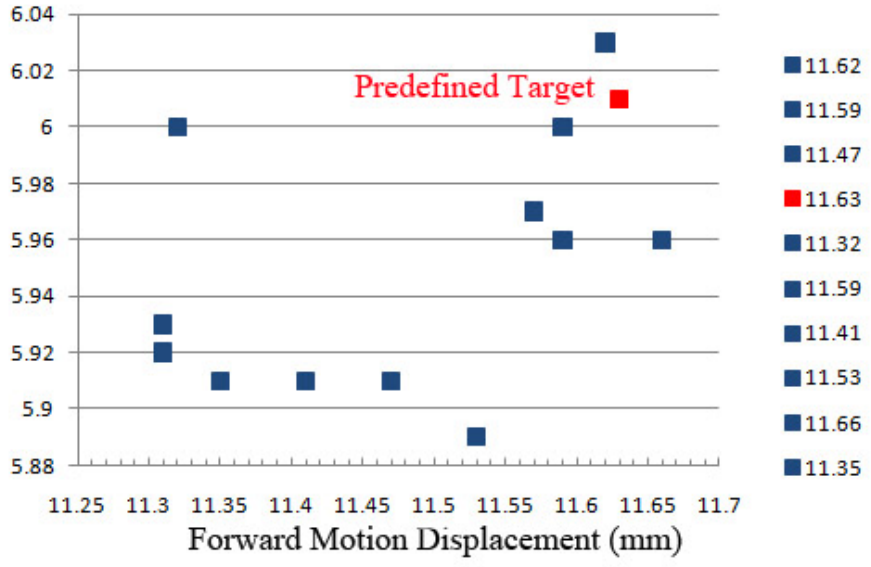

Figure 6.16: Needle tip position in xy plane for clockwise swim wave motion

Chapter 7

Discussion and Conclusion

The research issues of the active robotic needle including kinematic analysis, dynamic analysis, path planning, and simulation of the tissue-device interaction are investigated in this thesis. The active needle prototype device has also been fabricated. The performance of this prototype is examined by experiments. This chapter describes the limitations and contributions of our research on flexible needle insertion. Further improvement on the active needle has also been discussed.

7.1 Discussion

The findings and limitations of this research are discussed in four subsections.

7.1.1 Kinematic and Dynamic Analysis

A robotic device is proposed to enhance the reachability of the active needle by adding revolute joints to a long needle. These revolute joints create swim-wave motion of the active needle. A forward motion is also employed at the same time.

Simultaneous effect of forward motion and swim-wave motion increases reachable areas for the active needle. Swim-wave motion is created by the closed-loop mechanism to transfer rotary motion of the motor to the revolute joints. The actuator for swim-wave motion can be positioned at the base joint of the needle. This can reduce the size of the active needle model. Without micro-machining fabrication infrastructure, the mechanical structure limits size reduction of the active needle because a minimum length for moment arm is required. The moment arm exerts momentum on revolute joints under the application of reciprocating motion of the closed-loop mechanism.

The closed-loop mechanism used for the active needle insertion constrains the rotation of angles and applies constraint on the range of swim-wave motion and joint's revolution. The dependency of revolute joints on each other restricts the range of swim-wave motion. Kinematic analysis of the closed-loop mechanism may provide a detailed analysis of the active needle model.

7.1.2 Path Planning and Simulation of Tissue-Needle Interaction Using SimMechanics

The active needle is modeled as a linear cantilever beam which is under the application of the bending energy from the surrounding tissue. The main objective is to reduce the transferred energy required to bend the needle. Tissue injury and recovery time can be reduced if the bending energy is minimized for an optimal path. An optimal path is found regarding to needle-tissue interaction forces, while there is no obstacle in the examination area. The optimal path is started from an insertion point and reaches a target, which is aligned with the insertion point.

The optimal path is determined with the maximum amplitude of $0.1mm$. This path cannot be followed by the prototype of the active needle and can not be

achieved by simulation analysis. Then, the simulation is used to investigate a path of the active needle model.

The active needle is designed in CAD software with the mechanical structure in details. Then, the CAD model in Solidworks is transformed to the SimMechanics software for the simulation. The revolute joints are actuated to create swim-wave motion of the active needle, along with a forward motion. In simulation, frequency of two revolute joints are selected relatively considering the kinematics of the closed-loop mechanism. The simulation result has a high amplitude compare to the optimal path of the path planning.

Two different types of joints are used for the translational stage in order to insert the needle forward: prismatic joint and cylindrical joint. Prismatic joint has only 1-DOF which is not affected by the amount of applied forces. In order to observe the effect of needle-interaction forces, the cylindrical joint is selected which has 2-DOF, one forward motion and another revolute motion about insertion axis. Based on the four different assumptions, different simulations are conducted. The simulation results are good when the cutting force is exerted at the needle tip separately or together with the frictional force applied on the last link.

The two aforementioned assumptions have reasonable results which match with the trend of the simulation result of the prismatic joint. Therefore, it is concluded that the cutting forces can be applied on the needle tip of the active needle as well as frictional forces only on the last link. These results are verified by other's method used for motion planning described in Chapter 3. One method was the application of the cutting force on the last link [94] and the other was the ignorance of frictional forces as a constraint of motion [95].

7.1.3 Experiment

Experiment is conducted to determine the accuracy of needle insertion. The prototype of the active needle is fabricated and then, motorized by two stepper motors. Based on the preliminary simulation, the required number of steps are calculated for the stepper motors of both motions: forward motion and swim-wave motion. The relation between swim-wave motion and the needle tip's position is investigated. After that, the accuracy of needle insertion for two pre-defined targets is calculated. Two pre-defined targets are reached by the combination of forward motion and swim wave motion of the needle. Fig.7.1 and 7.2 show the error for each insertion trial.

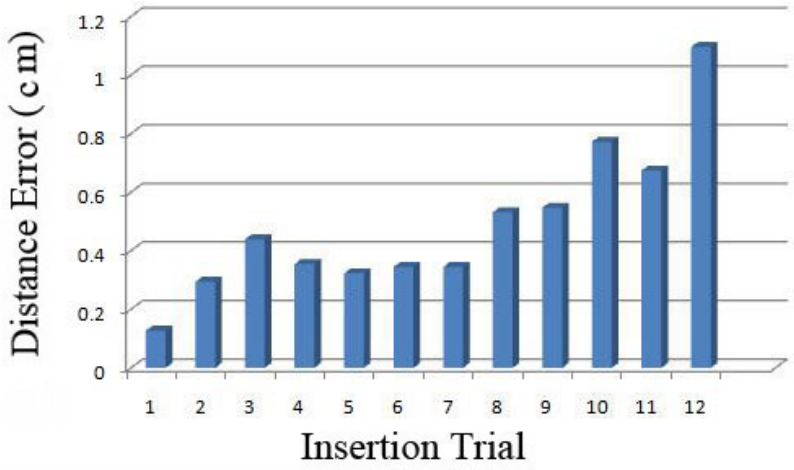

Figure 7.1: Distance error from predefined target- counter-clockwise rotation of swim wave motion

The actual size of surgical needle is $3mm$ in diameter and search area of the target is $50mm$ wide inside the tissue. The needle should be navigated inside this area. In our prototype, the width of the active needle is $15mm$. Thus, linear scale factor is determined as 5 and search area of the target for the active needle is $250mm$ wide. The average distance error for two insertions is calculated for twelve insertion: $4.9mm$ for the first target and $1.8mm$ for the second target. Both results

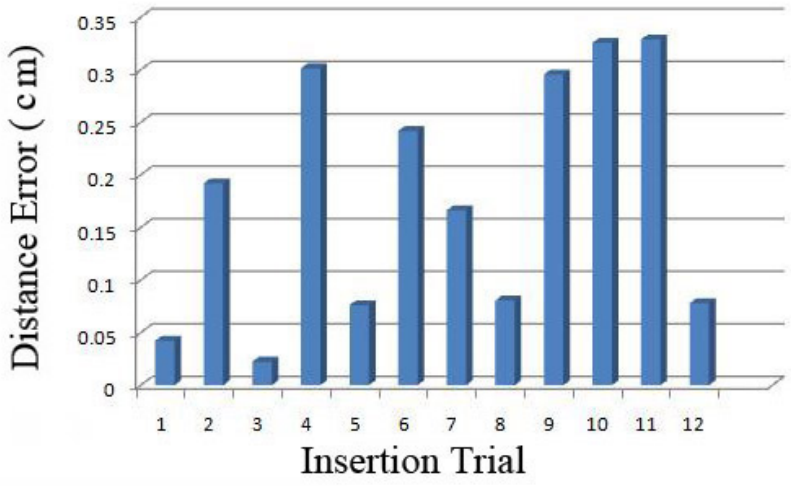

Figure 7.2: Distance error from predefined target- clockwise rotation of swim wave motion

have good accuracy which is less than 5% error in needle placement.

7.1.4 Application

In liver surgery, the active needle can deliver drug to the affected area or can be used for ablation. In prostatic therapy, the needle can be used to implant a seed in the tumour. Furthermore, the active needle can be used for biopsy, by connecting number of links together to propagate swim-wave motion along the body of a long active needle. Therefore, active needle can be used for many clinical applications due to its flexibility and compact size.

7.2 Future Works

This thesis opens up some directions for further investigations.

Kinematic analysis of the closed-loop mechanism should be analyzed and should be integrated to the kinematic analysis of the main body. This kinematic analysis can solve mapping relationship between swim-wave motion, joints' revolutions and the needle tip's position.

The size of the active needle can be reduced by the technology of microfabrication, although actuators are positioned at the base of the needle in order not to constrain the size of the needle. In the design of the active needle, only the length of moment arm constrains the size of needle. The length of moment arm can be reduced if the motor provides a larger torque to move the bars of the closed-loop mechanism forward and backward. A servo motor can provide a larger torque and can be a good substitution for the stepper motor of swim-wave motion.

It is suggested that a comprehensive control scheme to be used in order to improve the accuracy of the needle tip placement. Therefore, some sensors are required to read the position of the needle tip and to measure applied forces, to bring the feedback to be the input of control system.

Imaging techniques could determine the position of the clinical target and the needle position. The readings of the imaging techniques can be used to update the position of the target and the actuating signal of actuators.

7.3 Conclusion

Active needle is a new robotic system for the needle surgery with enhanced flexibility to reach inaccessible targets. Modeling of the needle and its interaction with the tissue is described. Computational example for the inverse kinematics is also investigated.

Optimal path is obtained according to energy minimization of the bending moment of the needle, under the application of needle-tissue interaction forces. Simulation of the active needle is used to follow the optimal path. Preliminary work on the active needle modeling and path planning has been published in IEEE international conference on Systems, man, and cybernetics [98].

The active needle prototype is a new robotic insertion system which is different from current systems. The active needle is designed to be flexible and compact with the aid of a special mechanism.

Bibliography

[1] K. Cleary, and Ch. Nguyen, "State of the Art in Surgical Robotics: Clinical Applications and Technology Challenges",Computer Aided Surgery, vol. 6, no. 6, pp. 31228, 2001.

[2] B. Davies, "A review of robotics in surgery", Proc Inst Mech Eng [H], vol.214, no.1, pp.129-140, 2000.

[3] http://www.embs.org.

[4] http://www.wikipedia.com

[5] W. S. Ng, B. L. Davies, R. D. Hibberd, and A. G. Timoney, "A firsthand experience in transurethral resection of the prostate.", IEEE, EMBS J., pp. 120-125, 1993.

[6] R. Alterovitz, K. Goldberg, "Motion Planning in Medicine: Optimization and Simulation Algorithms for Image-Guided Procedures", Springer Tracts in Advanced Robotics, vol. 50, 2008.

[7] S. P. DiMaio, S. E. Salcudean, "Needle insertion modeling and simulation", IEEE Trans Robotics Autom: Special Issue Med Robotics, vol. 19, pp. 864-75, 2003.

[8] N. Abolhassani et al., "Experimental study of robotic needle insertion in soft tissue", Proceedings of the international congress on computer assisted radiology and surgery, vol. 1268, pp. 797-802, 2004.

[9] R. Alterovitz, K. Goldhere, J. Pouliot, R. Taschereau, and I. C. Hsu, "Needle insertion and radioactive seed implantation in Human tissues: simulation and sensitivity analysis", Proceeding of IEEE International Conference on Robotics & Automation (ICRA), vol.2, pp. 1793-9, 2003.

[10] R. J. I. Webster, J. S. Kim, N. J. Cowan, G. S. Chirikjian, A. M. Okamura, "Nonholonomic modelling of needle steering", International journal of Robotics Research, vol. 25, pp. 509-25, 2006.

[11] O. Goksel, S. E. Salcudean, S. P. DiMaio, "3D simulation of needletissue interaction with application to prostate brachytherapy", Computer Aided Surgery vol. 11, no. 6, pp. 279-88, 2006.

[12] F. Arambula Cosio, M.A. Padilla Castaneda, "Computer assisted surgery", Medical Physics. Seventh Mexican Symposium on Medical Physics, pp. 38-45, 2003.

[13] Dohi et al., "Computer aided surgery system (CAS): development of surgical simulation and planning system with three dimensional graphic reconstruvtion", Proceeding of the first conference on visualization in biomedical computing, pp. 458-462, 1990.

[14] G. Megali, et al., "EndoCAS navigator platform: a common platform for computer and robotic assistance in minimally invasive surgery", International Journal of Medical Robotics and Computer Assisted Surgery, vol. 4, no. 3, pp.242-51, 2008.

[15] J. Zhang, et al., "Criteria of human-computer interface design for computer assisted surgery systems", vol. 13 E, no. 5, pp. 538-541, 2008.

[16] O. Chavanon, et al., "Computer-assisted pericardial punctures: animal feasibility study", First Joint Conference Computer Vision, Virtual Reality and Robotics in Medicine and Medical Robotics and Computer-Assisted Surgery, pp. 285-94, 1997.

[17] G.G. Gubaidullin,"Medical robotics - a new field of medical engineering and robotics", The 8th World Multi-Conference on Systemics, Cybernetics and Informatics, vol. 8, pp. 399-402, 2004.

[18] Y. Louhisalmi, T. Leinonen, "Development of a robotic surgical assistant", Proceeding of Annual International Conference of the IEEE Engineering in Medicine and Biology, vol. 16, no. 2, pp. 1043-1044, 1994.

[19] P. A. Finlay, and M. H. Ormstein, "Controlling the movement of a surgical laparoscope", IEEE Engng in Med. Biol. Mag., vol.14, no.3, pp.289-291, 1995.

[20] J. M. Sackier, and Y. Wang, "Robotically assisted laparoscopic surgery: from concept to development", Computer-Integrated Surgery (Eds R. Taylor et al.), MIT Press, Cambridge, Massachusetts, pp. 577580 , 1996.

[21] A. Zivanovic, and B.L. Davies, "A robotic system for blood sampling", IEEE Trans Inf Technol Biomed, vol. 4, no.1, pp. 8-14, 2000.

[22] R. Taylor, P. Jensen, L. Whitcomb, A. Barnes, R. Kumar, D. Stoianovici, P. Gupta, Z. Wang, E. Dejuan, and L. Kavoussi,"A Steady-Hand Robotic System for Microsurgical Augmentation", International Journal of Robotics Research, vol. 18, no. 12, pp. 1201-1210, 1999.

[23] Z. Wei, G. Wan, L. Gardi et al., "Robot-assisted 3D-TRUS guided prostate brachytherapy: system integration and validation", Med Phys, vol.31, no.3, pp.539-48, 2004.

[24] P.R. Rizun, P.B. McBeth, D.F. Louw, and G.R. Sutherland, "Robot-assisted neurosurgery", vol. 11, no.2, pp.99-106, 2004.

[25] Y. R. Rampersaud, et al., "Application-specific accuracy requirements for image guided spinal surgery", Proceedings of the symposium of fourth computer assisted orthopaedic surgery, 1999.

[26] J. J. Carr et al., "Stereotactic localization of breast lesions: how it works and methods to improve accuracy.", RadioGraphics, vol. 21, pp. 463-73, 2001.

[27] P. L. Roberson et al., "Source placement error for permanent implant of the prostate", Med Phys, vol. 24, no .2, 1997.

[28] H. K. Hussain et al., "Imaging-guided core biopsy for the diagnosis of malignant tumors in pediatric patients", Am Roentgen Ray Soc, vol. 176, pp. 43-7, 2001.

[29] R. Taschereau et al., "Seed misplacement and stabilizing needles in transperineal permanent prostate implants", Radiother Oncol, vol. 55, pp. 59-63, 2000.

[30] V. Narayana et al., "Optimal placement of radioisotopes for permanent prostate implants", Radiology, vol. 199, no. 457, 1996.

[31] Y. Wakasa, M. Oka, K. Tanaka, M. Fujii, S. Yamauchi, and K. Minami, "Development of a Needle-Insertion Robot for MRI-Guided Stereotactic Surgery", Journal of Robotics and Mechatronics, vol.18, no.5, pp. 643-649, 2006.

[32] S. F. Robinson et.al., "Comparative study of deflection characteristics and fragility of 25-, 27-, and 30-gauge short dental needles", JADA, vol. 109, pp. 920-924, 1984.

[33] H. Kataoka et al., "A model for relations between needle deflection, force, and thickness on needle insertion", In Proceedings of the medical image computing and computer-assisted intervention (MICCAI), pp. 966-74, 2001.

[34] R. Alterovitz et al., "Planning for steerable bevel-tip needle insertion through 2D soft tissues with obstacles", Proceedings of the IEEE international conference on robotics and automation (ICRA), pp. 1652-7, 2005.

[35] E. Dehghan, S. E. Salcudean, "Needle insertion parameter optimization for brachytherapy", IEEE Trans Robotics, vol. 25, pp. 509-25, 2006.

[36] A. Jemal, "Cancer statistics", CA Cancer J Clin, vol. 54, no. 8, 2004.

[37] J. C. Blasko, T. Mate, j.E. Sylvester, p. D. Grimm, and W. Cavanagh, "Brachytherapy for carcinoma of the prostate: techniques, patient selection, and clinical outcomes", Seminars in Radiation Oncology vol. 12, no. 1, pp. 81-94, 2002.

[38] E. Nakakura, and M. Choti, "Hepatocellular carcinoma: Current management recommendations", Advances on Onc, vol. 16, no. 2, pp. 12-18, 2000.

[39] S. Mulier,Y. Ni, Y. Miao, A. Rosiere, A. Khoury, G. Marchal, and L. Michel, "Size and geometry of hepatic radiofrequency lesions", Eur J Surg Oncol, vol.20, no.10, pp. 867-78, 2003.

[40] S. A. Mayer, "Ultra-early hemostatic therapy for intracerebral hemorrhage", Stroke, vol. 34, no. 1, pp. 224-9, 2003.

[41] R. Altrovitz, M. Branicky, K. Goldberg, "Motion planning under uncertainty for image-guided needle steering", International Journal of Robotics Research, vol. 27, no. 11-12, pp. 1361-74, 2008.

[42] R. Alterovitz, A. Lim, K. Goldberg, G. S. Chirikjian, A. M. Okamura, "Steering flexible needles under Markov motion uncertainity", International Conference on intelligent robots and systems, pp. 120-5, 2005.

[43] W. Park, J. S. Kim, Y. Zhou, N. J. Cowan, A. M. Okamura, G. S. Chirikjian, "Diffusion-based motion planning for a nonholonomic flexible needle model",

In: IEEE International Conference on robotics and automation, pp. 4600-5, 2005.

[44] S. P. DiMaio, "Modeling simulation and planning of needle motion in soft tissues", PhD thesis, University of Biritish Coloumbia, 2003.

[45] D. Glozman, M. Shoham, "Image-guided robotic flexible needle steering", IEEE Transaction on Robotics vol. 23, pp. 459-66, 2007.

[46] K. G. Yan, T. Podder, D. Xiao, Y. Yu, T. I. Liu, C. Cheng, "An improved needle steering model with online parameter estimator", International Journal of Computer Assisted Radiology Surgery, vol.1, pp. 205-12, 2006.

[47] Y. C. Fung, "Biomechanicsmechanical properties of living tissues", Springer-Verlag, 2nd edition, 1993.

[48] L. Han et al., "A novel ultrasound indentation system for measuring biomechanical properties of *invivo* soft tissue", Journal of Ultrasound Medical Biology, vol. 29, no. 6, pp. 813-23, 2003.

[49] K. R. Nightingale et al., "Investigation of real-time remote palpation imaging", Proceedings of the SPIE conference on medical imaging, pp. 224-9, 2001.

[50] G. E. Trahey et al., "Arterial stiffness measurements with acoustic radiation force impulse imaging", Proceedings of the SPIE conference on medical imaging, p. 34652, 2003.

[51] A. Menciassi et al., "Force sensing microinstrument for measuring tissue properties and pulse in microsurgery", IEEE/ASME Transaction Mechatronics, vol. 8, no. 1, pp. 10-7, 2003.

[52] M. Ottensmeyer et al., "The effects of testing environments on the viscoelastic properties of soft tissues", Proceedings of Medical Simulation: Intl Symp ISMS, vol. 3078, pp. 9-18, 2004.

[53] M. P. Ottensmeyer, "TeMPeST 1-D: an instrument for measuring solid organ soft tissue properties", Experimental Techniques, vol. 26, no. 3, pp. 48-50, 2002.

[54] I. Brouwer et al., "Measuring *invivo* animal soft tissue properties for haptic modeling in surgical simulation", Proceedings of the international conference on medicine meets virtual reality, pp. 69-74, 2001.

[55] J. D. Brown et al., "In-vivo an in-situ compressive properties of porcine abdominal soft tissues", Proceedings of the international conference on medicine meets virtual reality, pp. 26-32, 2003.

[56] C. K. Chui, E. Kobayashi, "Transversely isotropic properties of porcine liver tissue: Experiments and constitutive modelling", Medical and Biological Engineering and Computing, vol. 45, no. 1, pp. 99-106, 2007.

[57] A. E. Kerdok et al., "Truth cube: establishing physical standards for soft tissue simulation", Medical Image Analysis vol. 7, pp. 283-91, 2003.

[58] R. D. Howe, "The truth cube: establishing standards for soft tissue modeling", Proceedings of the IEEE workshop on intelligent robotics and systems, 2003.

[59] S. Cotin, "Surgical simulation and training: the state of the art and need for tissue models, Proceedings of the IEEE workshop on intelligent robotics and systems, 2003.

[60] A. Nava, E. Mazza, M. Furrer, P. Villiger, W. H. Reinhart, "*Invivo* mechanical characterization of human liver", Med. Image Anal, vol. 12, no. 2, pp. 203-216, 2008.

[61] H. Yamada, "Strength of biological materials", Willians & Wilkins, Baltimore, 1970.

[62] C. K. Chui, E. Kobayashi, X. Chen, T. Hisada, I. Sakuma, "Combined compression and elongation experiments and non-linear modeling of liver tissue for surgical simulation", Med. Biol. Eng. Comput, vol. 42, no. 6, pp. 787-798, 2004.

[63] J. M. Schwartz, M. Denninger, D. Rancourt, C. Moisan, D. Laurendeau , "Modelling liver tissue properties using a non-linear visco-elastic model for surgery simulation", Med. Image Anal, vol. 9, no.2,pp. 103-112, 2005.

[64] S. C. Ko, S. Lee, C. H. Hsueh, "Viscoelastic stress relaxation in ilm/substrate systems-Kelvin Model", Jour on Applied Physics, vol. 9, no. 5, pp. 2453-2457, 2003.

[65] H. W. Nienhuys, A. F. van der Stappen, "A computational technique for interactive needle insertions in 3D nonlinear material", Proceedings of the IEEE international conference on robotics and automation (ICRA), pp. 2061-7, 2004.

[66] R. Alterovitz, K. Goldberg, "Comparing algorithms for soft tissue deformation: accuracy metrics and benchmarks", Technical draft UCBerkeley: Alpha Lab., 2002.

[67] L.Heimenz et al., "Development of the force-feedback model for an epidural needle insertion simulator", Journal of Stud Health Technol Inform, vol. 50, pp. 272-7, 1998.

[68] L. L. Holton, "Force models for needle insertion created from measured needle puncture data", Journal Stud Health Technol Inform, vol. 81 pp. 180-6, 2001.

[69] B. H. Meiklejohn, "The effect of an epidural needle. An in vitro study", vol. 42, no. 11, pp. 1180-2, 1987.

[70] B. Maurin B et al., "*Invivo* study of forces during needle insertions", Proceedings of the scientific workshop on medical robotics, navigation and visualization (MRNV), pp.415-22, 2004.

[71] C. Simone, A. M. Okamura, "Modeling of needle insertion forces for robot-assisted percutaneous therapy", Proceedings of the IEEE international conference on robotics and automation (ICRA), pp. 2085-91, 2002.

[72] D. Karnopp, "Computer simulation of stick-slip friction in mechanical dynamic systems", Trans ASME J Dyn Syst Meas Contr vol. 107, pp. 1003, 1985.

[73] A. M. Okamura et al., "Force modeling for needle insertion into soft tissue", IEEE Trans Biomed Eng vol. 51, no. 10, pp. 170716, 2004.

[74] W. Maurel, "3D modeling of the human upper limb including the biomechanics of joints, muscles and soft tissues", PhD thesis. Switzerland: Laboratoire dInfographie-Ecole Polytechnique Federale de Lausanne, 1999.

[75] K. Matsumiya et al., "Analysis of forces during robotic needle insertion to human vertebra. Proceedings of the medical image computing and computer-assisted intervention (MICCAI)", pp. 271-8, 2003.

[76] S. P. DiMaio, S. E. Salcudean, "Interactive simulation of needle insertion models", IEEE Transaction Biomedical Engineering, vol. 52, no. 7, pp. 1167-79, 2005.

[77] T. K. Podder et al., "Evaluation of robotic needle insertion in conjunction with *invivo* manual insertion in the operating room", Proceedings of the IEEE international workshop on robot and human interactive communication, pp. 66-72, 2005.

[78] J. Magill et al., "Multi-axis mechanical simulator for epidural needle insertion", Proceedings of the medical image computing and computer-assisted intervention (MICCAI), pp. 267-76, 2004.

[79] B. Maurin et al., "A parallel robotic system with force sensors for percutaneous procedures under CT-guidance", Proceedings of the medical image computing and computer-assisted intervention (MICCAI), pp. 176-83, 2004.

[80] E. Hagmann et al., "A haptic guidance tool for CT-directed percutaneous interventions", Proceedings of the IEEE international conference on engineering in medicine and biology, pp. 2764-9, 2004.

[81] J. Hong et al., "An ultrasound-driven needle insertion robot for percutaneous cholecystostomy", Phys Med Biol, vol.49, pp. 441-55, 2004.

[82] G. Kronreif et al., "Robotic guidance for percutaneous interventions", Adv Robot, vol. 17, no. 6, pp. 541-60, 2003.

[83] P. N. Breu, T. I. Parker, A. J. Harrison, T. A. Thomas, and A. Cm, "Simulation of resistance forcer acting on surgical needles", Joumol of Engineering in Midicine, vol. 211, no. 13, pp. 335-347, 1997.

[84] X. Wang et al., "3D real-time interactive needle insertion simulation: soft tissue deformable modeling and sensitivity analysis",Proceedings of the international congress on computer assisted radiology and surgery, pp. 1326, 2004.

[85] R. Alterovitz et al., "Simulating needle insertion and radioactive seed implantation for prostate brachytherapy", Proceedings of the international conference on medicine meets virtual reality, pp. 19-25, 2003.

[86] R. C. Susil et al., "System for MR image-guided prostate interventions: canine study", Radiology, vol. 228, pp.886-94, 2003.

[87] G. Fichtinger et al., "System for robotically assisted prostate biopsy and therapy with interactive CT guidance", Acad Radiol, vol. 9, no. 1, pp. 60-74, 2002.

[88] C. Schneider et al., "A robotic system for transrectal needle insertion into the prostate with integrated ultrasound", Proceedings of the IEEE international conference on robotics and automation (ICRA), pp. 2085-91, 2004.

[89] R. Ebrahimi et al., "Hand-held steerable needle device", Proceedings of the medical image computing and computer-assisted intervention (MICCAI), pp. 223-30, 2003.

[90] J. J. Craig, "Introduction to Robotics, Mechanics and Control", 3rd Edition, Pearson Prentice Hall, 2005.

[91] R. M. Muray, L. Zexiang, S. S. Sastry, "A Mathematical Introduction to Robotic Manipulation", CRC Press, Inc., 1st Edition, 1994.

[92] T. Mineta, et al.,"Batch fabricated flat meandering shape memory alloy actuator for active catheter", Sensors and Actuators A: Physical, vol. 88, no. 2, pp. 112-120, 2001.

[93] Y. Haga, Y. Tanahashi, M. Esashi, "Small diameter active catheter using shape memory alloy", Proceeding of The Eleventh Annual International Workshop on Micro Electro Mechanical Systems. MEMS, pp. 419-424, 1998.

[94] C. K. Chui et al., "Integrative Modeling of Liver Organ for Simulation of Flexible Needle Insertion", 9th International Conference on Control, Automation, Robotics and Vision. ICARCV '06, pp. 1-6, Dec 2006.

[95] J. S. Trk, "Analytical Mechanics", Wiley Interscience, 2000.

[96] D. Glozman and M. Shoham, "Flexible Needle Steering and Optimal Trajectory Planning for Percutaneous Therapies", Medical Image Computing and Computer-Assisted Intervention MICCAI, vol. 321, pp. 137-144, 2004.

[97] S. P. DiMaio ans S. E. Salcudean, "Simulated Interactive Needle Insertion", Proceedings of the 10th Symposium on Haptic Interfaces for Virtual Environment and Teleoperator Systems, pp. 344, 2002.

[98] N. Hamzavi, et al., "Flexible Liver-Needle Navigation Using Fish-Like Robotic Elements", Systems, Man and Cybernetics: IEEE, pp. 3491-3496, 2008.

Appendix A: Calculation of Joint Variables for Inverse Kinematic Analysis

A wave-traveling path is proposed for steering the active needle:

$$y = (x + x^2).sin(kx + wt), \tag{7.1}$$

where $k = 2\pi/\lambda$ and $w = 2\pi/M$. M as the resolution of motion is equal to 32; λ as the wave length is assumed to be $15cm$. Therefore, Eq. 7.1 can be obtained as:

$$y = (x + x^2).sin(41.89x + 0.19t). \tag{7.2}$$

From Eq. 7.2, joint variables are calculated. The first time derivative of this path provides the velocity which rotates the path from the initial position to the next position. Each joint can be found by differentiating the path motion. Therefore,

$$\frac{dy}{dt} = 0.19.(x + x^2).cos(41.89x + 0.19t). \tag{7.3}$$

Join variables can be found by Eq. 7.3:

$q_2(t_f) = \frac{dy}{dt}(@x = 5cm, t_f = 5sec) = 0.01$

$q_3(t_f) = \frac{dy}{dt}(@x = 10cm, t_f = 5sec) = 0.02$

$q_4(t_f) = \frac{dy}{dt}(@x = 15cm, t_f = 5sec) = 0.03,$

where $q_2 = \theta_2, q_3 = \theta_3$ and $q_4 = \theta_4$.

Joint variable function of each joint is time variable. Final values of all joint variable are already calculated. Four boundary conditions are employed on each joint variable's function. Therefore, a cubic polynomial is sufficient to approximate joint variable's function. Boundary conditions are $q(0) = 0$, $\dot{q}(0) = \dot{q}(t_f) = 0$, $q(t_f) = q_f$.

$$q(t) = q_0 + q_1.t + q_2.t^2 + q_3.t^3 \tag{7.4}$$

Boundary conditions are

$q(0) = 0$, then $q_0 = 0$

$\dot{q}(0) = 0$, then $q_1 = 0$

$\dot{q}(t_f) = 0$, then $q_2 = -\frac{3}{2}q_3.t_f$

$q(t_f) = q_f$, then $q_3 = \frac{1}{t_f^3}(q_f - q_2.t_f^2)$.

Therefore, $q(t) = \frac{3}{t_f^2}q_f.t^2 - \frac{2}{t_f^3}q_f.t^3$. This formula is applicable to each joint and the general formula for all joints can be obtained as:

$$q_i(t) = \frac{3}{t_f^2}q_i f.t^2 - \frac{2}{t_f^3}qi_f.t^3.$$

.

Appendix B: Drawing of The Active Needle Prototype

The active needle consists of main body and closed-loop mechanism. Here are figures (Fig. 7.3, Fig. 7.4 and Fig. 7.5)of three links of the main body of the active needle.

.

The figures of linkages of the closed-loop mechanism are shown below. (Fig. 7.6, Fig. 7.7 and Fig. 7.8).

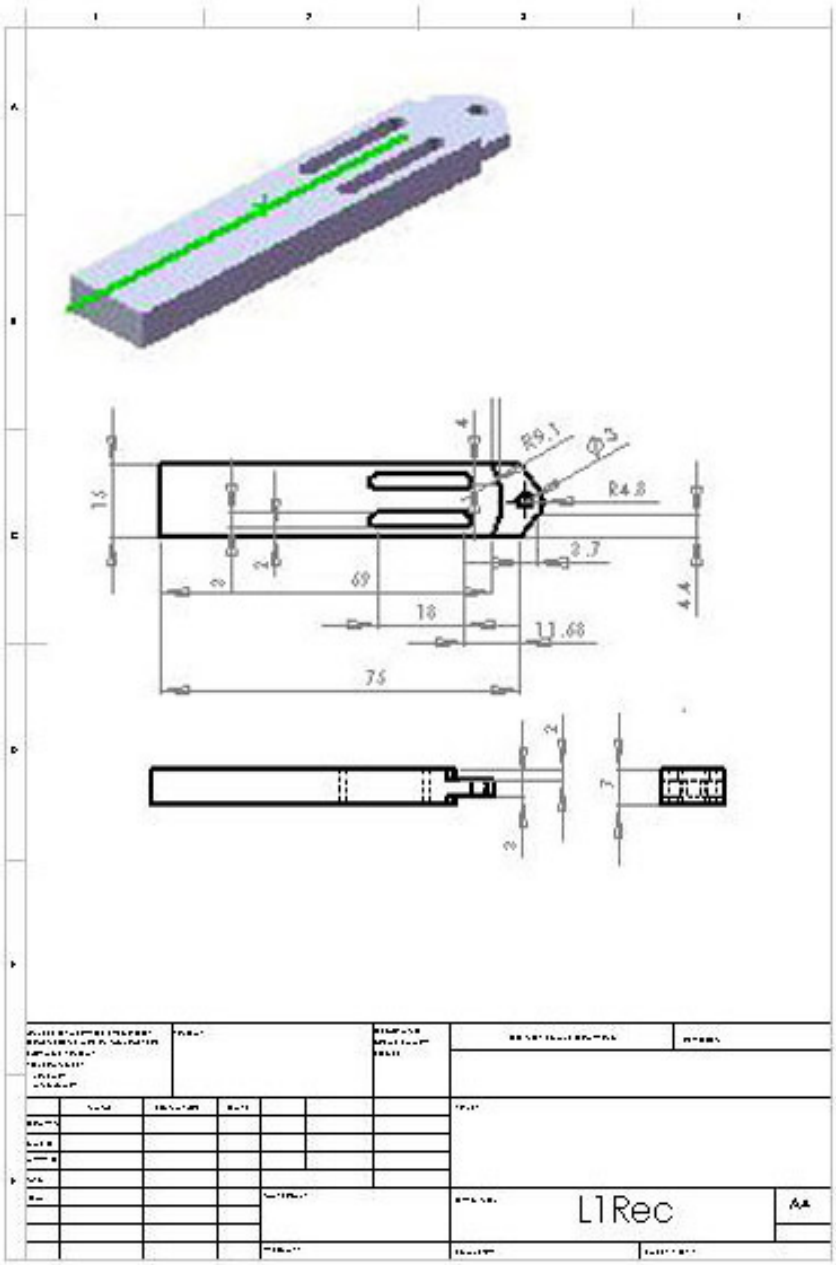

Figure 7.3: First link of main body connected to stepper motor

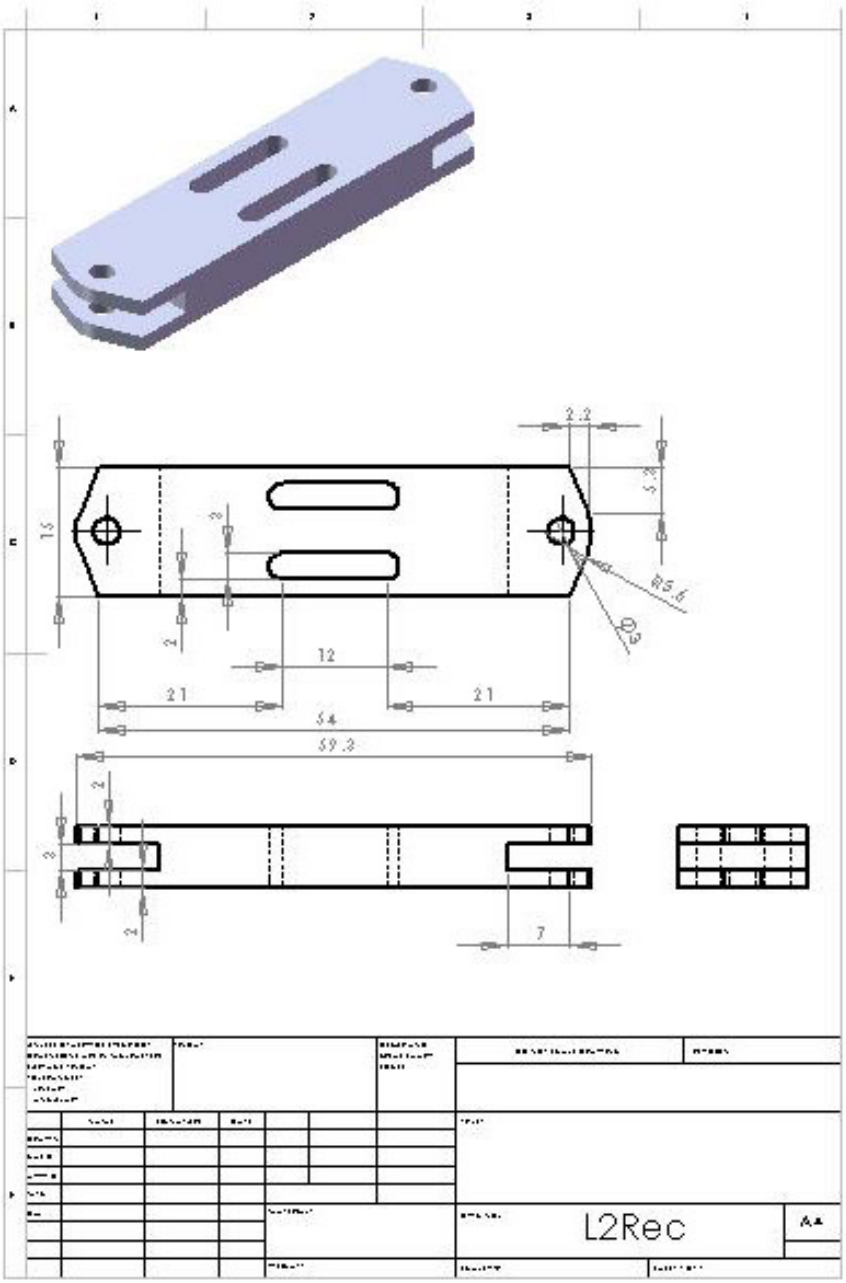

Figure 7.4: Second link of main body

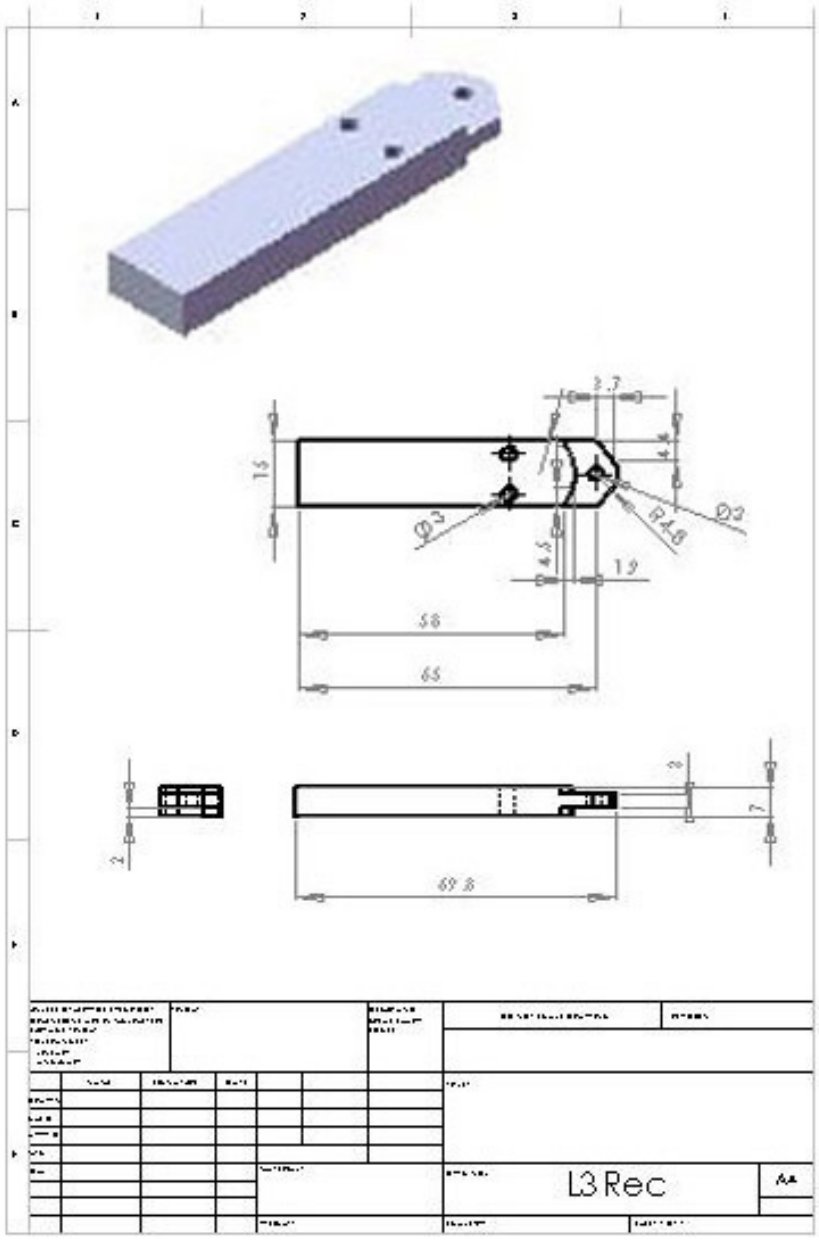

Figure 7.5: Third link of main body

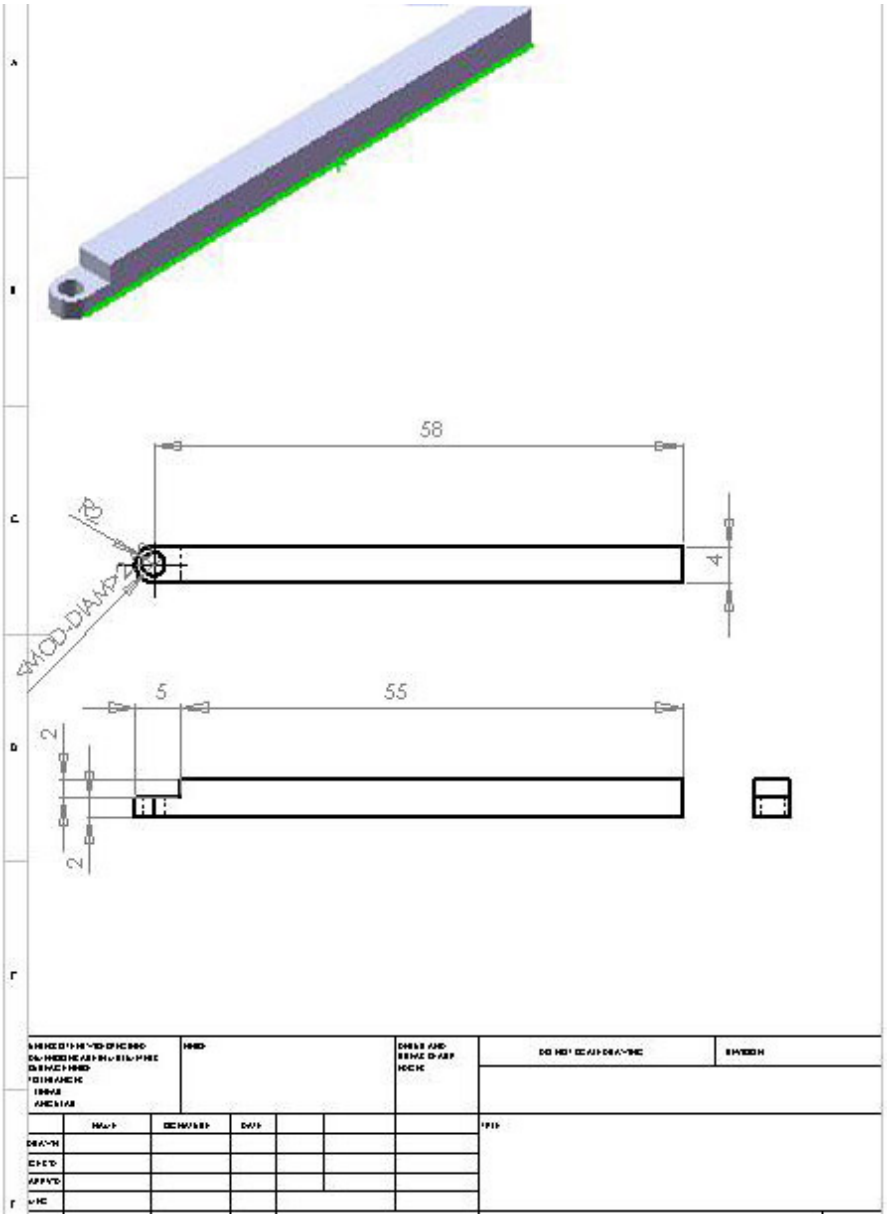

Figure 7.6: First link of closed-loop mechanism connected to stepper motor

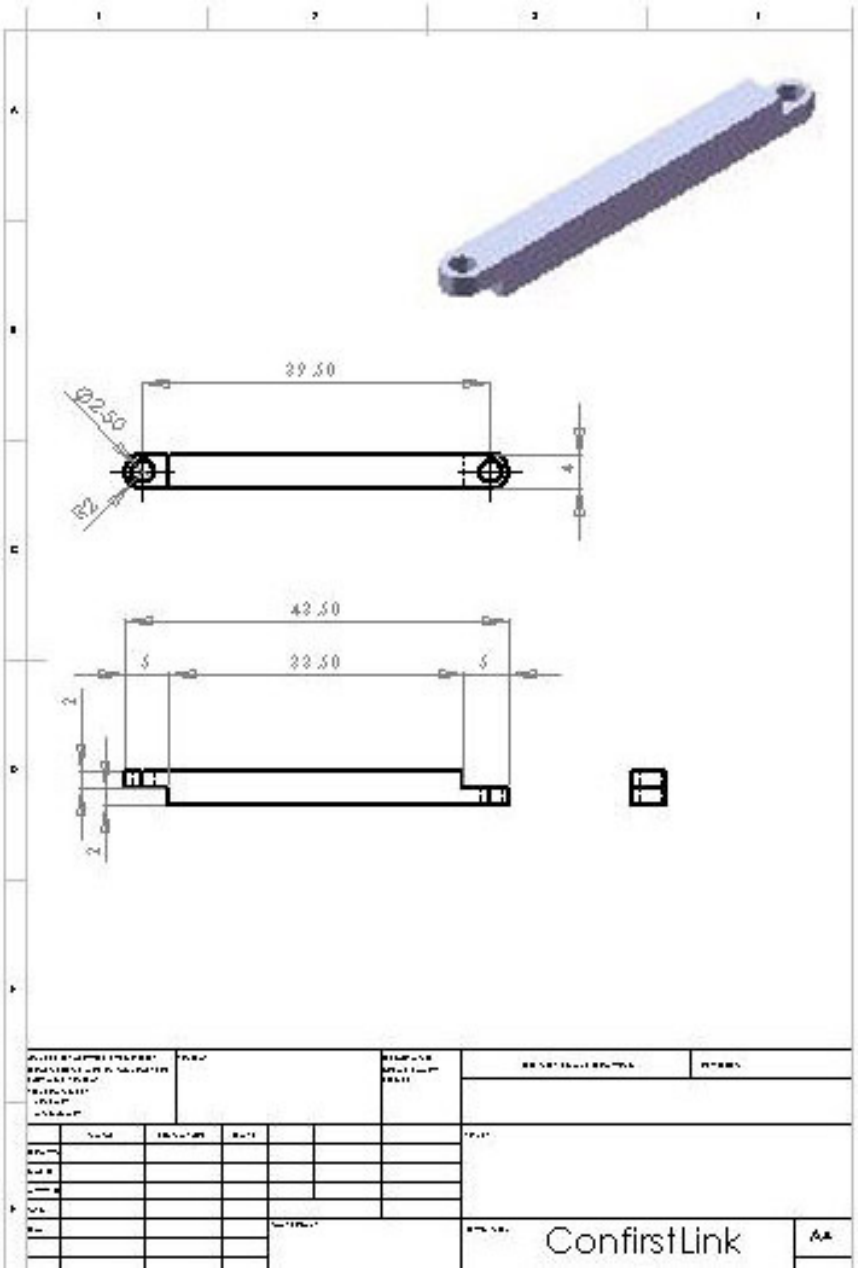

Figure 7.7: Second link of closed-loop mechanism

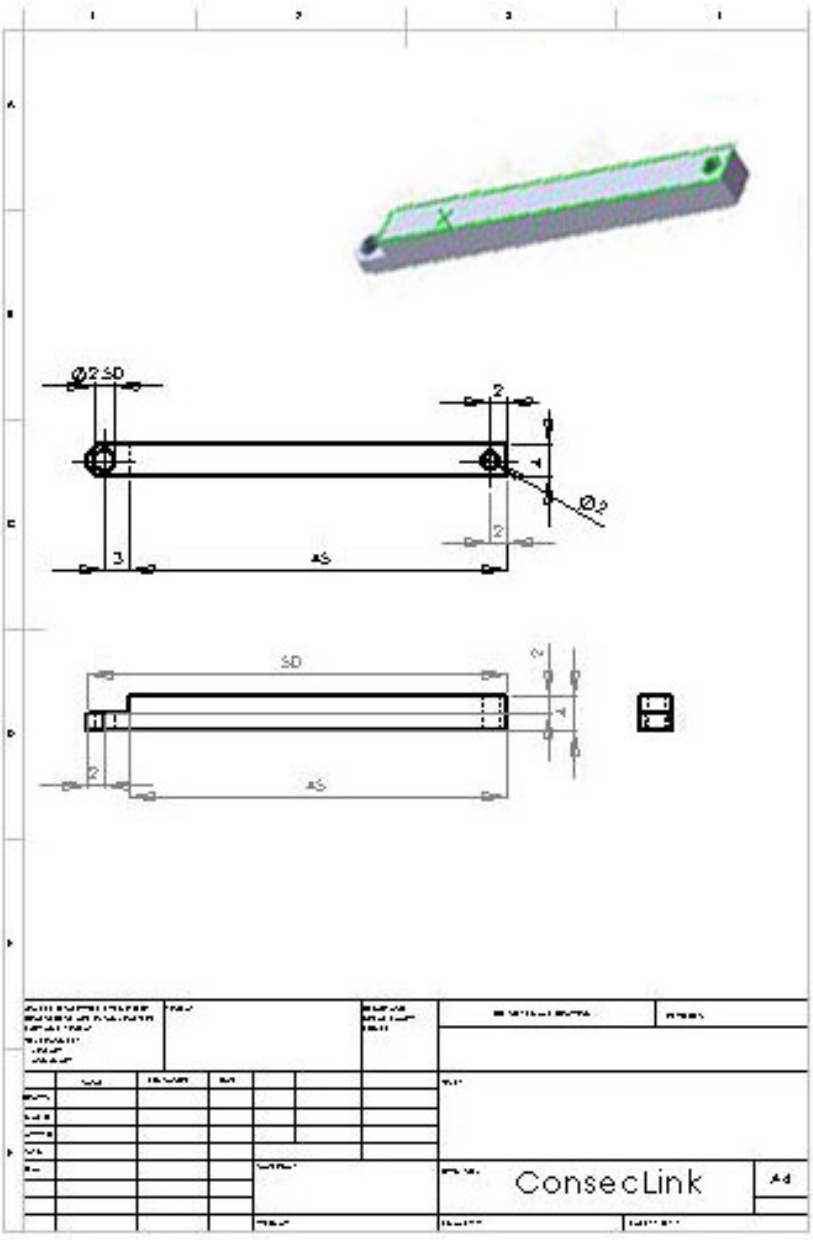

Figure 7.8: Last link of closed-loop mechanism

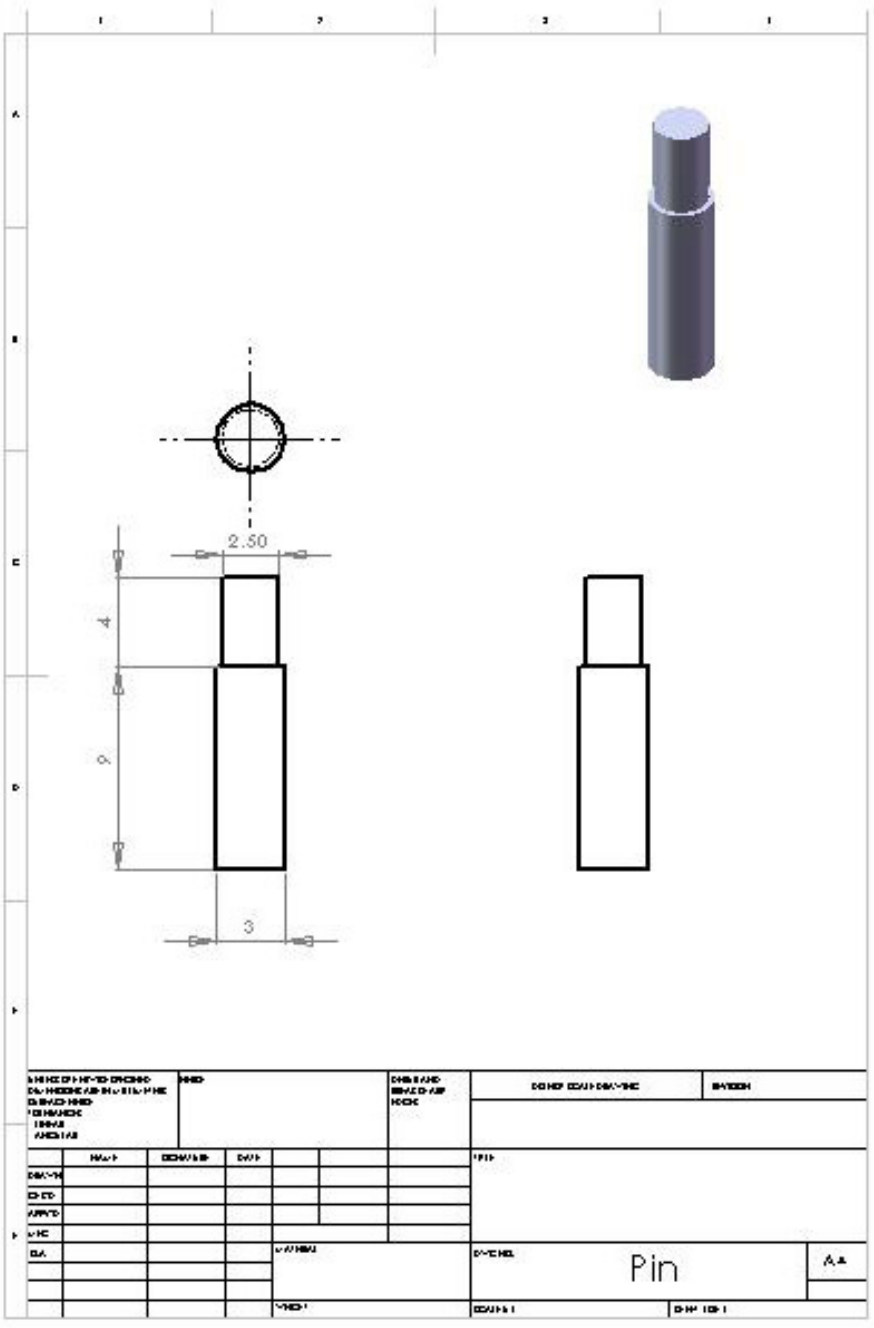

Figure 7.9: Pins for connecting closed-loop mechanism to main body

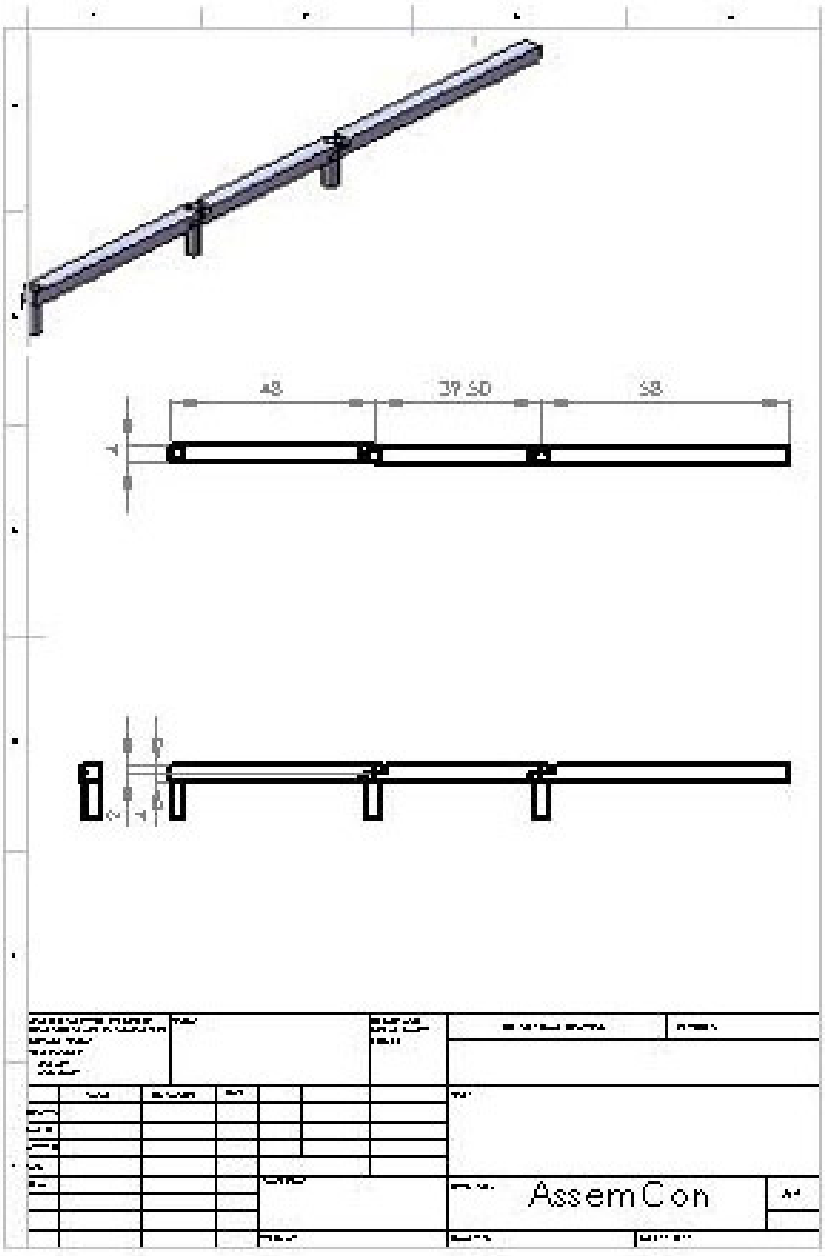

Figure 7.10: Assembly of closed-loop mechanism